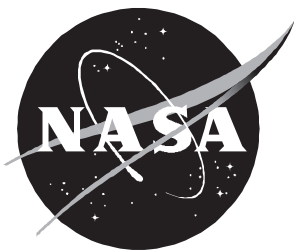


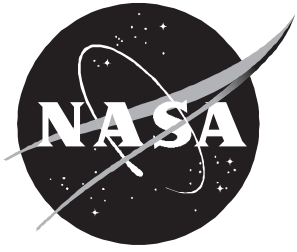
NASA Technical Paper 3427



Subsonic Aerodynamic Characteristics of Semispan Commercial Transport Model With Wing-Mounted Advanced Ducted Propeller Operating in Reverse Thrust

Zachary T. Applin, Kenneth M. Jones, Brenda E. Gile, and P. Frank Quinto

July 1994



Subsonic Aerodynamic Characteristics of Semispan Commercial Transport Model With Wing-Mounted Advanced Ducted Propeller Operating in Reverse Thrust

*Zachary T. Applin, Kenneth M. Jones, Brenda E. Gile, and P. Frank Quinto
Langley Research Center • Hampton, Virginia*

Summary

A test was conducted in the Langley 14- by 22-Foot Subsonic Tunnel to determine the effect of the reverse-thrust flow field of a wing-mounted advanced ducted propeller on the aerodynamic characteristics of a semispan subsonic high-lift transport model (TM). The advanced ducted propeller (ADP) model was mounted separately in position alongside the wing so that only the aerodynamic interference of the propeller and nacelle affected the aerodynamic performance of the transport model. Test Mach numbers ranged from 0.14 to 0.26; corresponding Reynolds numbers ranged from 2.2 to 3.9×10^6 . The primary effect of the ADP on the transport model was reduced lift and drag and was caused by the reverse-thrust flow field of the ADP, which shielded a portion of the wing from the free-stream airflow. The reduction in lift and drag was a function of ADP rotational speed and free-stream velocity.

A vertical ground plane (GP) was installed to determine the ground effect on the transport model and ADP configuration. Test data indicated that the ground plane caused a beneficial increase in drag and an undesirable slight increase in lift. The ADP and transport model performance in ground effect was similar to performance trends observed for out of ground effect.

The test results form a comprehensive data set that supports the application of the ADP engine and airplane concept on the next generation of advanced subsonic transports. Before this investigation, the engine concept was predicted to have detrimental ground effect characteristics. Ground effect test measurements indicated no critical problems and were the first step in proving the viability of this engine and airplane configuration.

Introduction

Recent research and development programs of U.S. airplane and engine manufacturers have focused on the application of large-diameter advanced ducted propellers (ADP's) on the next generation of subsonic transports. The ADP's have significantly greater bypass ratios than conventional turbofan engines and better performance characteristics. (See refs. 1-3.) However, the large diameter of an ADP presents a challenge for achieving an aerodynamically efficient wing-mounted configuration; ground clearance requirements reduce the space between the engine nacelle and the wing, which makes physical integration of the engine and wing more difficult. The aerodynamic interference between the engine and airframe is of concern because of the large

engine diameter in relation to the local wing chord, particularly at the outboard engine location on a four-engined airplane.

Engines are often used to provide reverse thrust to assist airplane deceleration after touchdown. Conventional turbofan engines obtain reverse thrust by deflecting the exhaust forward through the use of cascade deflectors or buckets. The reverse-thrust mechanisms of the engines can be designed to minimize the detrimental effects of exhaust flow on wing aerodynamics and engine performance and to compensate for ground effects. However, the ADP operates in a manner similar to a conventional propeller by utilizing blade pitch angle changes to achieve reverse-thrust capability. As developed to date, the ADP has no other mechanism for directing the reverse-thrust flow. Therefore, determination of the ADP reverse-thrust flow field interaction with the wing and airframe is important to the development of the ADP as a viable engine for subsonic transports.

An investigation was conducted in the Langley 14- by 22-Foot Subsonic Tunnel (ref. 4) to determine the effect of the reverse-thrust flow field of a wing-mounted ADP on the aerodynamic performance of a commercial transport. The test setup consisted of a large 10.5-ft semispan subsonic transport model and 17-in-diameter ADP simulator. The configuration was tested both in and out of ground effect.

Symbols

Longitudinal forces and moments presented in this report are related to the stability axis system. All moment data are referred to the moment reference center on the model centerline, located longitudinally at $0.25\bar{c}$.

All measurements and calculations were made in U.S. Customary System of Units.

C_D	drag coefficient, $\frac{\text{Drag}}{q_\infty S}$
C_L	lift coefficient, $\frac{\text{Lift}}{q_\infty S}$
C_m	pitching moment coefficient about $0.25\bar{c}$, $\frac{\text{Pitching moment}}{q_\infty S \bar{c}}$
C_p	pressure coefficient, $\frac{p - p_{s,\infty}}{q_\infty}$
$C_{p,\text{gp}}$	ground plane pressure coefficient, $\frac{p_{s,\text{gp}} - p_{s,\infty}}{q_\infty}$
\bar{c}	wing mean aerodynamic chord, 27.44 in.
c_{af}	local aft flap chord to nondimensionalize pressure tap locations, in.

c_{mf}	local main flap chord to non-dimensionalize pressure tap locations, in.
c_s	local slat chord to nondimensionalize pressure tap locations, in.
c_w	local cruise wing chord to non-dimensionalize pressure tap locations, in.
L/D	lift-drag ratio, $\frac{C_L}{C_D}$
M_∞	free-stream Mach number
n	boundary layer rake total pressure probe number ($n = 1, 2, 3, \dots, 52$)
p	wing pressure, psf
p_{atm}	atmospheric reference pressure, psf
$p_{s,\text{gp}}$	ground plane static pressure, psf
$p_{s,\infty}$	free-stream static pressure, psf
$p_{t,n}$	boundary layer rake total pressure, psf
q_{gp}	effective dynamic pressure to calculate ground plane velocity, psf
q_1	reference dynamic pressure to characterize flow conditions with ground plane installed, psf
q_∞	free-stream dynamic pressure, psf
R	Reynolds number based on wing mean aerodynamic chord
S	semispan wing reference area, 23.075 ft ²
s	distance of pressure tap from ground plane leading edge, in.
T	temperature, °F
u_{gp}	velocity from ground plane pressure, ft/sec
u_n	velocity from boundary layer rake pressure, ft/sec
u_{q_1}	velocity determined from q_1 dynamic pressure, ft/sec
u_∞	free-stream velocity, ft/sec
x	chord station of pressure tap relative to leading edge, in.
z	height of boundary layer rake pressure probe above tunnel floor, in.
α	angle of attack, deg

β_{ADP}	ADP blade pitch angle, deg
Δ	incremental value
δ_{wall}	wall flap deflection angle, deg
η	nondimensional semispan station
ρ	free-stream density, slugs/ft ³

Abbreviations:

ADP	advanced ducted propeller
AF	axial force
BL	boundary layer
GP	ground plane
NF	normal force
PM	pitching moment
RM	rolling moment
SF	side force
TM	transport model
YM	yawing moment

Model Description

The test airplane was a semispan low-wing, wide-body commercial transport model which simulated the entire port side. A sketch of the transport model and wing planforms is presented in figure 1. The wing was tested in both cruise and high-lift planforms. The high-lift wing incorporated a full-span, leading-edge slat and a partial-span, double-slotted trailing-edge flap system. The wing had chordwise rows of pressure taps at three different span stations. On the slat, pressure taps were located in line normal to the leading edge; on the wing, pressure taps were also located in line normal to the leading edge up to $0.15c_w$ and then in line in the streamwise direction aft. Pressure taps on the flap elements were also located in line in the streamwise direction. Pressure taps were concentrated near the leading edge of each wing component and were not necessarily distributed to the trailing edge.

Photographs of the semispan transport model installed in the Langley 14- by 22-Foot Subsonic Tunnel are presented in figure 2. The transport model was mounted so that the plane of the model centerline was nominally 0.5 in. above the tunnel floor. The vertical tail had an upper fairing designed for mounting a T-tail horizontal stabilizer (fig. 2(d)); the horizontal stabilizer was not installed during any of the tests. Initial tests of the cruise wing configuration were conducted with the vertical tail and a simulated aft fuselage-mounted engine and pylon installed on the model. All of these components were subsequently removed during the tests with the

high-lift wing configuration because of balance load limitations.

An ADP model with a 17-in-diameter propeller disk was installed in a simulated wing-mounted configuration for powered operation; the ADP model was tested only with the transport model and the high-lift wing planform. Figure 3 shows the advanced ducted propeller model and support stand. The ADP was coupled to a 1350-hp air turbine that was powered by the facility high-pressure air system. The ADP model contained two balances: one that measured thrust and torque loads on the propeller disk and the other that measured nacelle drag. The ADP balance measurements are not included in the report. The ADP model and air turbine were supported by a vertical floor-mounted, cylindrical column with a streamlined top adapter and horizontal strut. (See fig. 3.) High-pressure air was supplied through the streamlined adapter and strut to the air turbine and exhausted from the aft end into the test section.

The aft portion of the simulated engine pylon was cantilevered from the ADP centerbody with no structural contact with the wing. A nonfouling foam insert was cut to match the cross-sectional contour of the pylon and to seal the small gap between the end of the pylon and the lower surface of the wing. (See details in fig. 3(b).) This mounting technique resulted in the capability of measuring only the aerodynamic interference of the ADP on the transport model.

The longitudinal location of the ADP nacelle exit was in line with the cruise wing leading edge at the semispan station $\eta = 0.387$. The ADP was tested at two waterline locations without the ground plane installed. The gap between the lower surface of the slat and the ADP nacelle was used to locate the ADP position relative to the wing. (See fig. 3(b).) The slat-to-nacelle gap was 2.75 in. for one waterline and 0.38 in. for the other.

A sketch of the TM and ADP configuration is shown in figure 4; several photographs of the setup are presented in figure 5. A small vertical streamlined strut was attached to the air turbine and acted as a damper to minimize structural vibrations of the ADP during powered operation.

The ADP blades can be operated at various pitch angles to simulate forward and reverse thrust conditions. Only the reverse thrust performance of the ADP at two blade angles was investigated; the nominal blade angle of $\beta_{ADP} = 98.25^\circ$ and an alternate blade angle of $\beta_{ADP} = 95^\circ$ were evaluated.

Ground effect conditions were simulated by installing a ground plane (vertical wall) 3.5 in. (0.18 na-

celle diameter) from the bottom of the ADP nacelle. (See figs. 6 and 7.) The ground plane had a rounded leading edge to make it insensitive to potential misalignment with the free-stream flow. A large adjustable flap was attached to the tunnel wall opposite the downstream edge of the ground plane. The wall flap was manually set at various deflection angles and provided control of free-stream velocity when the ground plane was installed. The appendix describes the ground plane test technique and how the wall flap was used as a flow control device.

Tests and Corrections

The investigation was conducted in the Langley 14- by 22-Foot Subsonic Tunnel, which has a test section 14.50 ft high by 21.75 ft wide by 50.00 ft long. The investigation was conducted at free-stream dynamic pressures of 30 to 100 psf, equivalent Mach numbers of 0.14 to 0.26, respectively, and corresponding Reynolds numbers of 2.2 to 3.8×10^6 based on the wing mean aerodynamic chord. The isolated transport model test angles of attack ranged from -4° to 20° with the cruise wing and from -4° to 32° with the high-lift wing. No boundary layer transition grit was used during the tests discussed in this report.

During tests of the isolated transport model, tunnel conditions and test data were based on free-stream dynamic pressures. However, during tests with the ADP installed, tunnel conditions and test data were based on free-stream velocities in knots.

Aerodynamic forces and moments on the transport model were measured with a six-component strain gauge balance located beneath the tunnel floor. The balance characteristics and accuracies are summarized in table I. Although all six balance components were measured during the investigation, model side force and yawing moment measurements were meaningless because of the nature of the semispan test setup; side force, yawing moment, and rolling moment data have been excluded from the report.

Model angle of attack was set by the yaw drive of the model support system and was measured by a curvilinear transducer attached to the turntable; the data acquisition and analysis system converted the yaw angle to model angle of attack.

Pressure measurements were obtained with an electronically scanned pressure system. This system was capable of on-line calibration, which was done frequently to maintain a high degree of accuracy.

Wing, body, and wake tunnel blockage corrections were determined according to the methods of reference 5. The blockage corrections were used to

Table I. Balance-to-Model Component Orientation and Balance Load Characteristic Effects on Aerodynamic Coefficient Accuracy

Balance component	Model component	Full-scale load, lb, or moment, in-lb	Accuracy, percent	Accuracy of load, lb, or moment, in-lb	Coefficient accuracy at $\alpha = 0^\circ$ for—		
					$q_\infty = 30$ psf	$q_\infty = 50$ psf	$q_\infty = 100$ psf
NF	−NF	5000	0.5	± 25	± 0.0361	± 0.0217	± 0.0108
AF ^a	SF ^a	3500	2.0	± 70	± 0.1011	± 0.0607	± 0.0303
PM ^a	−RM ^a	400 000	0.5	± 2000	± 0.0229	± 0.0137	± 0.0069
RM	−PM	150 000	0.5	± 750	± 0.0395	± 0.0237	± 0.0119
YM ^a	−YM ^a	60 000	0.5	± 300	± 0.0034	± 0.0020	± 0.0010
SF	AF	1500	0.5	± 7.5	± 0.0108	± 0.0065	± 0.0033

^aComponent data not included in results

calculate the corrected free-stream dynamic pressure. No additional corrections were made to account for solid shape or flow field tunnel blockage by the ADP or ground plane. Tunnel wall interference corrections were applied to the data using the techniques of reference 6. No corrections were made to the data for tunnel buoyancy or flow angularity.

Results

Transport model longitudinal aerodynamic characteristics (i.e., lift, drag, and pitching moment coefficients) and wing pressure distributions are presented for various test conditions. Pitching moment data are presented for completeness but are not discussed in detail because no airplane horizontal stabilizer was installed during the investigation. The lift and drag data are untrimmed due to the absence of the horizontal stabilizer. The focus of this investigation was to simulate the airplane operating in reverse thrust in ground effect. In reality, the airplane would be decelerating to a stop on the runway, where lift and drag are of primary concern and pitching moment less important. For ADP interference and ground effect analysis, transport model pitching moment data are not presented.

Discussion of results will follow the general outline shown in table II.

Isolated Transport Model Characteristics

Effect of tunnel airspeed. The Langley 14-by 22-Foot Subsonic Tunnel is an atmospheric wind tunnel which does not have the capability to independently vary dynamic pressure q_∞ , Reynolds number R , and Mach number M_∞ . Therefore, an increase or decrease in any one of these parameters results in a corresponding increase or decrease in the other two. For this investigation, an increase in q_∞

from 30 to 100 psf resulted in an equivalent M_∞ of 0.14 and 0.26, respectively, and a corresponding R of 2.2 and 3.9×10^6 . These relationships are presented graphically in figure 8(a). During tests with the ADP, the free-stream velocity in knots was used to set tunnel conditions. Figure 8(b) shows the relationship between free-stream velocity and dynamic pressure. A comparison is made of two ambient conditions which represent the greatest variation in temperatures recorded during the ADP tests.

Figure 9 presents the effect of the variation in dynamic pressure and corresponding Reynolds and Mach numbers on model aerodynamic characteristics of the isolated transport model with cruise and high-lift wings. The cruise wing configuration (fig. 9(a)) included installation of the vertical tail and aft fuselage-mounted engine nacelle. These components were removed for the high-lift wing configuration (fig. 9(b)) and all subsequent tests. The tunnel floor boundary layer suction system was off for the data presented in figure 9.

The only significant variation in model aerodynamic performance occurred near the stall condition. Note that a similar cruise wing stall angle of attack ($\alpha \approx 14^\circ$) resulted at both the lowest and highest velocities; the stall angles of attack were approximately 1° greater for intermediate velocities. The high-lift wing stall angle of attack decreased progressively as tunnel airspeed was increased.

In general, tunnel airspeed had little or no effect on the data for low angles of attack ($\alpha = \pm 2^\circ$). Note that data comparisons are presented later in this report for the ADP installation and ground effect tests performed at $\alpha = \pm 2^\circ$. Free-stream velocities were not matched exactly for the configurations in those comparisons; however, the transport model aerodynamic coefficients were insensitive to changes

Table II. Topics Discussed in “Results”

Model configuration and test parameter	Force and moment, figure number	Wing pressure distributions, figure number
Isolated transport model with cruise wing (vertical tail and aft fuselage-mounted engine nacelle installed)		
Effect of tunnel airspeed	9(a)	10
Effect of angle of attack on wing pressure distributions		12
Isolated transport model with high-lift wing (vertical tail and aft fuselage-mounted engine nacelle removed)		
Effect of tunnel airspeed	9(b)	11
Effect of angle of attack on wing pressure distributions		13
Effect of tunnel airspeed on tunnel floor BL thickness		
BL suction off, figure 14(a)		
BL suction on, figure 14(b)		
Effect of transport model angle of attack on tunnel floor boundary layer thickness		
BL suction on, figure 15		
Effect of reduction in tunnel floor boundary layer thickness	16	17–18
Transport model with high-lift wing and ADP		
Effect of windmilling ADP on transport model	19	20
Effect of powered ADP on transport model	21	23–24
Effect of ADP waterline location on transport model	22	
Effect of angle of attack (ADP speed \approx 8900 rpm)	25	
Transport model with high-lift wing, ADP, and ground plane installed		
Effect of ground plane on transport model for windmilling ADP	26	
Effect of ground plane on transport model for powered ADP	27	28
Effect of powered ADP and tunnel airspeed on transport model	29	30–31
Effect of ADP blade angle on transport model	32	

in free-stream velocity at the angles of attack used for the ADP installation tests.

The effect of tunnel airspeed on wing pressure distributions is presented in figures 10 and 11 for the cruise and high-lift wings, respectively. Pressure tap locations on the main wing were nondimensionalized with the local cruise wing chord c_w . The local chords for the slat c_s , main flap c_{mf} , and aft flap c_{af} were used to nondimensionalize their respective pressure tap locations. Wing pressure distributions are presented for several angles of attack in the attached flow region (cruise wing $\alpha = 0^\circ, 4^\circ, 8^\circ$, and 12° ; high-lift wing $\alpha = 0^\circ, 8^\circ$, and 16°), one angle near maximum lift (cruise wing $\alpha = 14^\circ$; high-lift wing $\alpha = 22^\circ$), and one angle greater than maximum lift (cruise wing $\alpha = 16^\circ$; high-lift wing $\alpha = 26^\circ$). In general, tunnel airspeed variations had no significant effects on pressure distributions for either wing configuration at angles of attack below stall.

Wing pressure distributions at selected angles of attack for each test dynamic pressure are presented

in figures 12 and 13 for the cruise and high-lift wings, respectively. The cruise wing indicated the typical localized peak pressure coefficient C_p near the leading edge with gradual pressure recovery farther along the upper surface. The pressure coefficient became increasingly more negative with increased angles of attack up to stall; as expected, wing loading decreased at angles greater than the stall angle of attack. The inboard semispan station $\eta = 0.285$ had greater wing pressure load than the other two semispan stations $\eta = 0.646$ and 0.854 .

Pressure distributions on the high-lift main wing and slat configuration indicated an increased wing load with increased angle of attack. The leading-edge localized peak pressure coefficients on the main wing were mitigated by the presence of the slat. The main flap load decreased with increased angle of attack; the aft flap load did not change significantly.

Effect of tunnel floor boundary layer removal. The thickness of the tunnel floor boundary layer (BL) was important to the semispan transport model test. Flow along the surface of the fuselage

can be affected by an excessively thick tunnel floor boundary layer. Therefore, the tunnel floor boundary layer thickness with and without the boundary layer suction system on was measured and the effect on transport model aerodynamic characteristics was assessed. Boundary layer data are presented only for the ADP and high-lift wing configuration.

Tunnel floor boundary layer thickness was measured with a total pressure rake at all test airspeeds. The rake was located at the longitudinal station of the fuselage nose, which was approximately 1.7 ft downstream of the suction system. The rake was also positioned 7.7 ft laterally away from the model to minimize flow interference. (See figs. 1 and 2(a).)

Total pressure measurements obtained with the boundary layer rake were used to calculate velocity ratios from the relationship

$$\frac{u_n}{u_\infty} = \sqrt{\frac{P_{t,n} - P_{s,\infty}}{q_\infty}} \quad (n = 1, 2, 3, \dots, 52)$$

where n is the total pressure probe location number. Free-stream tunnel parameters were used to non-dimensionalize rake measurements.

As presented in figure 14, the boundary layer thickness defined at $u_n/u_\infty = 0.99$ was approximately 7 in. with the boundary layer suction system off. The boundary layer thickness was reduced to approximately 1 in. with the boundary layer suction system on. No attempt was made to measure the growth of the tunnel floor boundary layer along the full length of the fuselage. Changes in model angle of attack had essentially no effect on the tunnel floor boundary layer thickness as indicated in figure 15.

The effect of the reduction in boundary layer thickness on the transport model and high-lift wing configuration is presented in figure 16. An unexplainable reduction in lift and an incremental nose-up pitching moment resulted when the tunnel boundary layer suction system was turned on. The lift reduction occurred mainly in the intermediate range of angle of attack with less effect at low and stall angles. Drag was essentially unaffected.

Pressure distributions with the tunnel boundary layer suction system both off and on are presented in figures 17 and 18 for the lowest and highest tunnel airspeeds at $q_\infty = 30$ and 70 psf, respectively. The reduction in tunnel floor boundary layer thickness had no effect on wing pressures for the test at $q_\infty = 70$ psf and only a slight effect for the test at $q_\infty = 30$ psf.

Engine and Ground Plane Effects

The remainder of this report discusses the ADP and ground plane effect on the transport model aerodynamic characteristics. The isolated transport model high-lift wing configuration is used as a baseline reference.

Effect of ADP. The ADP was installed in close proximity to the high-lift wing of the semispan transport model to simulate a wing-mounted engine installation. (See figs. 4 and 5.) The gap between the lower surface of the slat and the ADP nacelle was 2.75 in. For the ADP installation tests, tunnel conditions were based on free-stream velocity in knots. All remaining data presented in this report will use velocity in knots to identify free-stream flow. In nearly all tests with the ADP installed, the transport model was operated at a geometric inclination of 0° to the free-stream flow. The exceptions were two tests at $\alpha \approx \pm 2^\circ$ to determine sensitivity to angle of attack. Although the geometric angle of the model was fixed, the actual aerodynamic angle of attack differed slightly because of corrections for wind tunnel wall effect.

Figure 19 presents the effect of a windmilling ADP on the transport model lift coefficient, drag coefficient, and lift-drag ratio data C_L , C_D , and L/D , respectively, when plotted versus free-stream velocity in knots. The windmilling ADP had no effect on the lift coefficient and only slightly reduced the drag coefficient which increased the lift-drag ratio. As previously discussed, the ADP was mounted separately and thus, any effects on the transport model were due exclusively to aerodynamic interference.

The windmilling ADP effect on wing pressure distributions is presented in figure 20. The effect was negligible; measurable pressure differences were noted only on the wing upper surface.

The ADP significantly affected the transport model aerodynamic coefficients when powered in reverse thrust. The results are presented in figure 21 for three ADP rotational speeds and a slat-to-nacelle gap of 0.38 in. Two trends are noteworthy in figure 21: (1) as the free-stream velocity increased, the effect on transport model aerodynamic coefficients decreased (i.e., the C_L , C_D , and L/D values for the powered ADP tests approached isolated transport model values) and (2) for a given free-stream velocity, increased ADP rotational speed increased the effect on transport model aerodynamic characteristics. The primary cause of these effects on the transport model was almost assuredly the reverse-thrust flow field developed by the ADP which blocked the free-stream flow from a portion of the wing.

Previous unpublished test results have shown that an isolated ADP when operating in reverse thrust will generate a relatively large donut-shaped flow field. The size of the reverse-thrust flow field is a function of ADP rotational speed and free-stream velocity. As the ADP rotational speed increases, the size of the reverse-thrust flow field increases for a constant free-stream velocity. Conversely, for a constant ADP rotational speed, the size of the reverse-thrust flow field decreases as free-stream velocity increases. The reverse-thrust flow field ceases when the ADP blades stall. Blade stall occurs when either the ADP rotational speed decreases (for a constant free-stream velocity) or free-stream velocity increases (for a constant ADP rotational speed) to where reverse thrust is no longer achieved. Reverse thrust is determined by ADP balance measurements and flow field observations. The parameters which control reverse-thrust flow field characteristics are evident in figure 21. For high ADP rotational speeds and low free-stream velocities, the large reverse-thrust flow field blocked the free-stream flow from a large portion of the wing which significantly affected wing aerodynamic performance. At high free-stream velocities, ADP effects on wing aerodynamic performance were minimized.

The only wing pressure distribution data available are for the TM and ADP configuration with the slat-to-nacelle gap of 2.75 in. The effect of a change in the slat-to-nacelle gap on wing aerodynamic performance is presented in figure 22. Lift and drag data for the two ADP waterline locations (slat-to-nacelle gaps of 2.75 in. and 0.38 in.) were in close agreement below $u_\infty = 120$ knots. Based on these results, wing pressure distributions for the 2.75-in. gap near $u_\infty = 100$ knots are probably representative for the 0.38-in. gap.

The effect of powered ADP reverse thrust on wing pressures for the TM and ADP configuration with a slat-to-nacelle gap of 2.75 in. is presented in figures 23 and 24. Figure 23 shows the powered ADP effect relative to the isolated transport model. Wing upper surface pressure coefficients were dramatically reduced in magnitude by the powered ADP at $u_\infty \approx 90$ knots. The outboard wing station was less affected than the two inboard stations. Again, the pressure distributions (fig. 23(a)) can be assumed to be representative of both ADP waterline locations. At $u_\infty \approx 120$ knots, the effect on wing pressures was not as large, which was expected based on the data presented in figure 22. The data at $u_\infty \approx 120$ knots (slat-to-nacelle gap of 2.75 in.) in figure 22 deviate significantly from the data at lower u_∞ 's and approaches the isolated model characteristics. Increasing free-stream velocity at a fixed ADP rotational

speed had decreasing effect on the wing pressures and approached the isolated transport model results. (See fig. 24.)

As previously mentioned, the transport model and ADP configuration with an ADP rotational speed of ≈ 8900 rpm was tested at $\alpha \approx \pm 2^\circ$ to determine sensitivity to angle of attack. The results are presented in figure 25. As the angle of attack was increased from $\alpha \approx -2^\circ$ to $\alpha \approx 2^\circ$, the lift and drag coefficients increased.

Effect of ground plane. A ground plane (vertical wall) was installed in the Langley 14- by 22-Foot Subsonic Tunnel in close proximity to the transport model and ADP setup to determine ground effect. The ground plane was located approximately 3.5 in. (0.18 nacelle diameter) from the bottom of the ADP nacelle. *All ground effect tests were performed with the ADP located at the slat-to-nacelle gap of 0.38 in.* (See figs. 6 and 7.) The ground plane was partially covered with flow visualization tufts and had a single longitudinal row of pressure taps near the centerline of the ADP. Ground plane pressure data were used to determine flow conditions over the transport model and ADP and to indicate, along with the tufts, the extent of the ADP reverse-thrust flow field.

The effect of the ground plane and windmilling ADP on the transport model aerodynamic coefficients is presented in figure 26. The effect of the ADP, previously presented in figure 19, is repeated in figure 26 for reference. (The only windmilling ADP data available for the TM and ADP configuration without the ground plane were for the slat-to-nacelle gap of 2.75 in.) The ground plane reduced both the lift and drag coefficients with a proportionately greater reduction of the latter; lift-drag values increased as a result of the greater effect on the drag coefficient.

Ground effects with the ADP powered in reverse thrust at ≈ 8900 rpm are presented in figure 27. The ground effect on the transport model (TM, ADP, and GP) resulted in increased lift and drag coefficients relative to the configuration for out of ground effect (TM and ADP). The increase in lift could degrade airplane braking effectiveness. Note that the wing did not have spoilers deployed, which would be a normal condition during runway deceleration; the increase in lift could probably be reduced with wing spoilers. The increased drag would improve airplane deceleration capability.

Ground effects on wing pressures are presented in figure 28 for the ADP rotational speed of ≈ 7500 rpm and $\beta_{ADP} = 98.25^\circ$ with a free-stream velocity of

≈ 90 knots. The ground effect (TM, ADP, and GP configuration) resulted in a greater increase in pressure coefficient at the mid-span station $\eta = 0.646$ than at the other two span stations which indicated a ground-induced buoyancy. Upper surface pressures on the main flap at the inboard station $\eta = 0.285$ indicated complete flow separation for both tests with the ADP installed. (As a reminder, the pressure distributions for the TM and ADP configuration in figure 28 were for the ADP at the 2.75-in. slat-to-nacelle gap, which as previously discussed, was assumed to be representative of the 0.38-in. slat-to-nacelle gap.)

Effect of ADP rotational speed. The ADP rotational speed was varied from ≈ 3750 to ≈ 11200 rpm with the ground plane installed to determine the effect of reverse-thrust power on transport model aerodynamic characteristics. Figure 29 shows the aerodynamic coefficients plotted versus free-stream velocity for $\beta_{ADP} = 98.25^\circ$ and 95° and several ADP rotational speeds. In general, as ADP rotational speed increased, the effect on aerodynamic characteristics increased relative to the isolated transport model. Also, as free-stream velocity was increased, the ADP reverse-thrust effect was reduced. These results are similar to the tests without the ground plane discussed previously. Change of the ADP blade angle had a significant effect and will be discussed further in the next section.

The ADP rotational speed and tunnel free-stream velocity effects on wing pressures are presented in figures 30 and 31, respectively. For a constant free-stream velocity, an increased ADP rotational speed had an increased effect on wing pressure distributions. (See fig. 30.) Pressure distributions approached the isolated transport model results for low ADP rotational speed. As the ADP rotational speed was increased, the wing pressure load was reduced, which correlates with the loss of lift shown in figure 29.

Figure 31 shows the effect of varying tunnel free-stream velocity with a constant ADP rotational speed. The wing pressure load tends to increase with increasing free-stream velocity. As discussed earlier, the size of the reverse-thrust flow field region decreases with increasing free-stream velocity. The wing loading is less affected at higher free-stream velocities for a given ADP rotational speed. Flow separation over most of the wing has occurred near $u_\infty = 30$ knots, as shown by the relatively chaotic pressure distributions ($C_p > 1$).

Effect of ADP blade angle. The nominal reverse-thrust blade angle for the ADP was $\beta_{ADP} =$

98.25° ; however, an alternate $\beta_{ADP} = 95^\circ$ was also tested. The effect of the blade angle change on transport model aerodynamic performance is presented in figure 32. The tests resulted in an apparent ADP blade stall at a lower free-stream velocity for $\beta_{ADP} = 95^\circ$ than for $\beta_{ADP} = 98.25^\circ$ for an ADP rotational speed ≥ 5400 rpm. As the free-stream velocity is increased, ADP blade stall occurs where the transport model lift and drag changes from a gradual slope to a steep slope; this is followed by a plateau region where further increases in free-stream velocity produce little change in lift and drag. Data were not acquired for the ADP at $\beta_{ADP} = 95^\circ$ and 3750 rpm between $u_\infty = 30$ and 90 knots; as a result, the ADP blade stall region could not be precisely determined. In all tests with ADP rotational speed > 3750 rpm, $\beta_{ADP} = 95^\circ$ resulted in blade stall at a lower free-stream velocity than with $\beta_{ADP} = 98.25^\circ$.

Conclusions

A test was conducted in the Langley 14- by 22-Foot Subsonic Tunnel to determine the effect of the reverse-thrust flow field of a wing-mounted advanced ducted propeller on the aerodynamic characteristics of a semispan subsonic transport model. The advanced ducted propeller (ADP) model was mounted separately in position alongside the wing so that only the aerodynamic interference of the ADP affected the aerodynamic performance of the transport model. Test results include an evaluation of ground effect on the transport model and ADP configuration. Conclusions derived from the subject investigation are summarized below:

1. The primary effect of the ADP on the transport model is to reduce lift and drag. The effect is caused by the reverse-thrust flow field created by the ADP that blocks a portion of the wing from the free-stream flow. The reduction in lift and drag is a function of ADP rotational speed and free-stream velocity. The reduction in lift and drag increases as ADP rotational speed increases at a given free-stream velocity or as free-stream velocity decreases at a given ADP rotational speed.
2. The effect of the ADP on the transport model aerodynamic characteristics is similar for both in ground and out of ground conditions.
3. A vertical ground plane is used to determine the ground effects on the transport model and ADP configuration. The ground effect results in a beneficial increase in drag and an undesirable slight increase in lift.

The test results form a comprehensive data set that supports the application of the ADP engine and airplane concept on the next generation of advanced subsonic transports. Before this investigation, the engine application was predicted to have detrimental ground effect characteristics. Ground effect test

measurements indicated no critical problems and were the first step in proving the viability of this engine and airplane configuration.

NASA Langley Research Center
Hampton, VA 23681-0001
March 14, 1994

Appendix

Ground Effect Test Procedure and Philosophy

To determine ground effect on the semispan subsonic transport model, a temporary vertical wall was designed, fabricated, and installed in the test section of the Langley 14- by 22-Foot Subsonic Tunnel. This wall was positioned in close proximity to the transport model and ADP setup and served as a ground plane for the ground effect tests.

The procedure and philosophy of the ground effect tests are summarized below:

1. *Acquire reference performance data for the isolated transport model condition.* Reference dynamic pressures were measured in preselected locations in the test section with the isolated transport model in place, but before the ground plane installation. These measurements as well as the corrected free-stream dynamic pressures provided target values for setting tunnel conditions after the ground plane was installed. The reference dynamic pressure measurement location for q_1 selected from previous experience to have minimal interference from the model and ground plane is shown in figure A1.
2. *Determine best ground plane design.* Previous measurements (ref. 4) have shown that the tunnel has straight flow with little up- or side-flow angularity. Therefore, the challenge was to provide a ground plane that was insensitive to any flow angularity induced by the test setup. The selection was a straight-walled ground plane of constant thickness with a rounded leading edge. (See fig. A2.) The design was also selected for its ease of fabrication. A single row of pressure taps was installed on the surface of the ground plane at a height approximately the same as the centerline of the ADP.
3. *Determine mechanism to control free-stream velocity.* With the ground plane installed, the original test section was effectively divided into two smaller test sections. A mechanism was required to control free-stream velocity along the model side of the ground plane. A large flap that could be deflected at several angles was attached to the tunnel wall and controlled airspeed by increasing or decreasing flow blockage. A plan view of the test section showing the test setup with the ground plane installed is presented in figure A3.
4. *Develop philosophy for setting and assessing free-stream flow conditions with ground plane installed.* The wall flap angle was set so that the

free-stream velocity along the model side of the ground plane matched the free-stream velocity previously measured for the isolated transport model setup. However, no provisions were made for measurement or adjustment of the free-stream velocity distribution.

The transport model was initially tested without the ADP and ground plane to establish baseline characteristics of the model and to measure reference dynamic pressures. These dynamic pressures were used as target values for tests after the ground plane was installed. Figure A4 compares the reference dynamic pressure with the corrected free-stream dynamic pressure. As discussed previously, the free-stream dynamic pressure is a calculated value based on tunnel calibration constants and transport model blockage factors. As shown, the reference dynamic pressure correlated well with the free-stream dynamic pressure; the dashed line represents a perfect match of the dynamic pressures. The correlation somewhat validates the corrections applied to free-stream dynamic pressures for the isolated transport model setup with the assumption that the flow is uniform throughout the cross-sectional area of the test section. Figure A5 presents the effect of angle of attack of the transport model on the reference dynamic pressure for four tunnel airspeeds. The corrected free-stream dynamic pressure was held constant during each test angle of attack. As the model angle of attack increased, the reference dynamic pressure increased; the percentage change in pressure was approximately the same for each of the tunnel test airspeeds. Note that tests with the ADP and ground effect wall were performed with the model near $\alpha = 0^\circ$.

Specifically, the goal of (4) above for setting free-stream velocity with the ground plane installed was to match the reference and free-stream dynamic pressure relationship that existed for the isolated transport model shown in figure A4. The wall flap provided the variable flow blockage that controls the reference and free-stream dynamic pressure relationship.

The transport model, ADP, and ground plane configuration was tested with two wall flap angles of $\delta_{\text{wall}} = 20^\circ$ and $\delta_{\text{wall}} = 25^\circ$. Comparison of the two conditions is shown in figure A6 and indicates that the angle $\delta_{\text{wall}} = 25^\circ$ resulted in a slightly better correlation of reference and free-stream dynamic pressure than the angle $\delta_{\text{wall}} = 20^\circ$; the setting of $\delta_{\text{wall}} = 25^\circ$ was used for all ground effect tests. Figure A7 shows the effect of ADP rotational speed on the reference dynamic pressure measurement; changes in ADP rotational speed from

≈ 3750 rpm to ≈ 11200 rpm resulted in negligible changes in pressures.

As mentioned in (4) above, the free-stream velocity distribution on the model side of the ground plane could not be measured or adjusted. The ground plane probably caused local variations in free-stream velocity. Even though the reference and free-stream dynamic pressure relationship was matched at the location where the reference dynamic pressure was measured, no data were recorded for the free-stream velocity distribution after the installation of the ground plane.

Ground plane and tunnel floor flow visualization tufts and ground plane surface pressure measurements were used to determine flow characteristics. Several tufts in series were attached to the tunnel floor near the leading edge of the ground plane to visually assess the free-stream flow angle; the approximate location of the tufts is presented in figure A8. The position and attitude of the tufts during tunnel operation based on visual observations are shown and indicate relatively straight flow near the leading edge of the ground plane during operation of the tunnel and ADP; tufts on the surface of the ground plane indicate attached flow on the ground plane ahead of the reverse-thrust flow region. A typical flow pattern is shown in figure A9.

Another measure of flow angularity was the analysis of the pressure measurements taken on the symmetrical leading edge of the ground plane. Nondimensionalized ground plane surface pressure coefficients are presented in figure A10 for two wall flap angles $\delta_{\text{wall}} = 20^\circ$ and 25° . Values of s signify pressure tap distances from the ground plane leading edge; positive s indicates the near side (model) and negative s indicates the far side (open).

If the free-stream flow had been perfectly straight, pressure distribution over the leading edge of the ground plane would have been symmetrical. Note that $\delta_{\text{wall}} = 25^\circ$ pressure distribution near the leading edge was more symmetrical than that for $\delta_{\text{wall}} = 20^\circ$. The leading edge stagnation pressure (defined as $C_{p,\text{gp}} = 1$) was not measured because its location was between pressure taps ($\Delta s = 2$ in.) From the data presented, the setting of $\delta_{\text{wall}} = 25^\circ$ provided straighter free-stream flow than did $\delta_{\text{wall}} = 20^\circ$ and was used for all ground effect tests.

The static pressures on the ground plane surface were referenced to atmospheric pressure and were used to calculate the velocity distribution. Because the tunnel operates at atmospheric pressure (i.e., Tunnel total pressure = Atmospheric pressure), the procedure that follows was used to determine veloci-

ties over the ground plane. Bernoulli's principle with certain assumptions states that

$$\text{Dynamic pressure} = \text{Total pressure} - \text{Static pressure}$$

Pressure measurements obtained at the ground plane surface were static pressures $p_{s,\text{gp}}$ referenced to atmospheric pressure (total pressure). The pressure differential is effectively a dynamic pressure and may be expressed as

$$-q_{\text{gp}} = p_{s,\text{gp}} - p_{\text{atm}}$$

or

$$q_{\text{gp}} = p_{\text{atm}} - p_{s,\text{gp}}$$

Because

$$q_{\text{gp}} = \frac{1}{2} \rho u_{\text{gp}}^2$$

then

$$u_{\text{gp}} = \sqrt{\frac{2q_{\text{gp}}}{\rho}}$$

Velocity distributions as determined by the above procedure are presented in figure A11. (Velocities for $C_p > 1$ were set to zero because this condition results in calculating the square root of a negative number.) The region of $s \approx 20$ to 60 in., which was sufficiently aft of the ground plane leading edge and ahead of the reverse-thrust flow field, was assumed to be representative of the free-stream velocity conditions in the vicinity of the ADP. Velocities determined from ground plane pressure measurements in this region were within ≈ 10 knots of the velocities determined from the free-stream and reference dynamic pressures. In conclusion, the free-stream velocity used to set tunnel operating conditions was representative (within ± 10 knots) of the conditions near the transport model and ADP setup.

Figure A12 presents the effect of free-stream velocity and test setup on ADP windmill speed. Because all model and tunnel characteristics were unchanged, comparison of ADP windmill speed with and without the ground plane installed is another indicator of free-stream velocity differences in the vicinity of the ADP. As expected, ADP windmill speed increased with increased free-stream velocity. Installation of the ground plane reduced the windmill speed by ≈ 300 rpm. This effect was possibly due to the ground plane boundary layer interacting with the ADP inlet. Comparison of corresponding velocities for each condition at the same ADP rotational speed suggests that the ground plane reduced the flow velocity in the vicinity of the ADP by ≈ 10 knots, which is in agreement with results determined from ground plane pressure measurements.

References

1. Zimbrick, R. A.; and Colehour, J. L.: Investigation of Very High Bypass Ratio Engines for Subsonic Transports. AIAA-88-2953, Aug. 1990.
2. Leavitt, Laurence D.; and Berrier, Bobby L.: *Transonic Propulsion Aerodynamic Research at NASA Langley Research Center*. SAE Tech. Paper Ser. 921937, Oct. 1992.
3. Pendergraft, Odis C., Jr.; Ingraldi, Anthony M.; Re, Richard J.; and Kariya, Timmy T.: *Installation Effects of Wing-Mounted Turbofan Nacelle-Pylon on a 1/17-Scale, Twin-Engine, Low-Wing Transport Model*. NASA TP-3168, 1992.
4. Gentry, Carl L., Jr.; Quinto, P. Frank; Gatlin, Gregory M.; and Applin, Zachary T.: *The Langley 14- by 22-Foot Subsonic Tunnel: Description, Flow Characteristics, and Guide for Users*. NASA TP-3008, 1990.
5. Rae, William H., Jr.; and Pope, Alan: *Low-Speed Wind Tunnel Testing*, 2nd ed. John Wiley & Sons, Inc., 1984.
6. Heyson, Harry H.: *Use of Superposition in Digital Computers To Obtain Wind-Tunnel Interference Factors for Arbitrary Configurations, With Particular Reference to V/STOL Models*. NASA TR R-302, 1969.

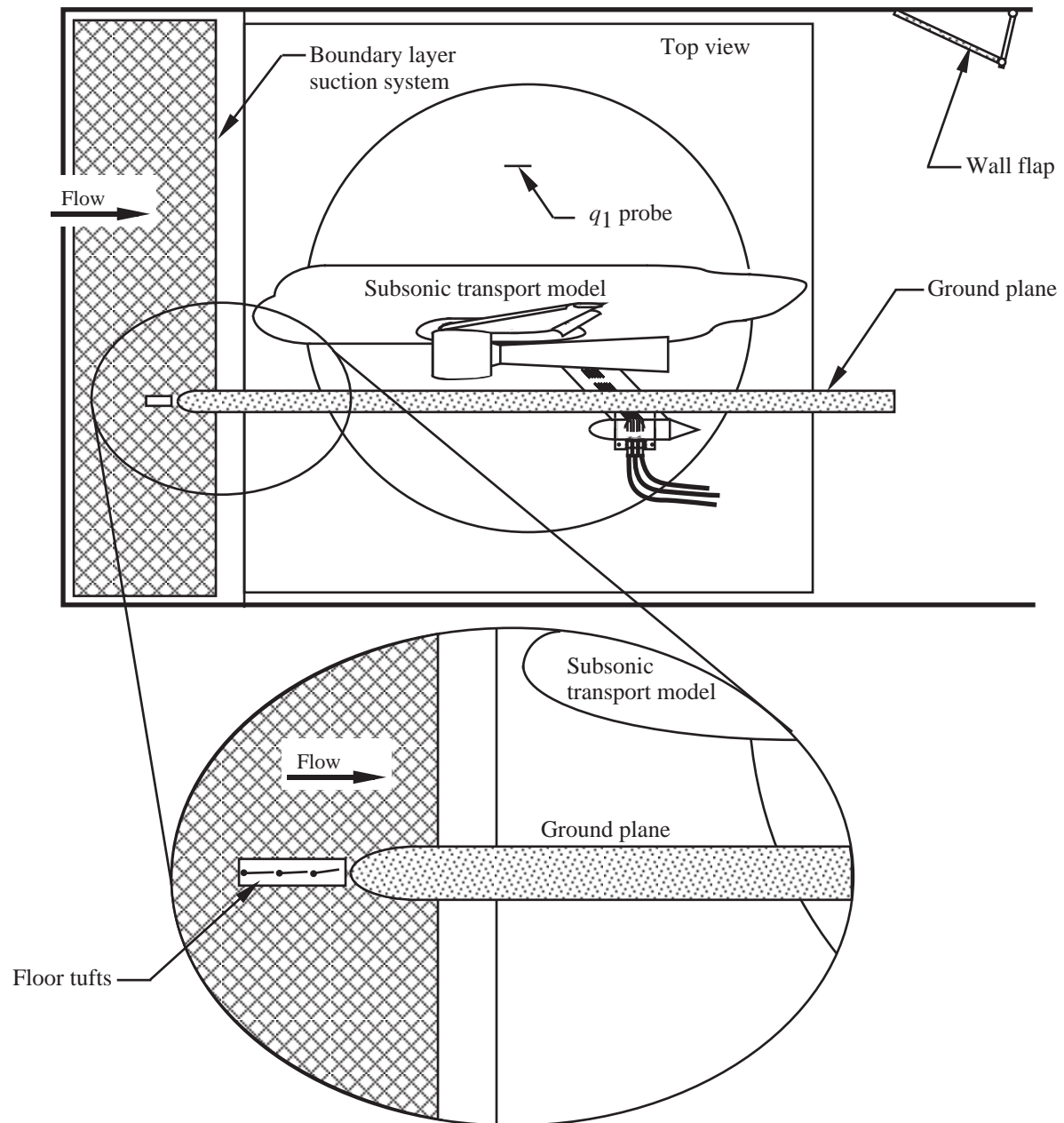
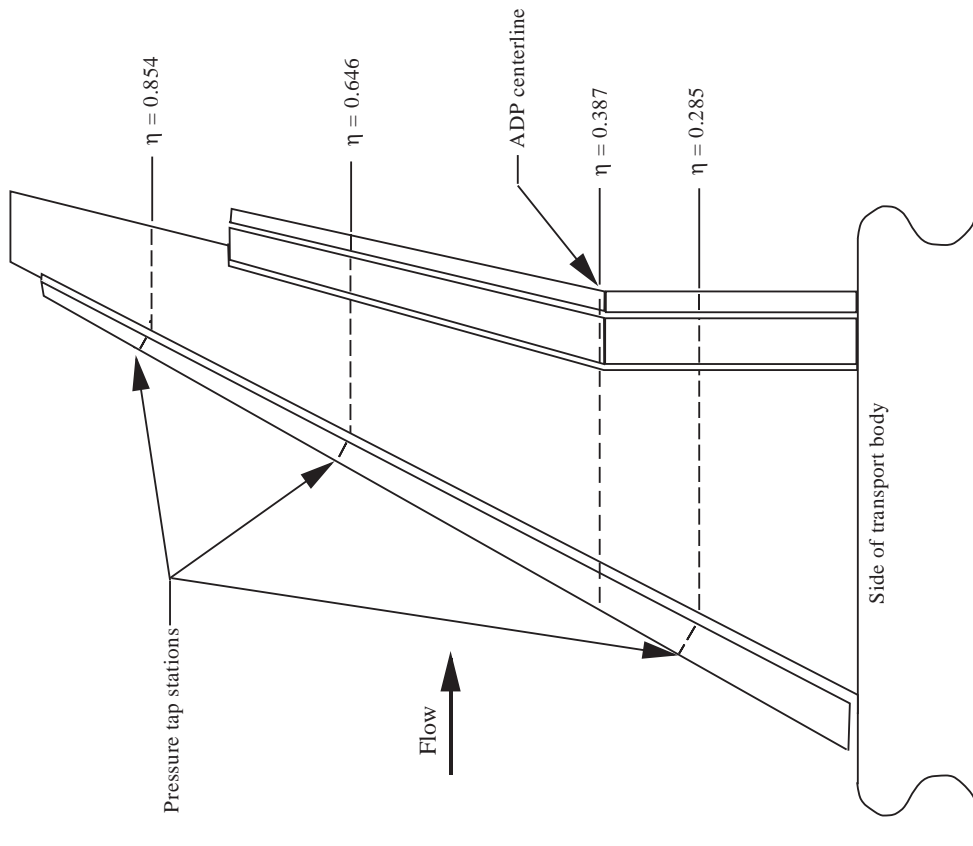
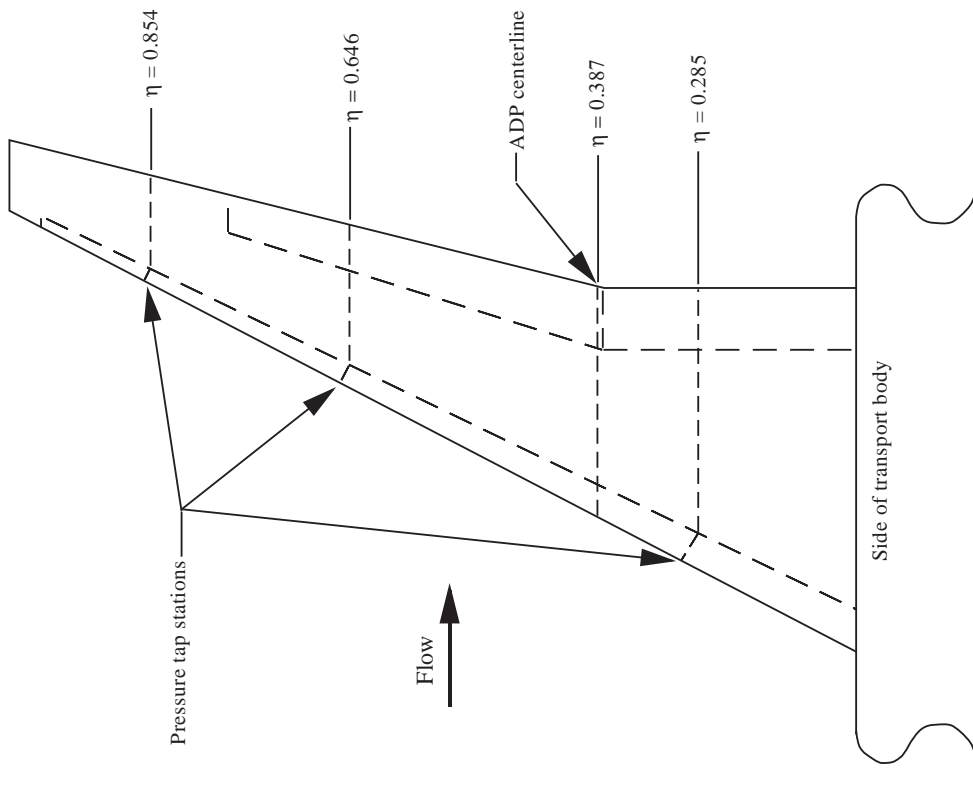


Figure A8. Airflow tuft pattern near leading edge of ground plane.



(c) High-lift wing planform.



(b) Cruise wing planform.

Figure 1.
Concluded.

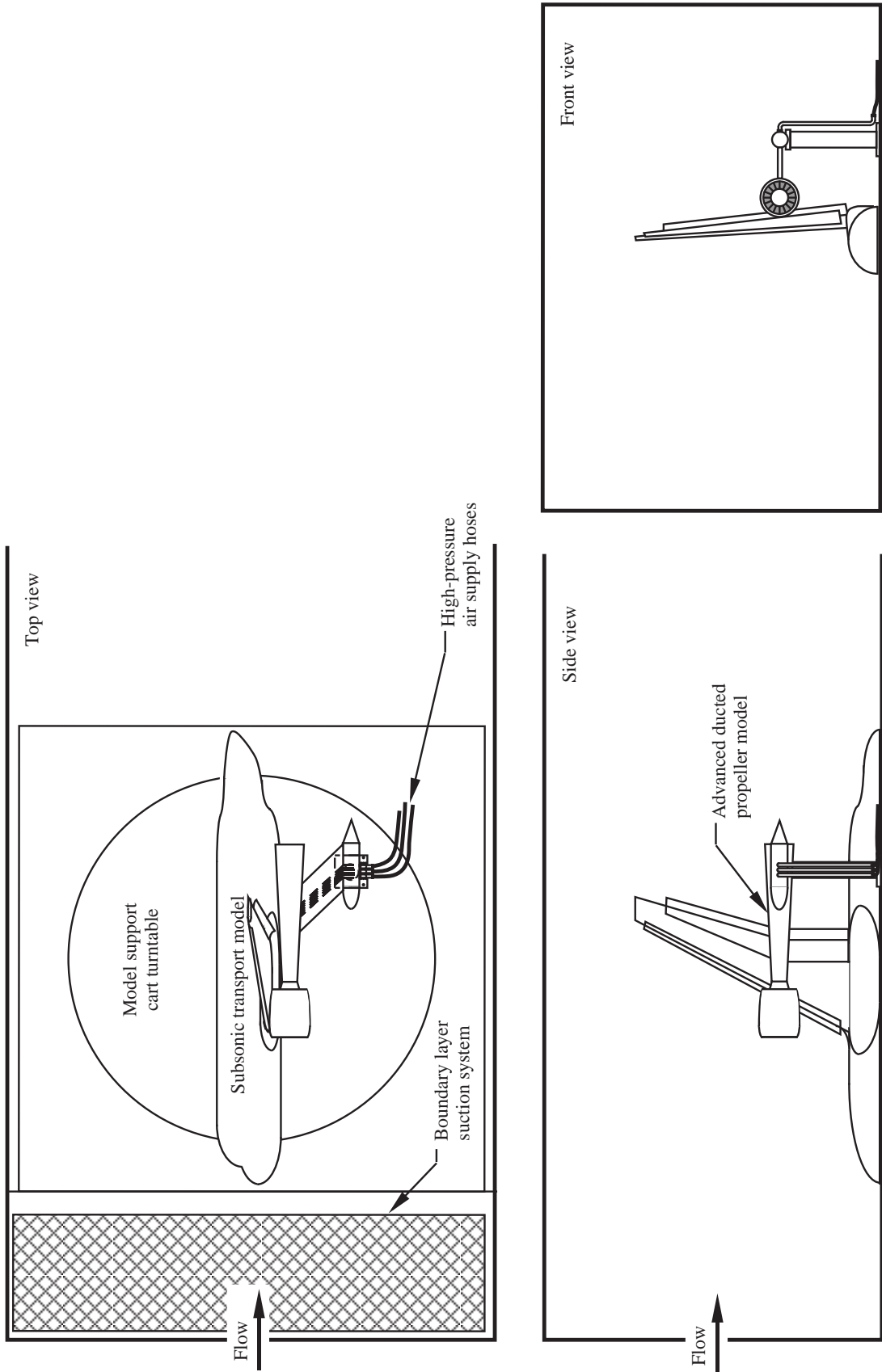
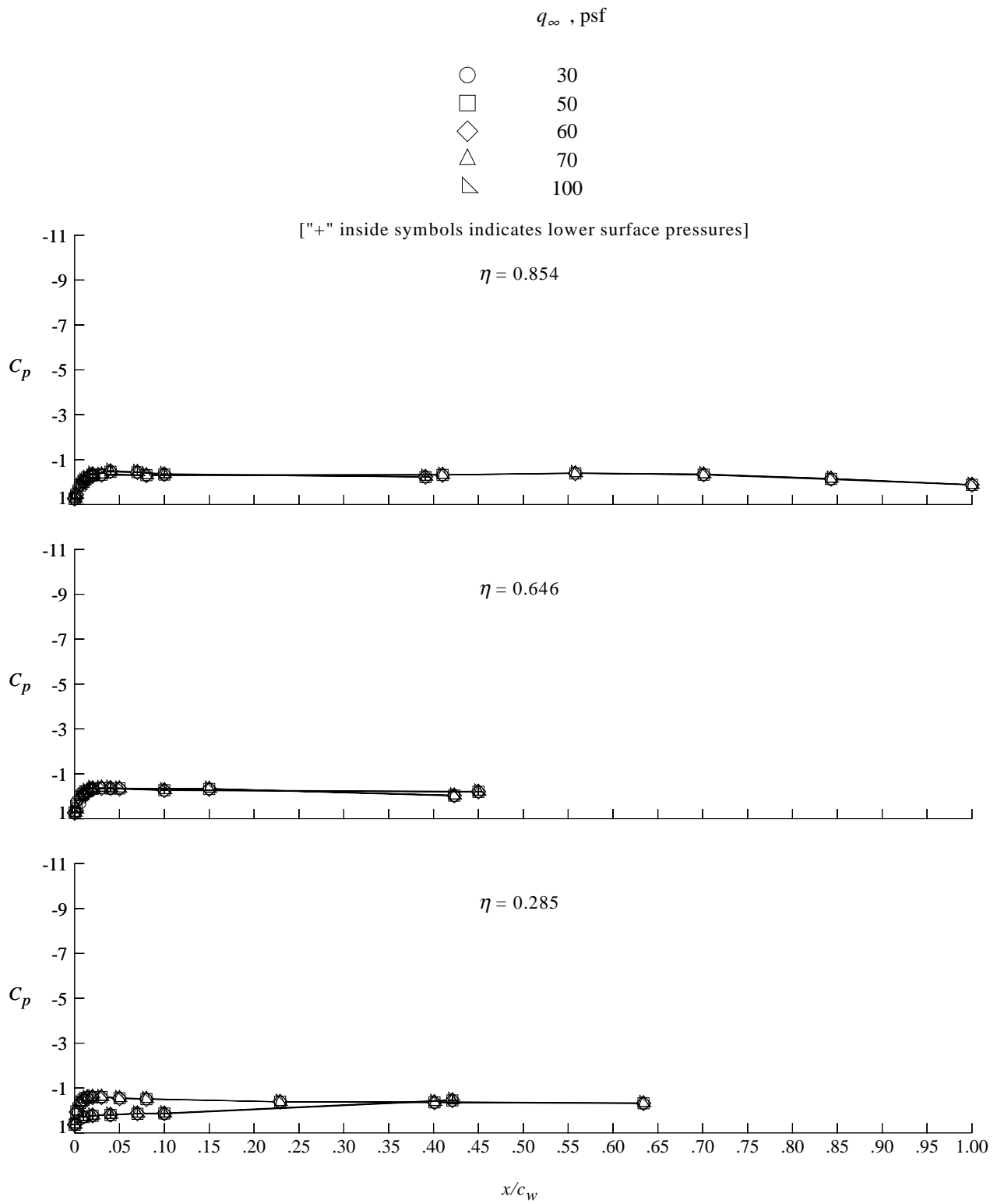
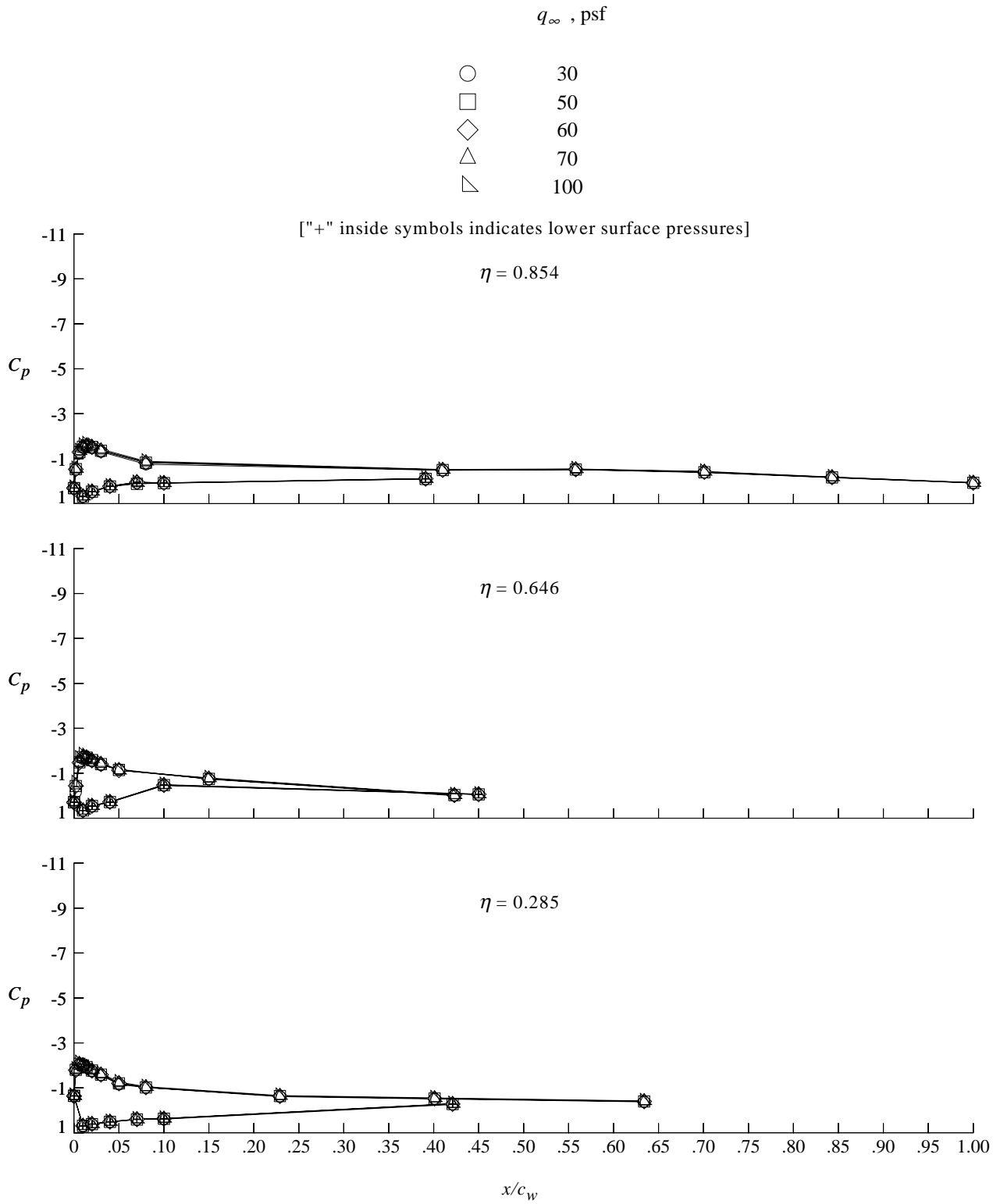


Figure 4. Transport model and simulated wing-mounted ADP test setup with high-lift wing.



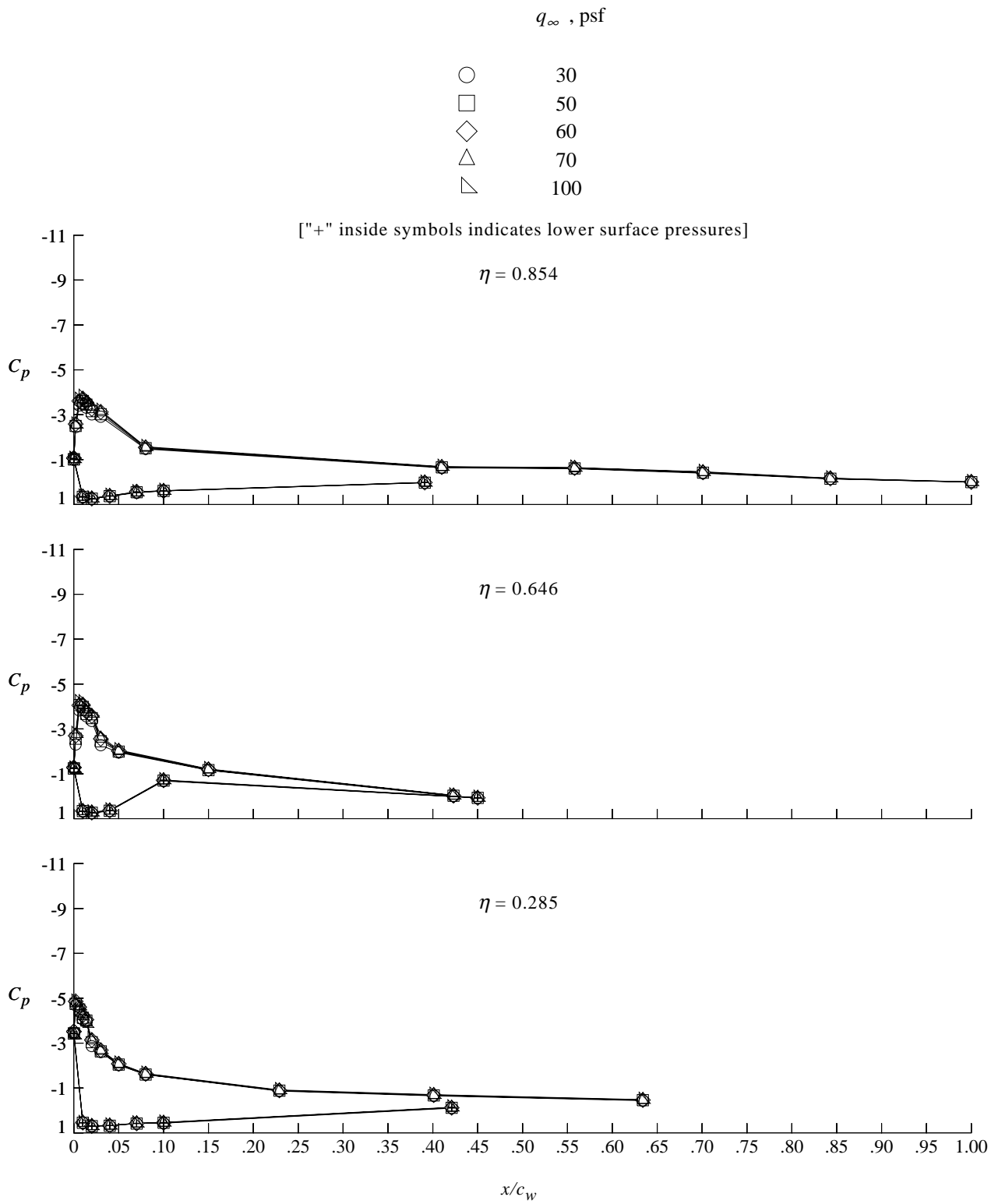
(a) $\alpha = 0^\circ$.

Figure 10. Free-stream speed effect on cruise wing pressure distributions. Tunnel floor boundary layer suction off.



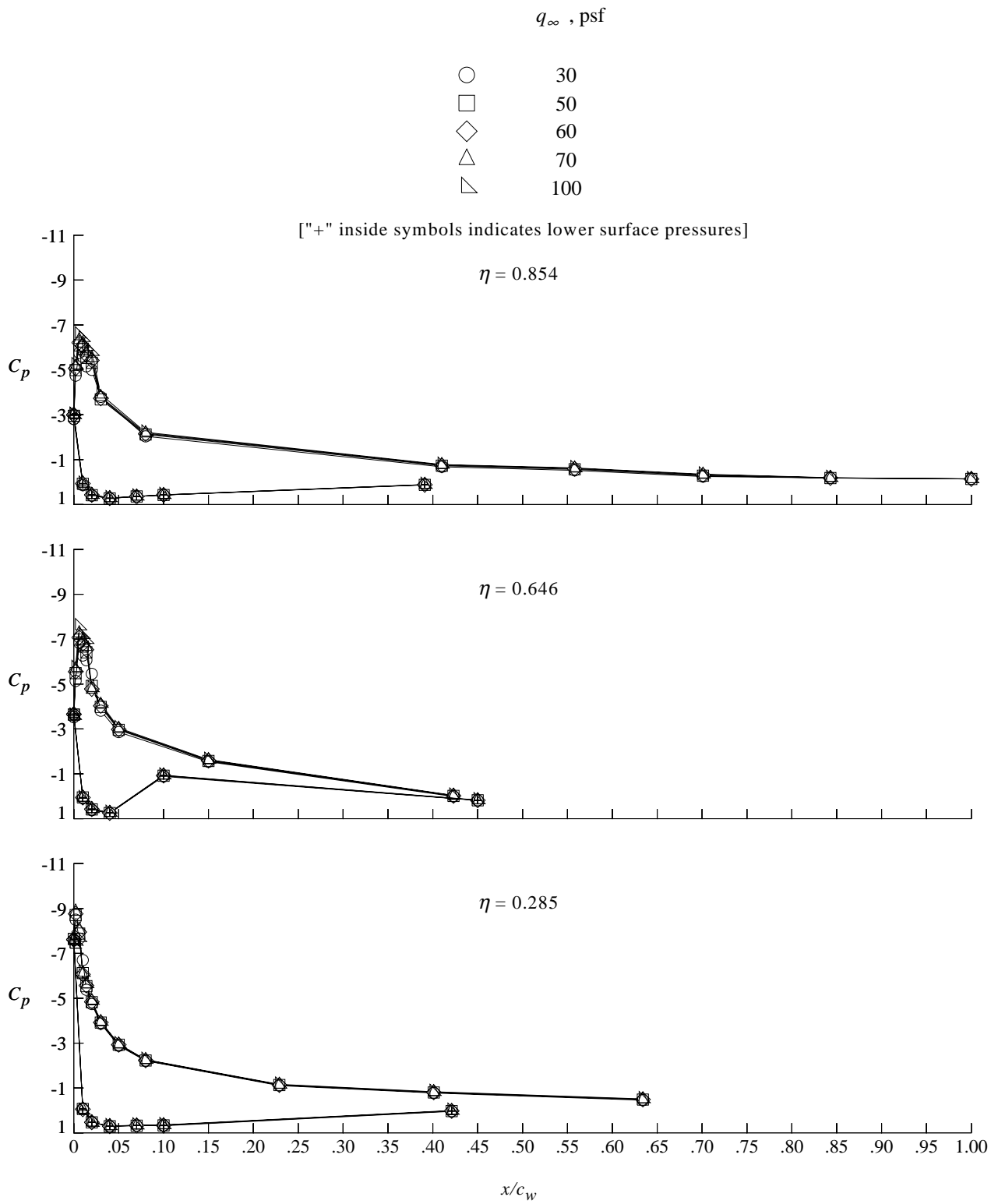
(b) $\alpha = 4^\circ$.

Figure 10. Continued.



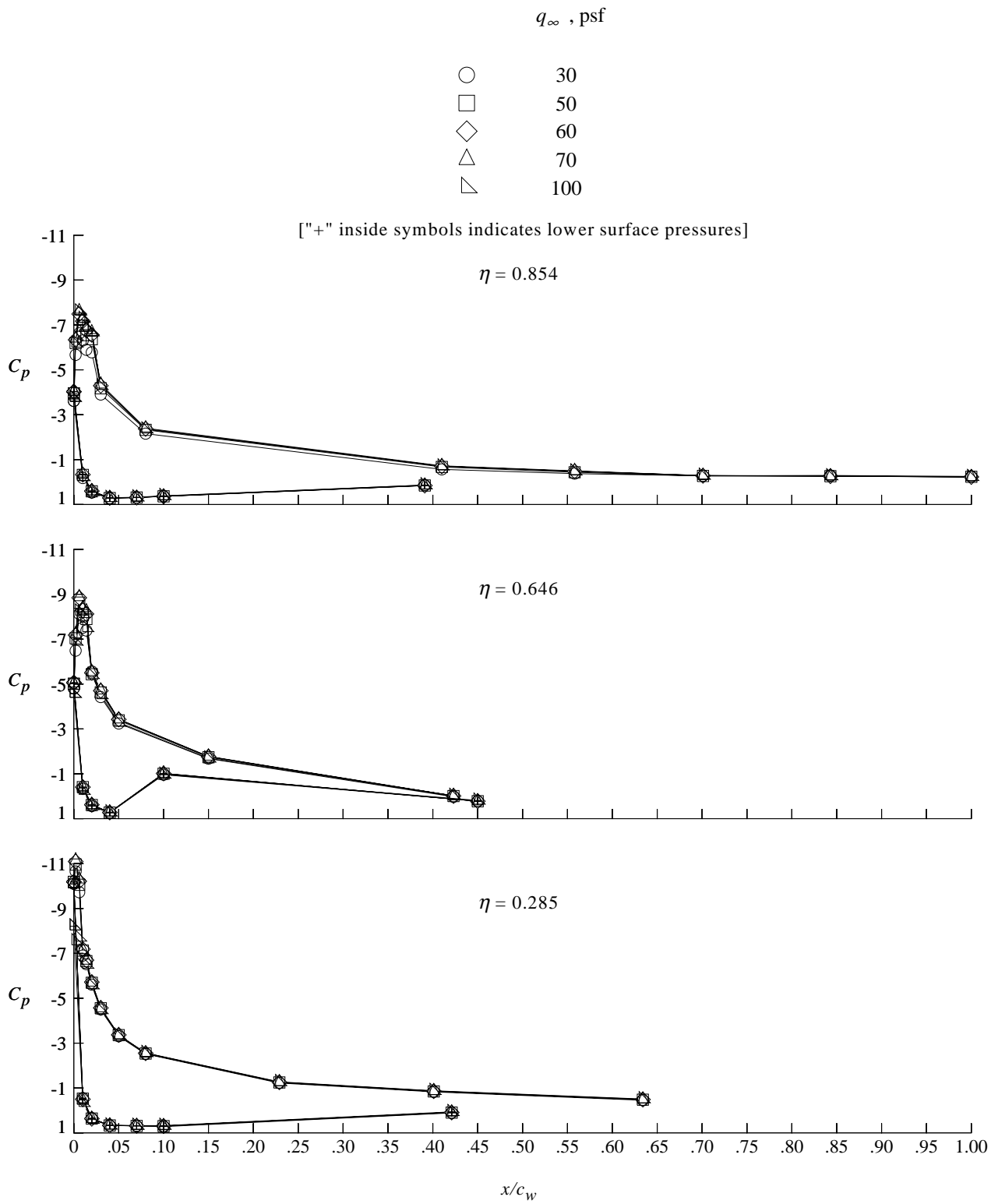
(c) $\alpha = 8^\circ$.

Figure 10. Continued.



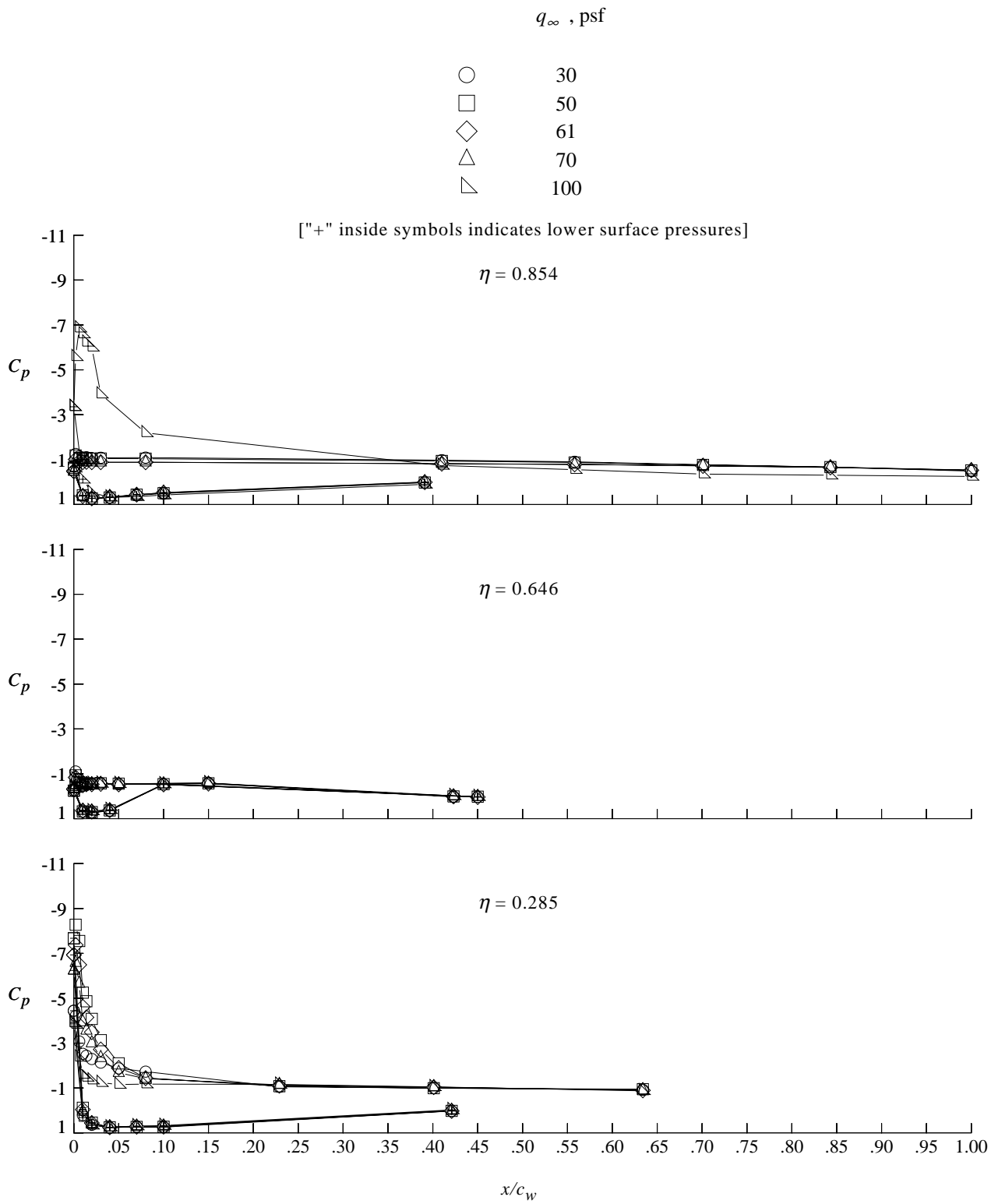
(d) $\alpha = 12^\circ$.

Figure 10. Continued.



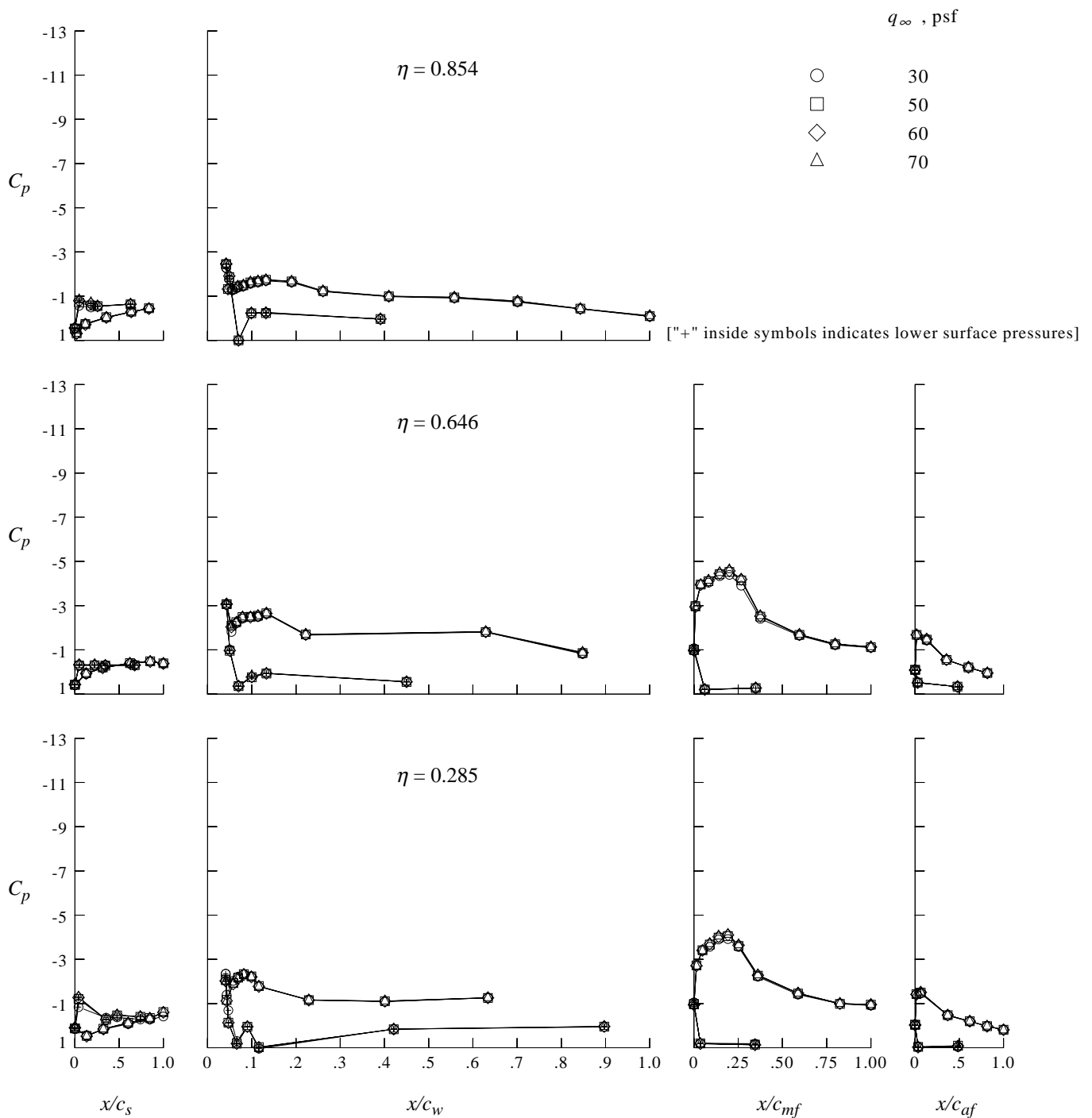
(e) $\alpha = 14^\circ$.

Figure 10. Continued.



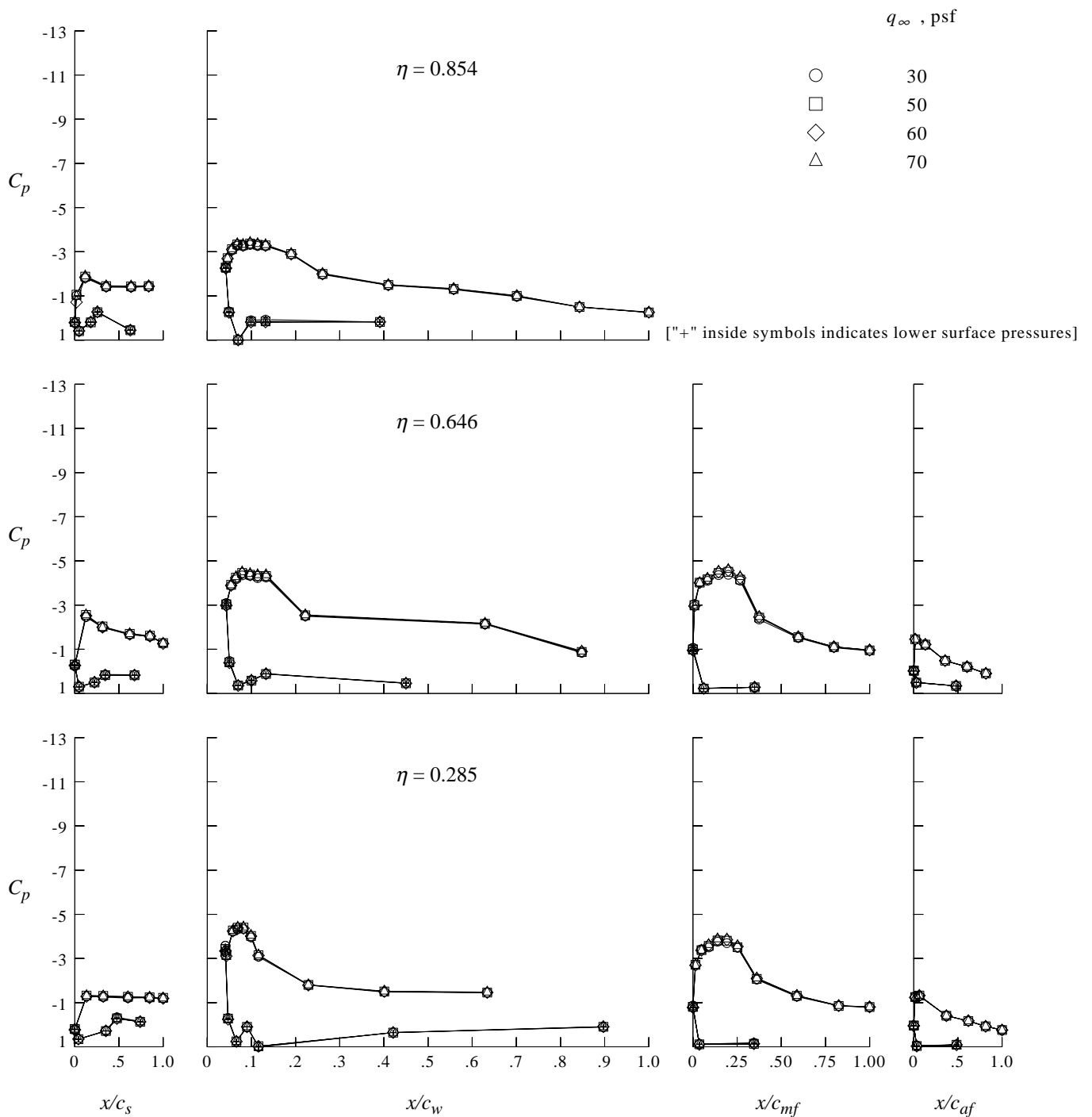
(f) $\alpha = 16^\circ$.

Figure 10. Concluded.



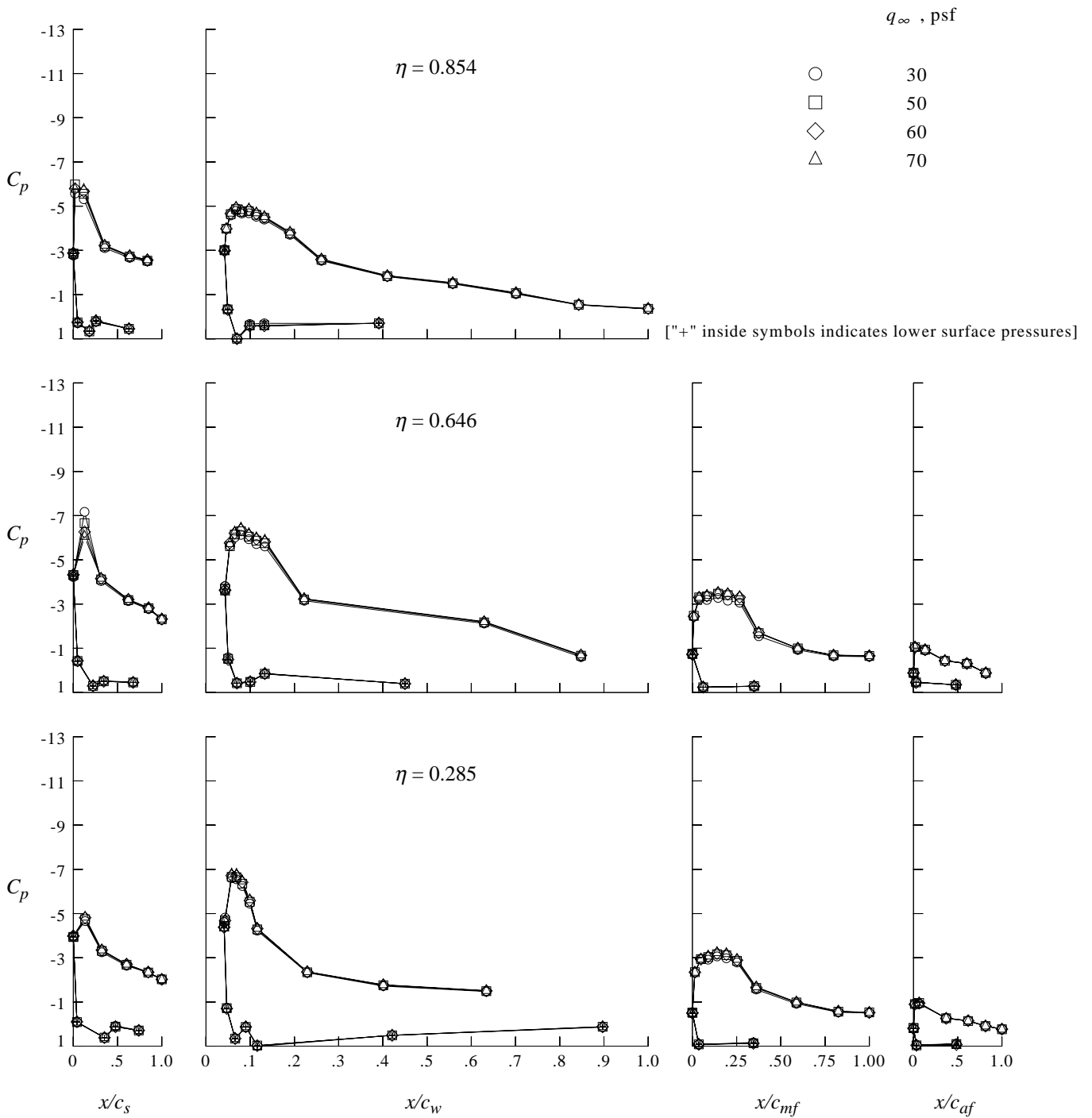
(a) $\alpha = 0^\circ$.

Figure 11. Free-stream speed effect on high-lift wing pressure distributions. Tunnel floor boundary layer suction off.



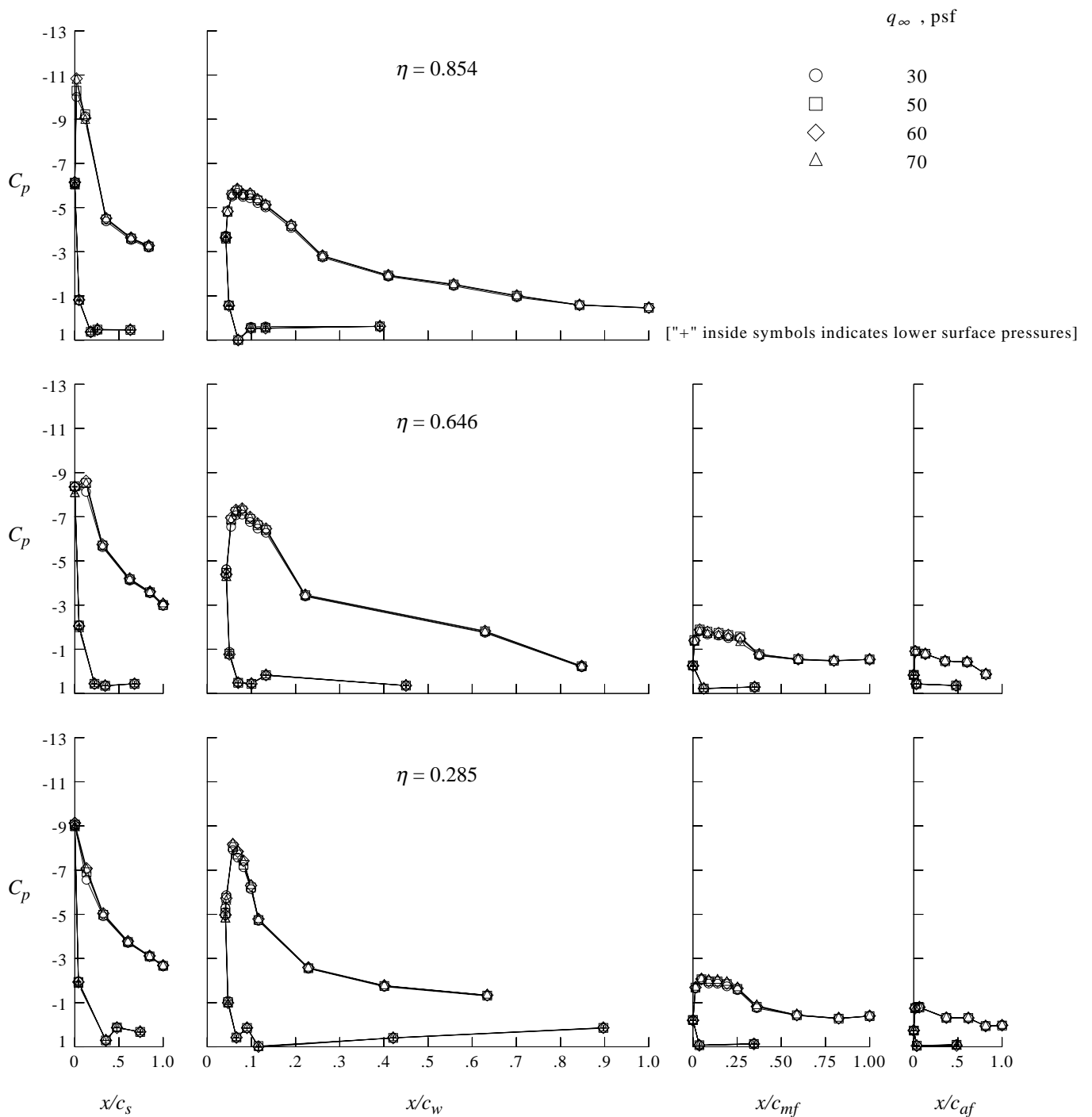
(b) $\alpha = 8^\circ$.

Figure 11. Continued.



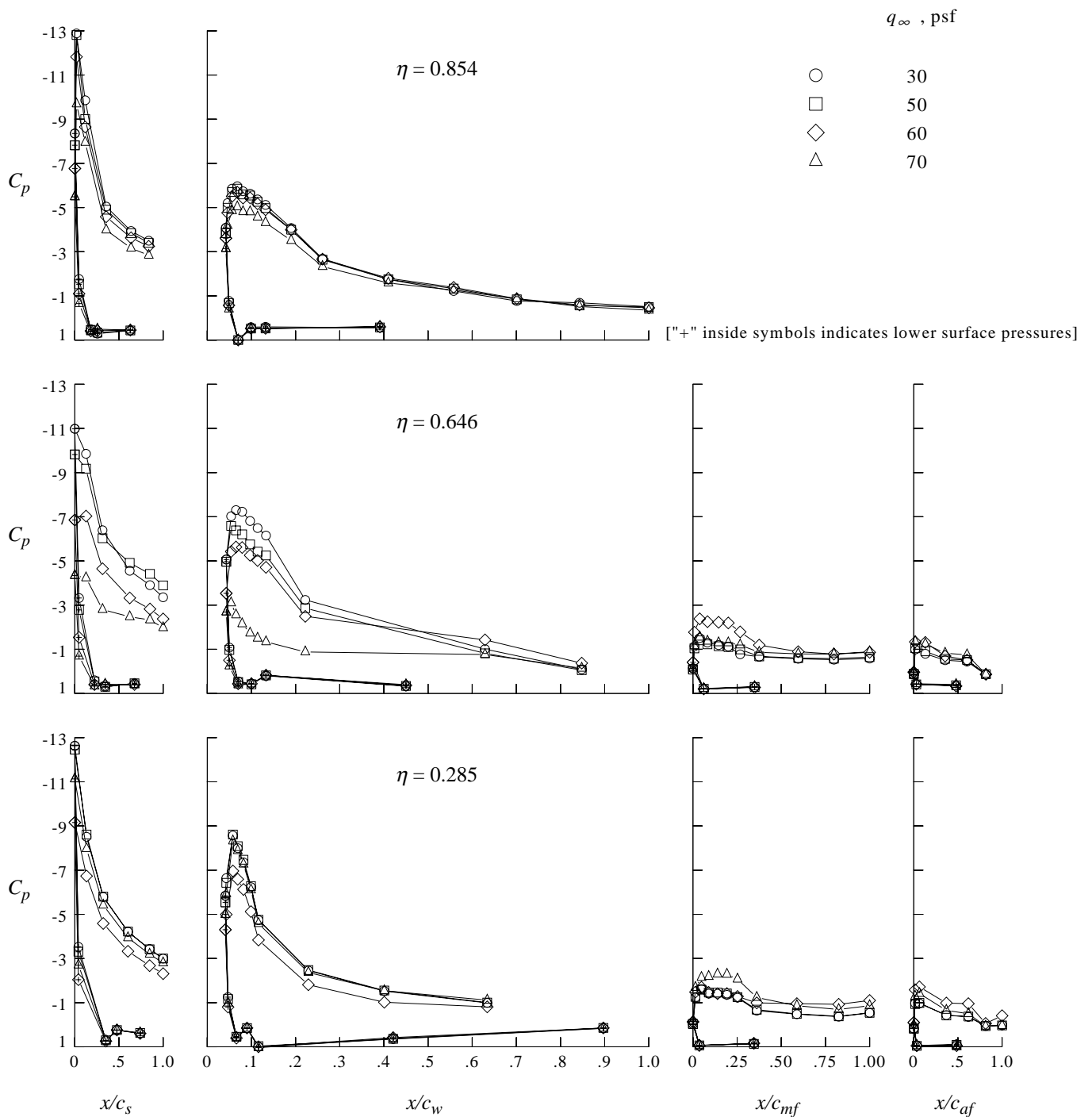
(c) $\alpha = 16^\circ$.

Figure 11. Continued.



(d) $\alpha = 22^\circ$.

Figure 11. Continued.



(e) $\alpha = 26^\circ$.

Figure 11. Concluded.

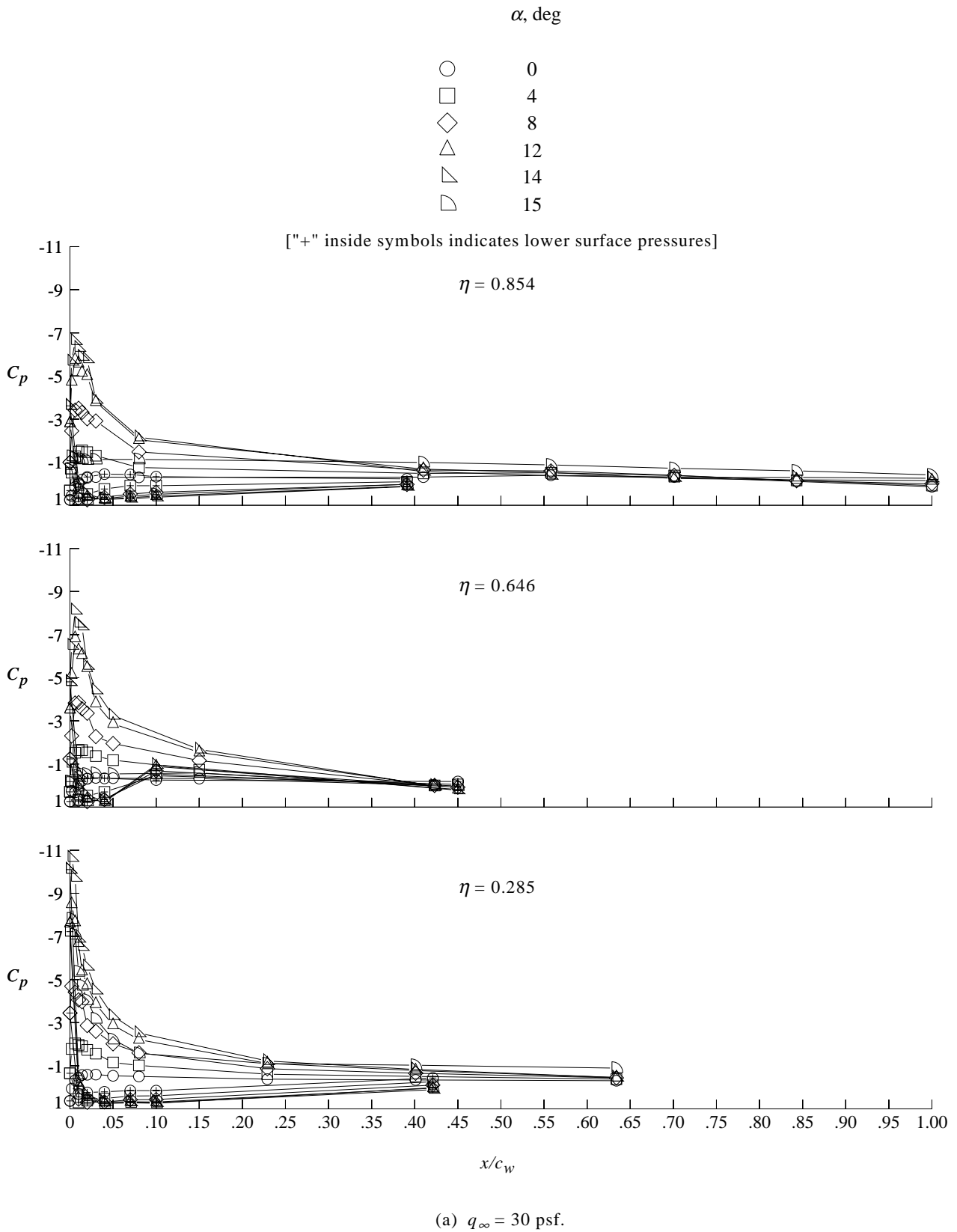
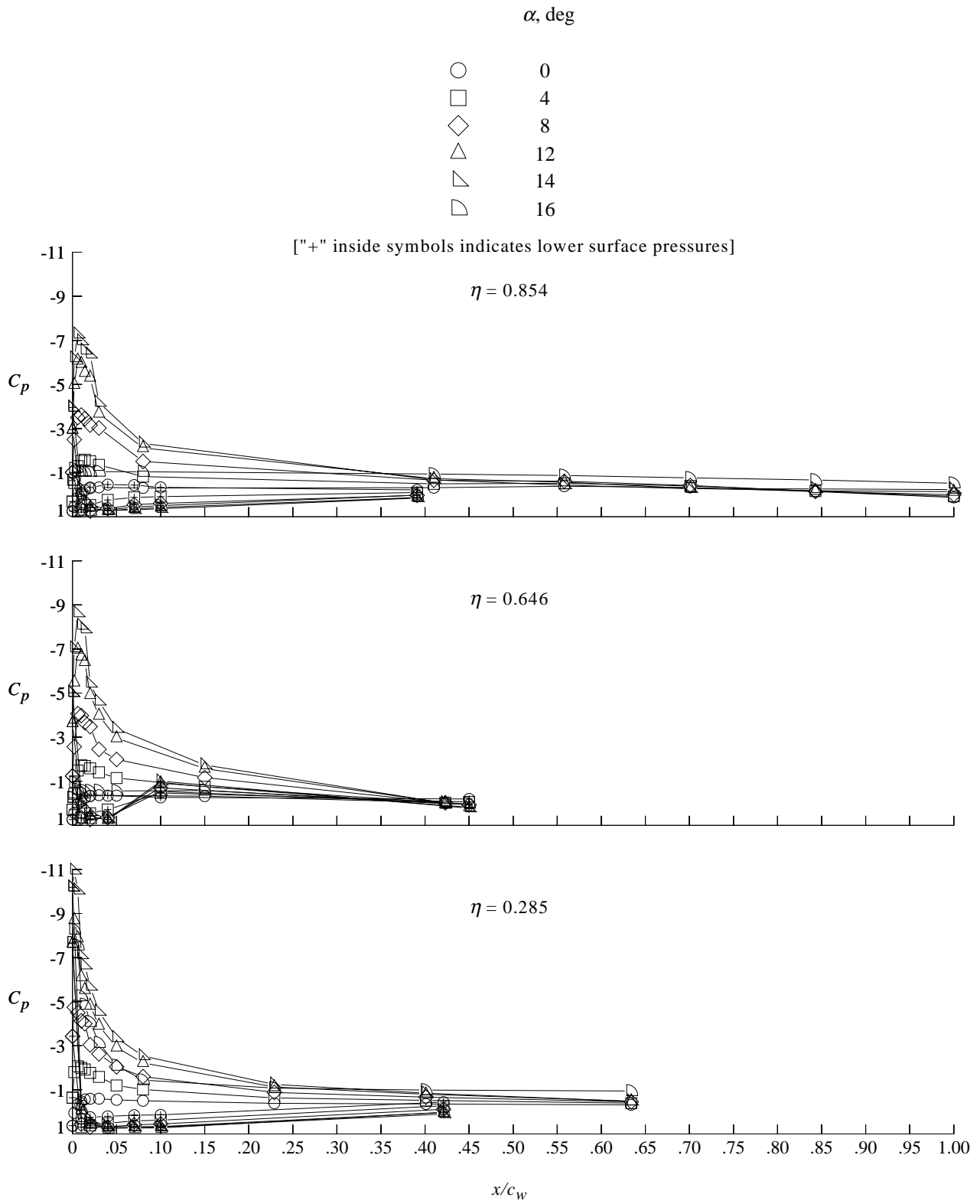
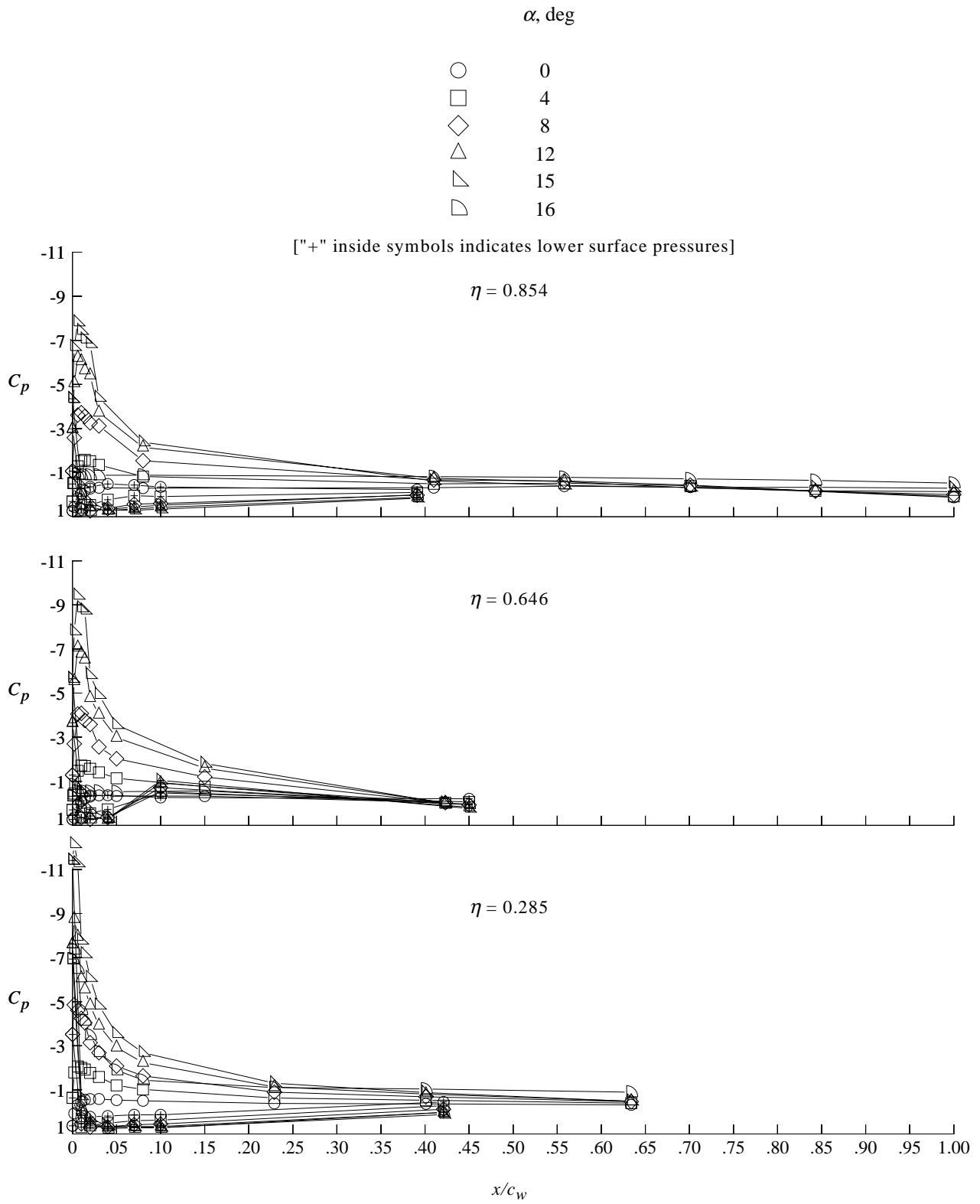


Figure 12. Angle of attack effect on cruise wing pressure distributions. Tunnel floor boundary layer suction off.



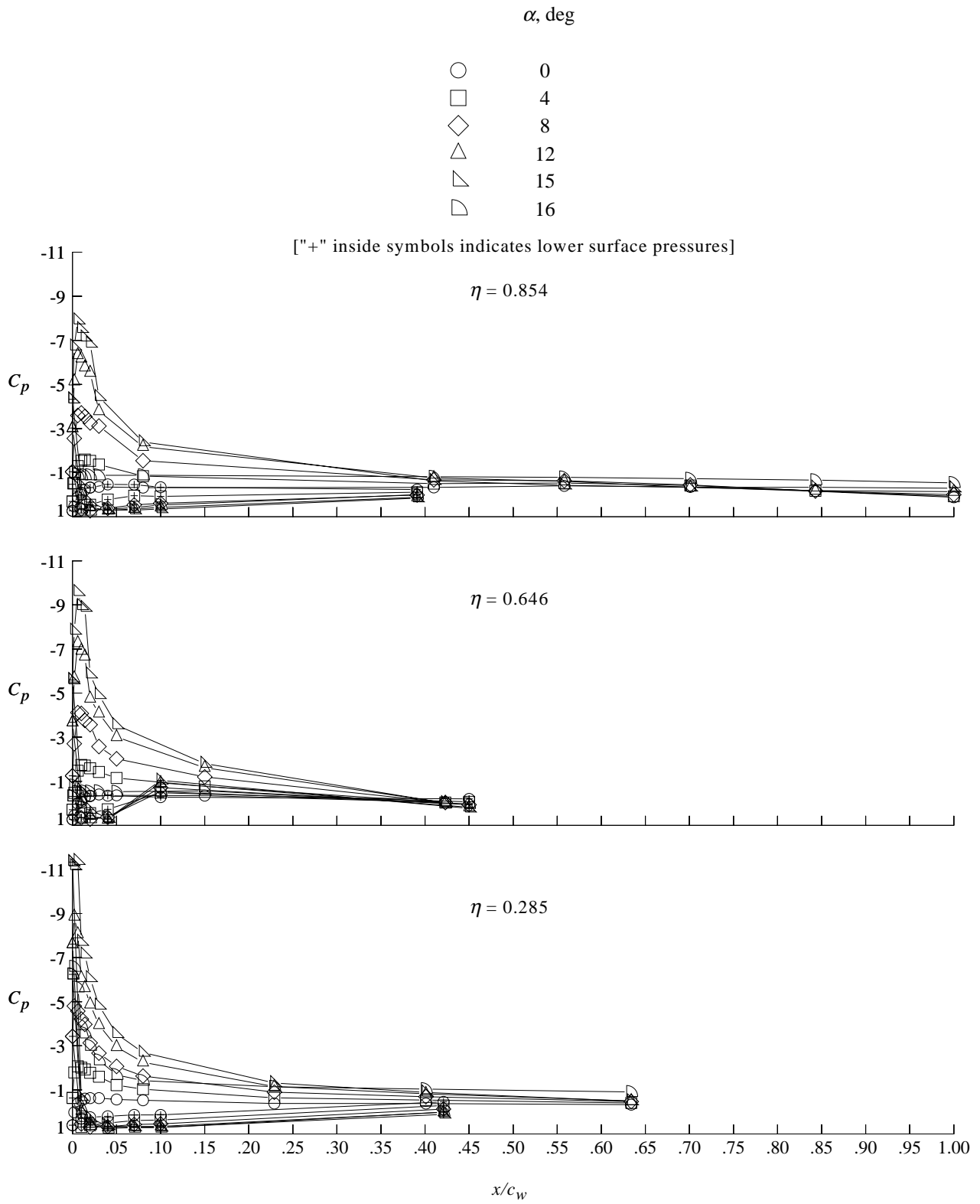
(b) $q_\infty = 50$ psf.

Figure 12. Continued.



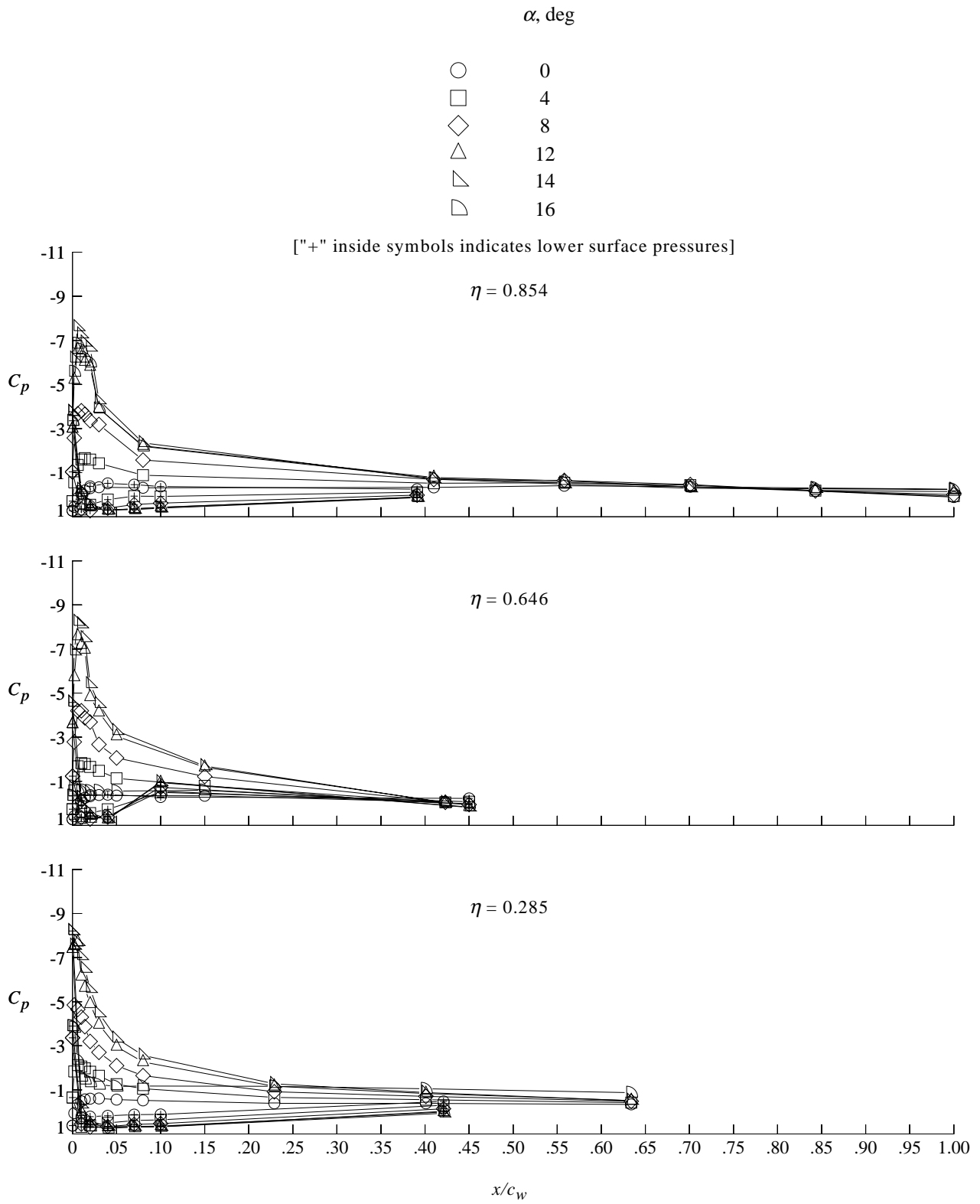
(c) $q_\infty = 60$ psf.

Figure 12. Continued.



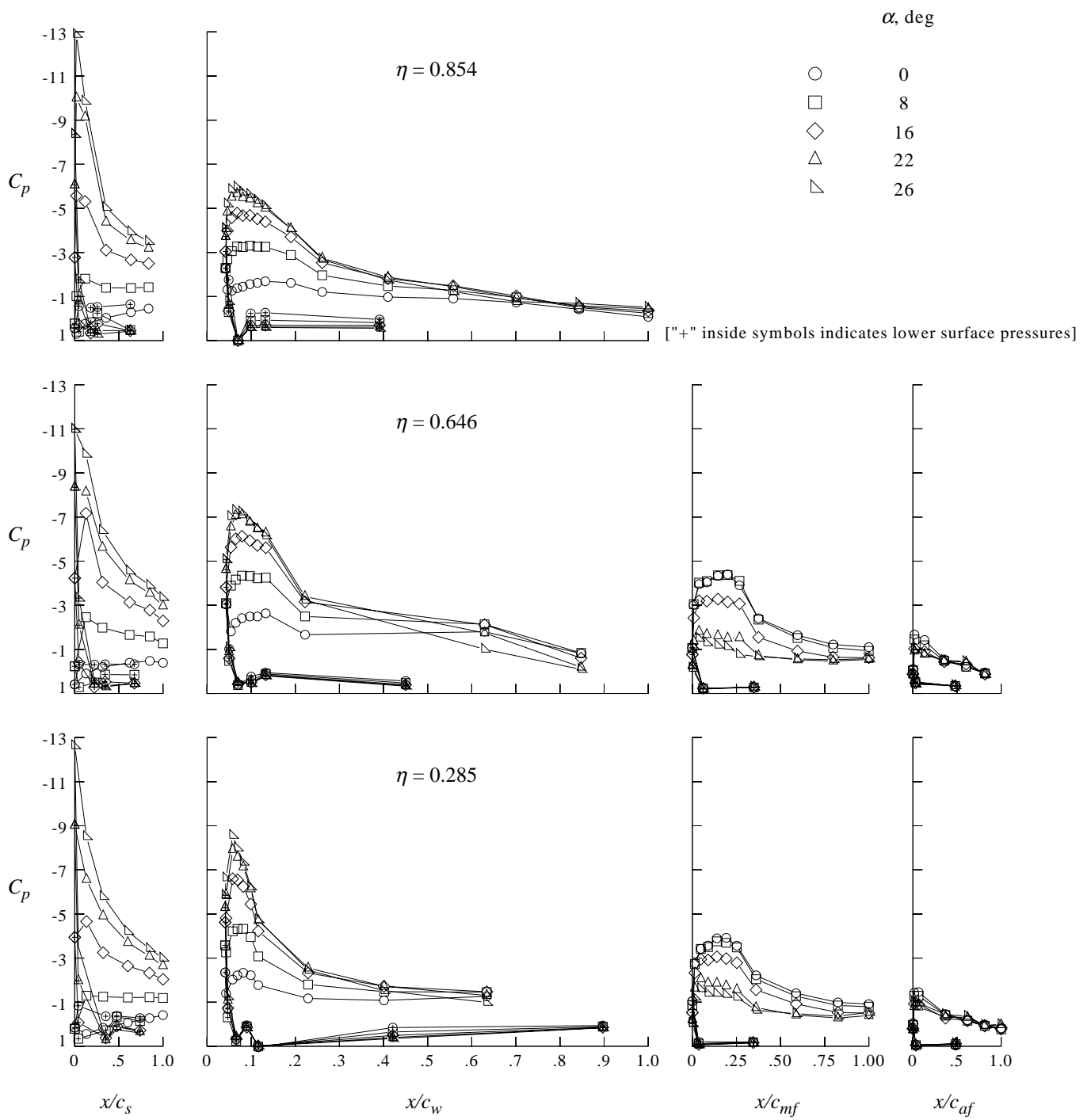
(d) $q_\infty = 70$ psf.

Figure 12. Continued.



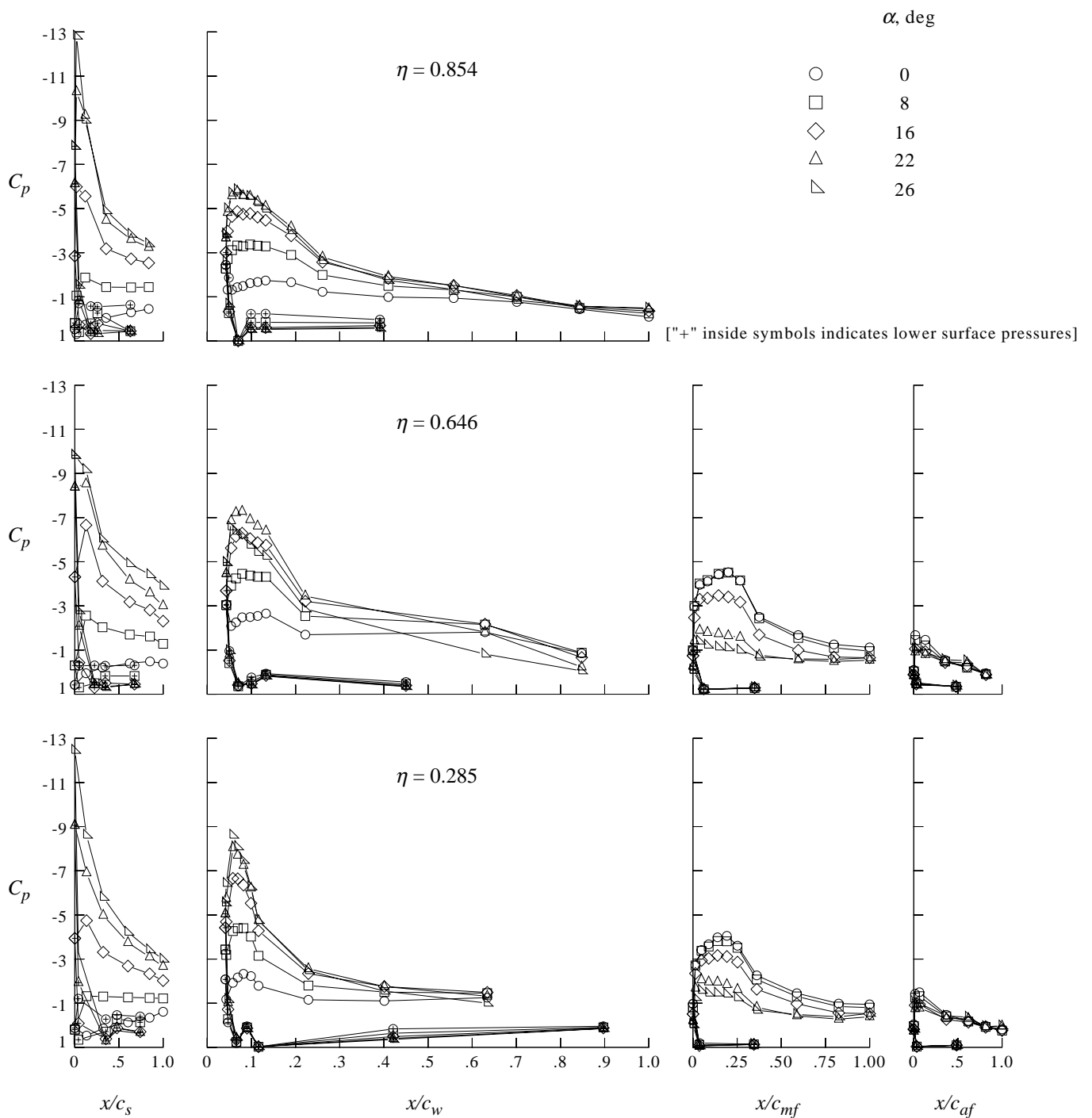
(e) $q_\infty = 100$ psf.

Figure 12. Concluded.



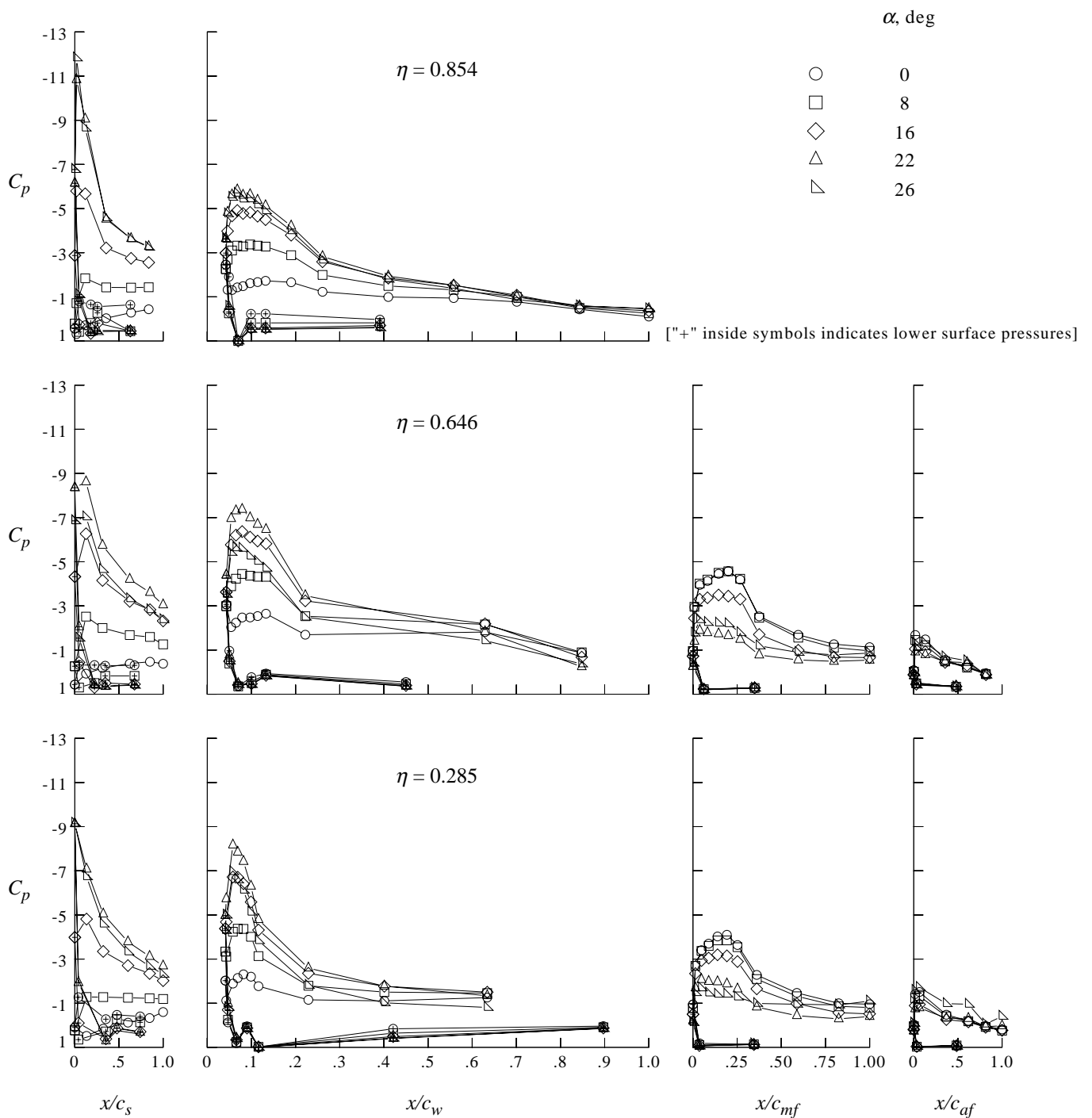
(a) $q_\infty = 30$ psf.

Figure 13. Angle of attack effect on high-lift wing pressure distributions. Tunnel floor boundary layer suction off.



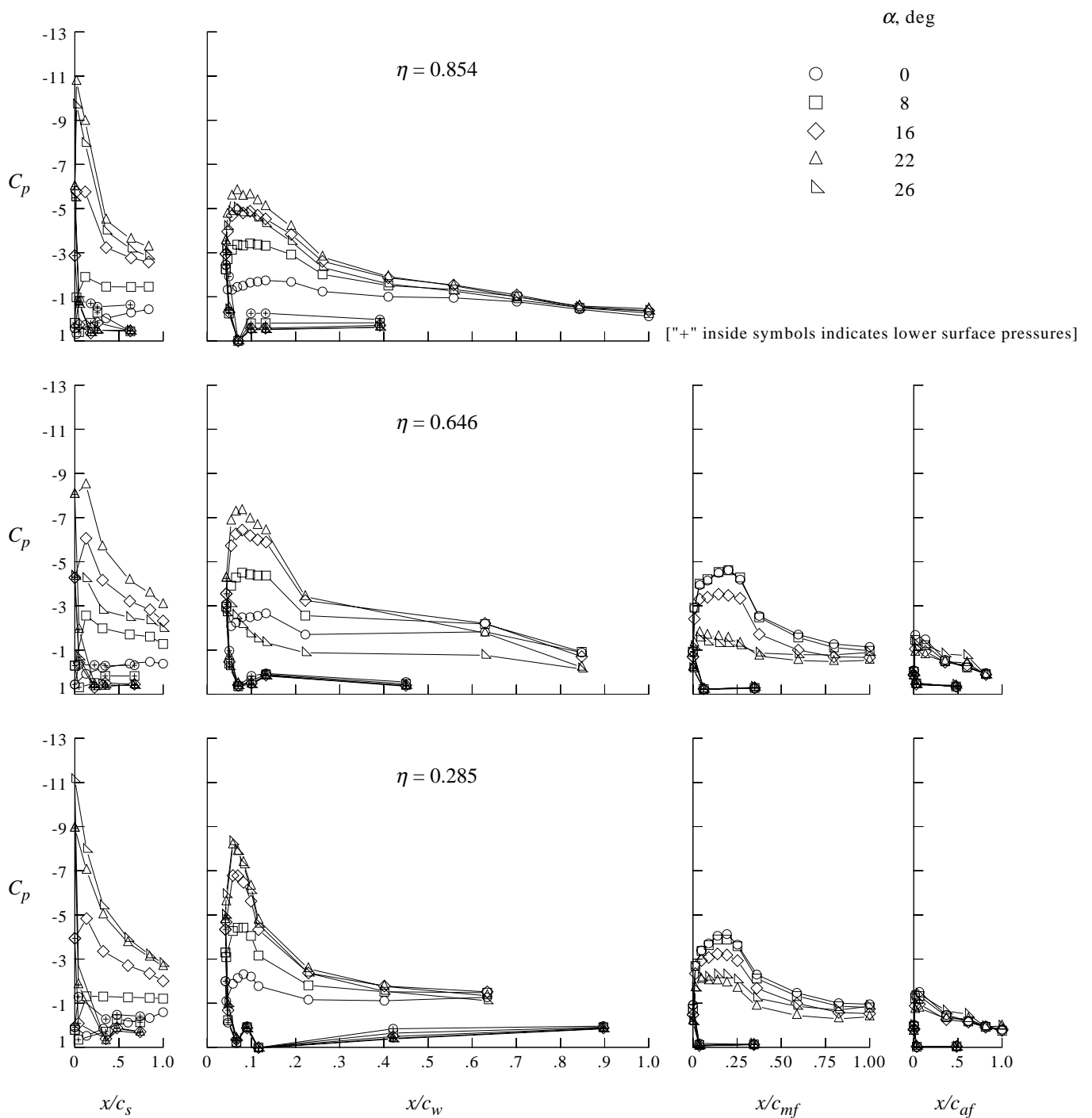
(b) $q_\infty = 50$ psf.

Figure 13. Continued.



(c) $q_\infty = 60$ psf.

Figure 13. Continued.



(d) $q_\infty = 70$ psf.

Figure 13. Concluded.

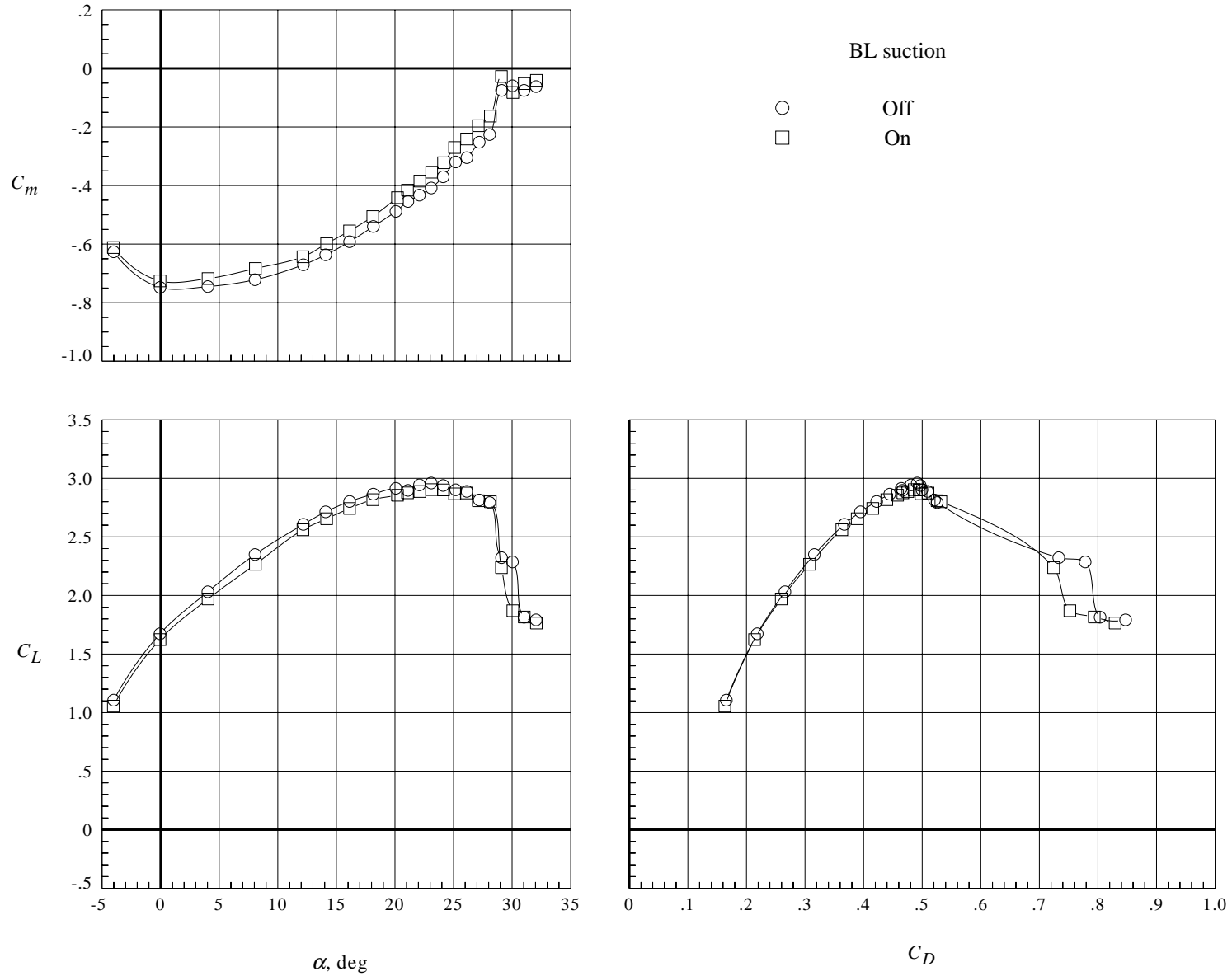
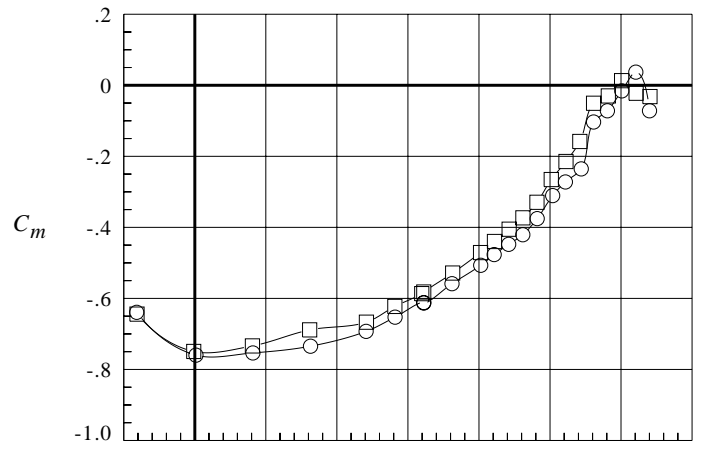
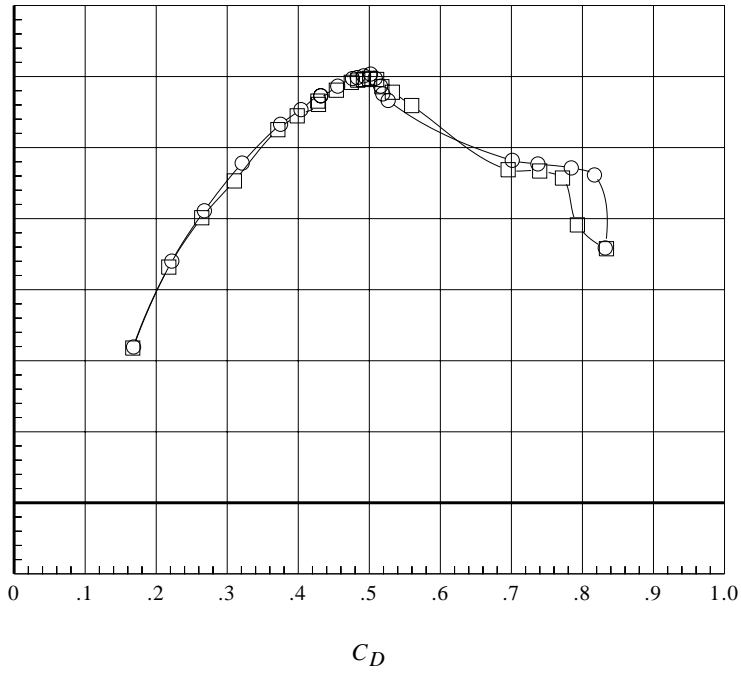
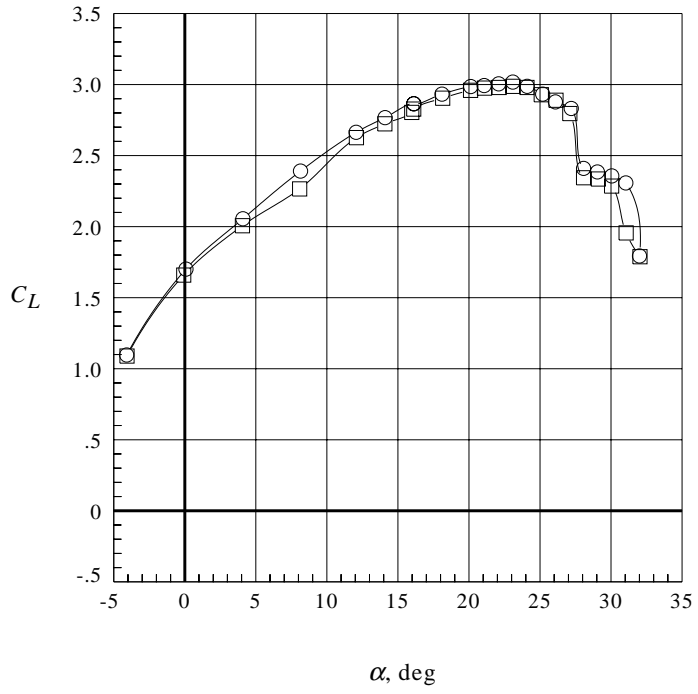
(a) $q_\infty = 30$ psf.

Figure 16. Tunnel floor boundary layer thickness reduction effect on transport model longitudinal aerodynamic coefficients with high-lift wing.

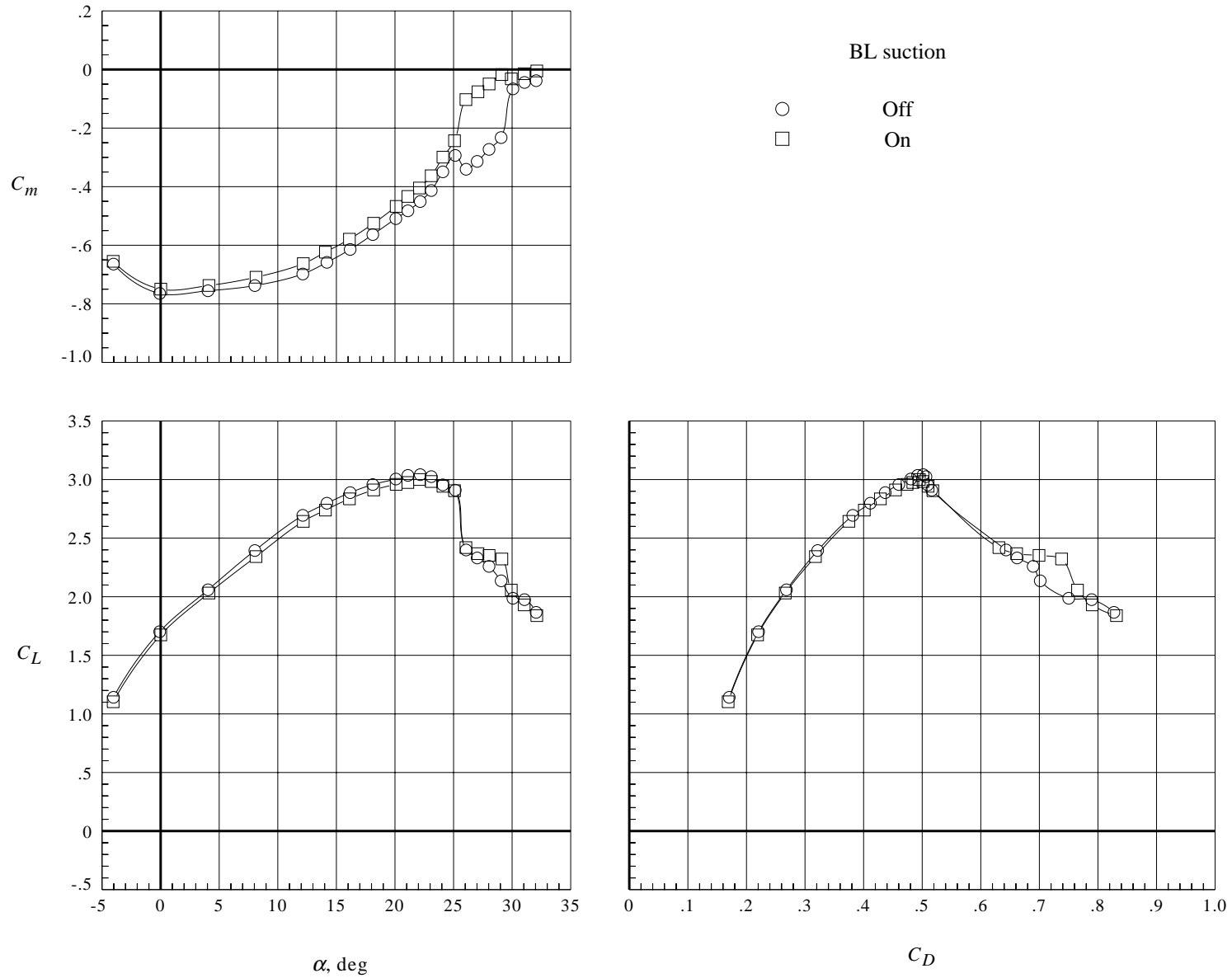


BL suction
 ○ Off
 □ On



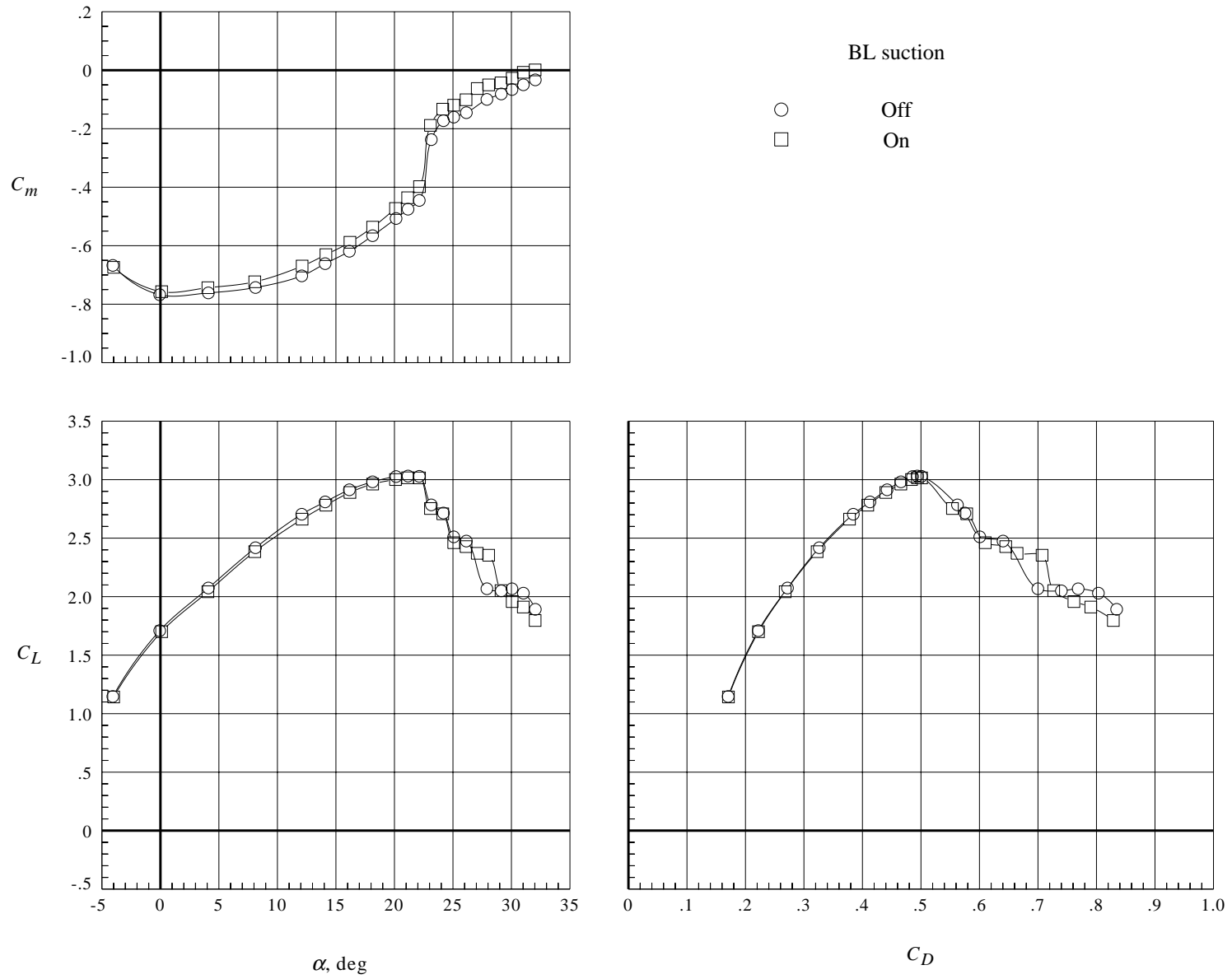
(b) $q_\infty = 50$ psf.

Figure 16. Continued.



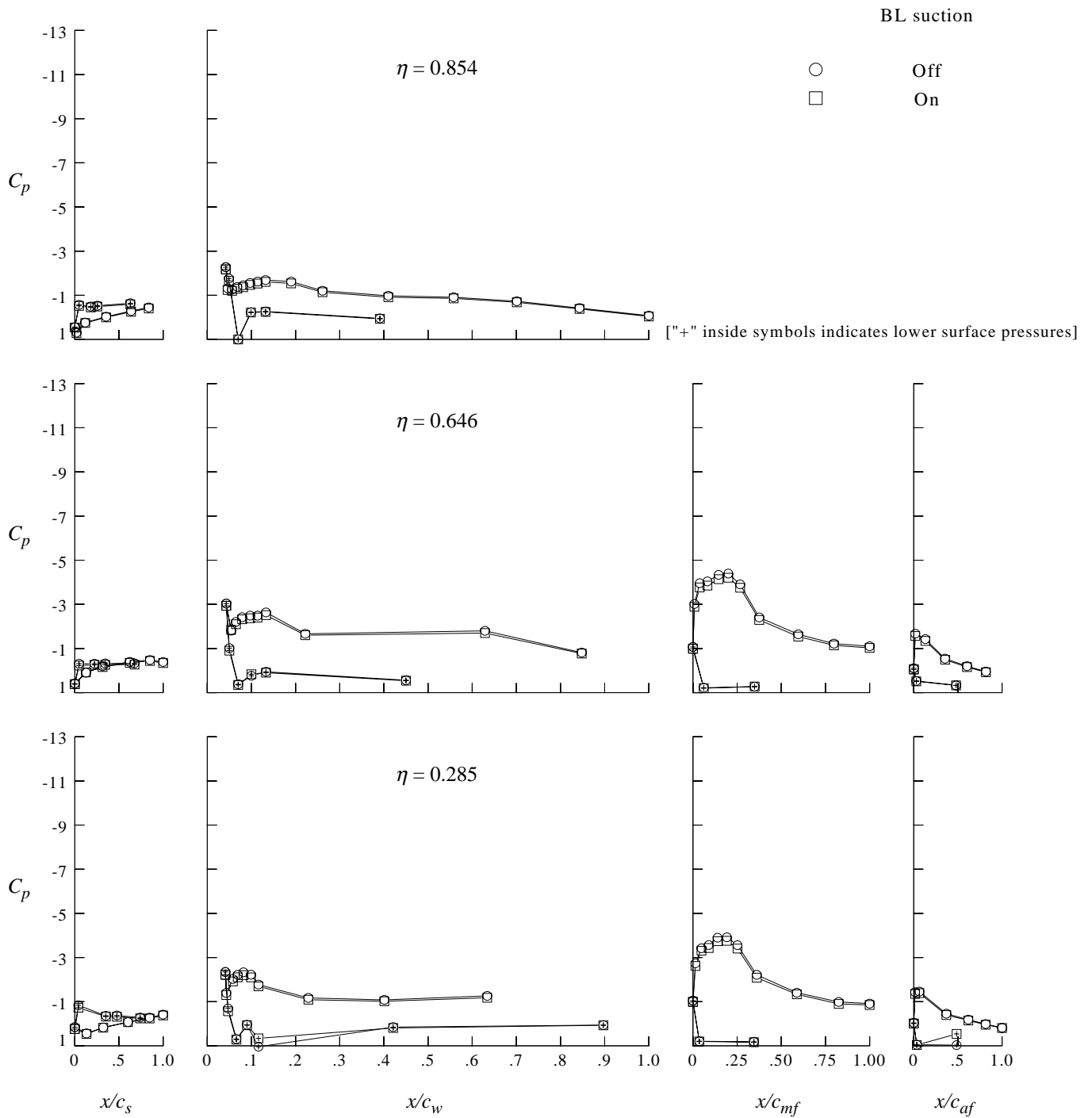
(c) $q_\infty = 60$ psf.

Figure 16. Continued.



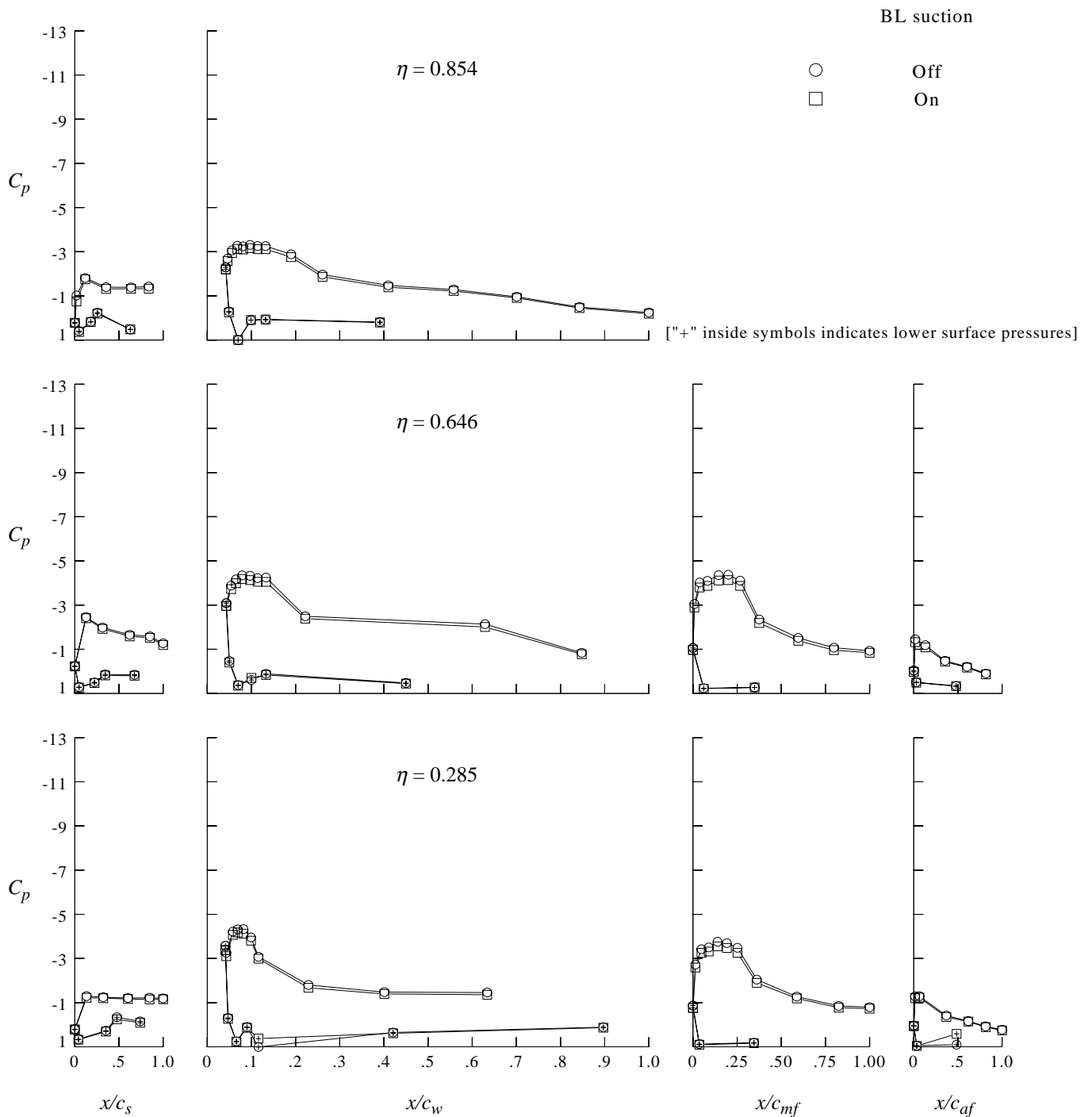
(d) $q_\infty = 70$ psf.

Figure 16. Concluded.



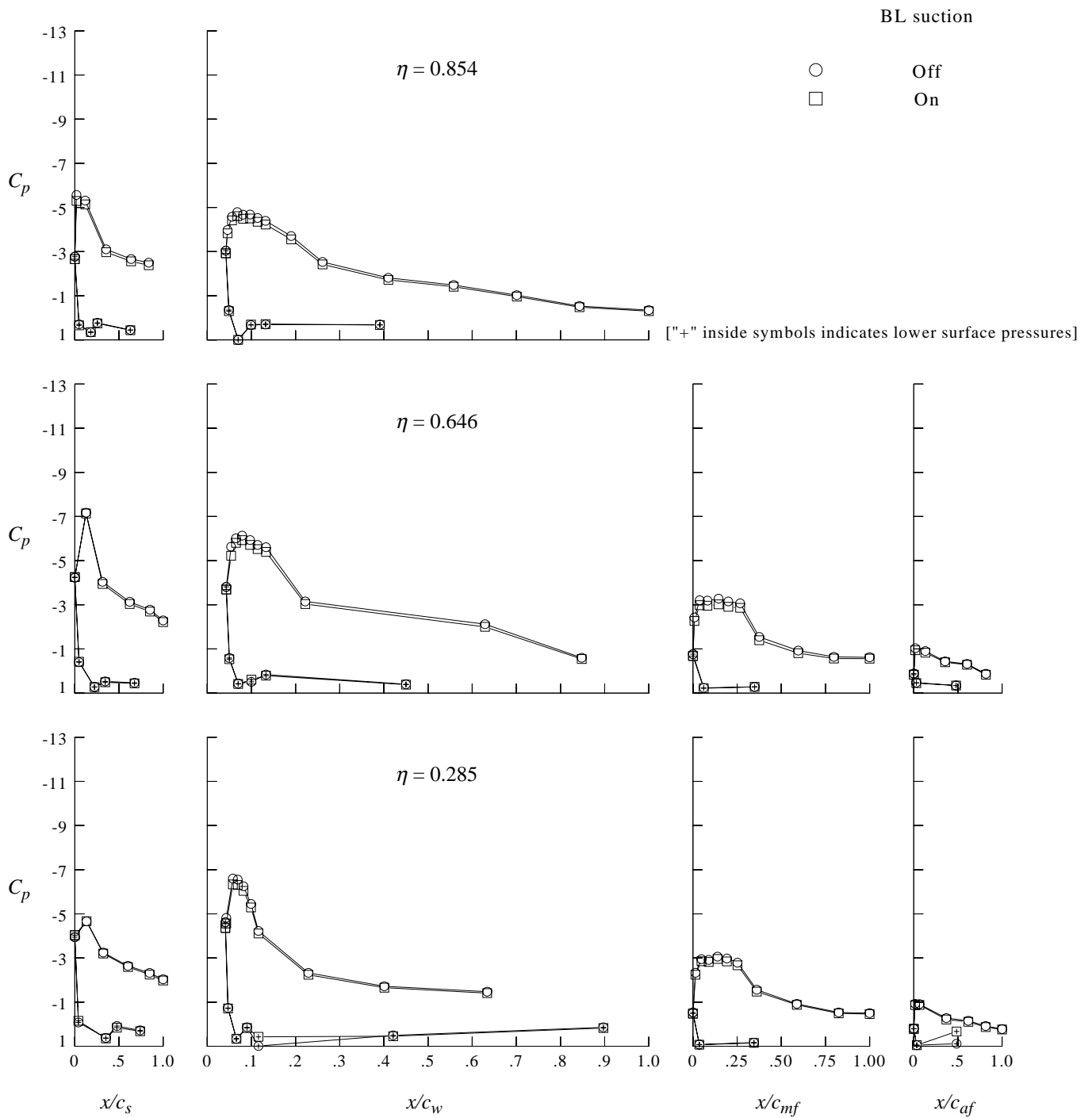
(a) $\alpha = 0^\circ$.

Figure 17. Tunnel floor boundary layer thickness reduction effect on high-lift wing pressure distributions. $q_\infty = 30$ psf.



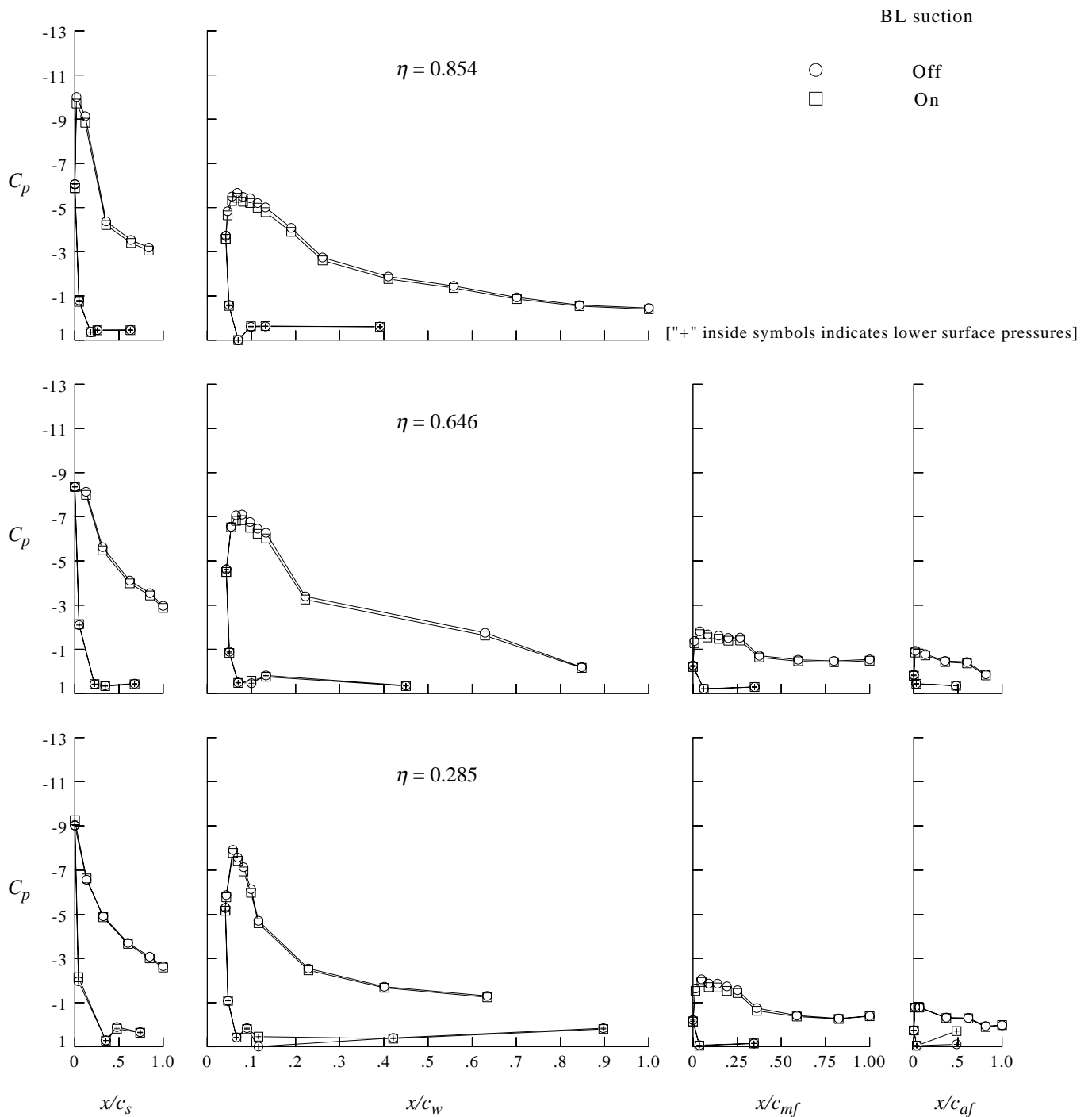
(b) $\alpha = 8^\circ$.

Figure 17. Continued.



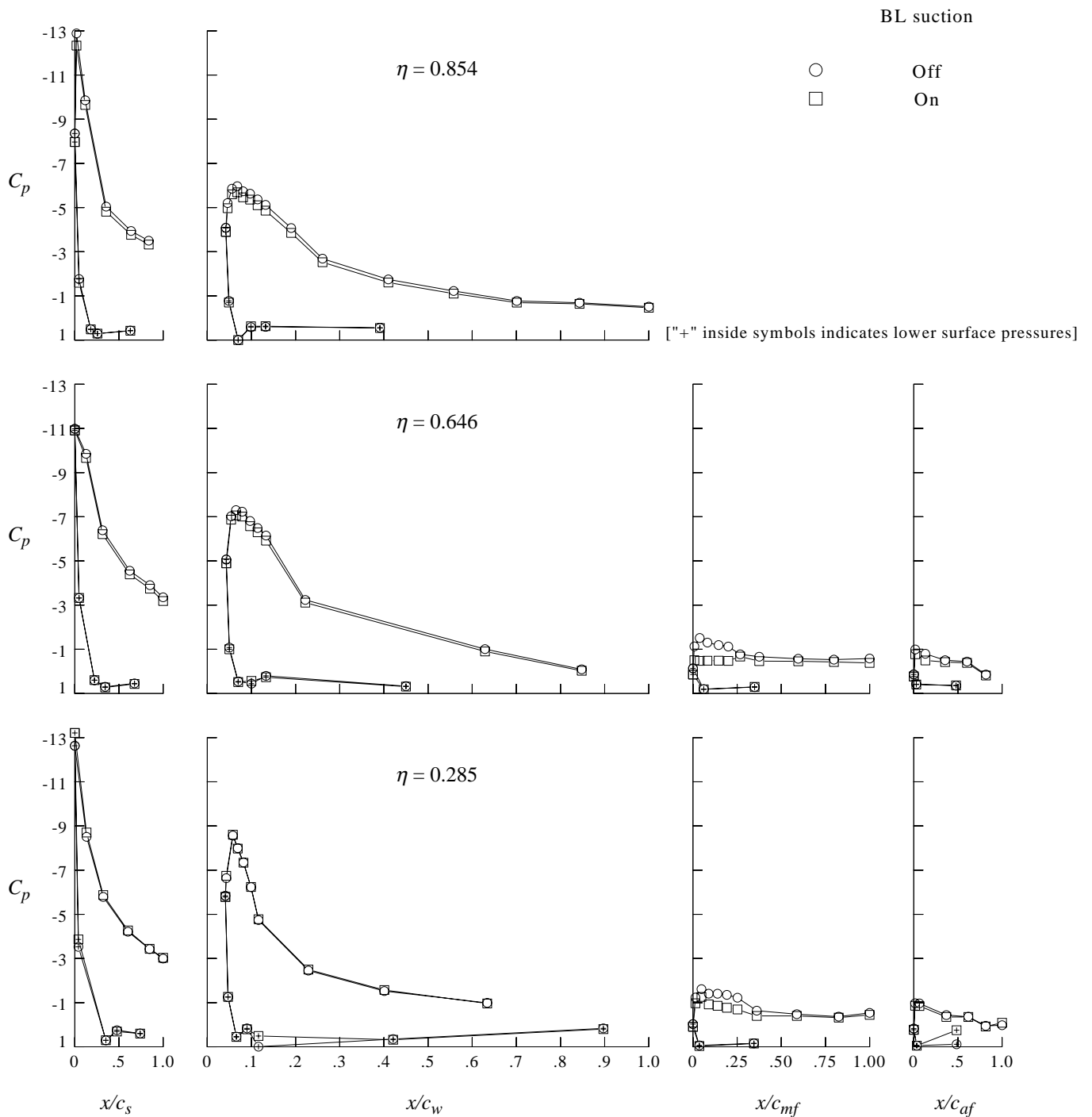
(c) $\alpha = 16^\circ$.

Figure 17. Continued.



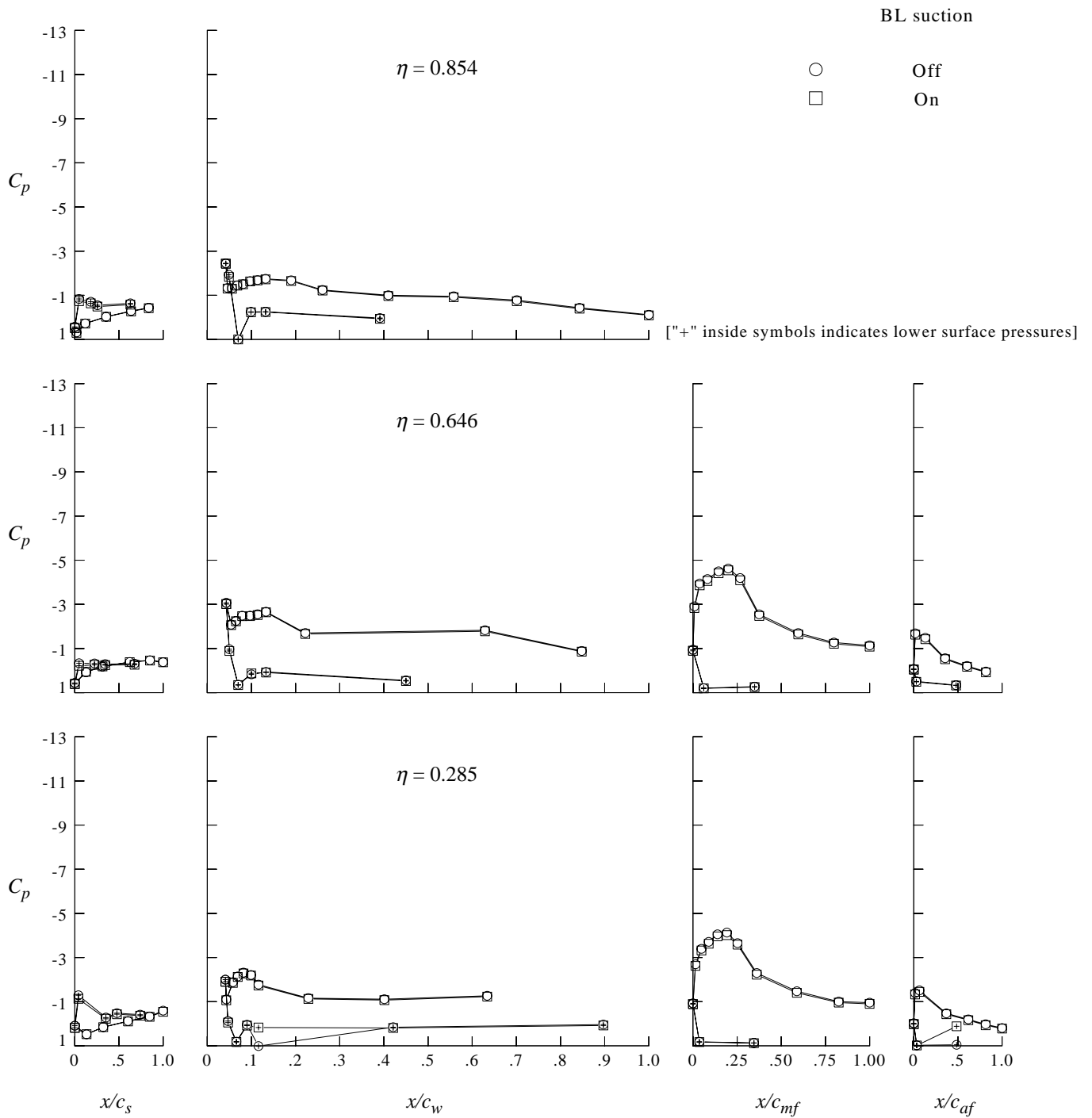
(d) $\alpha = 22^\circ$.

Figure 17. Continued.



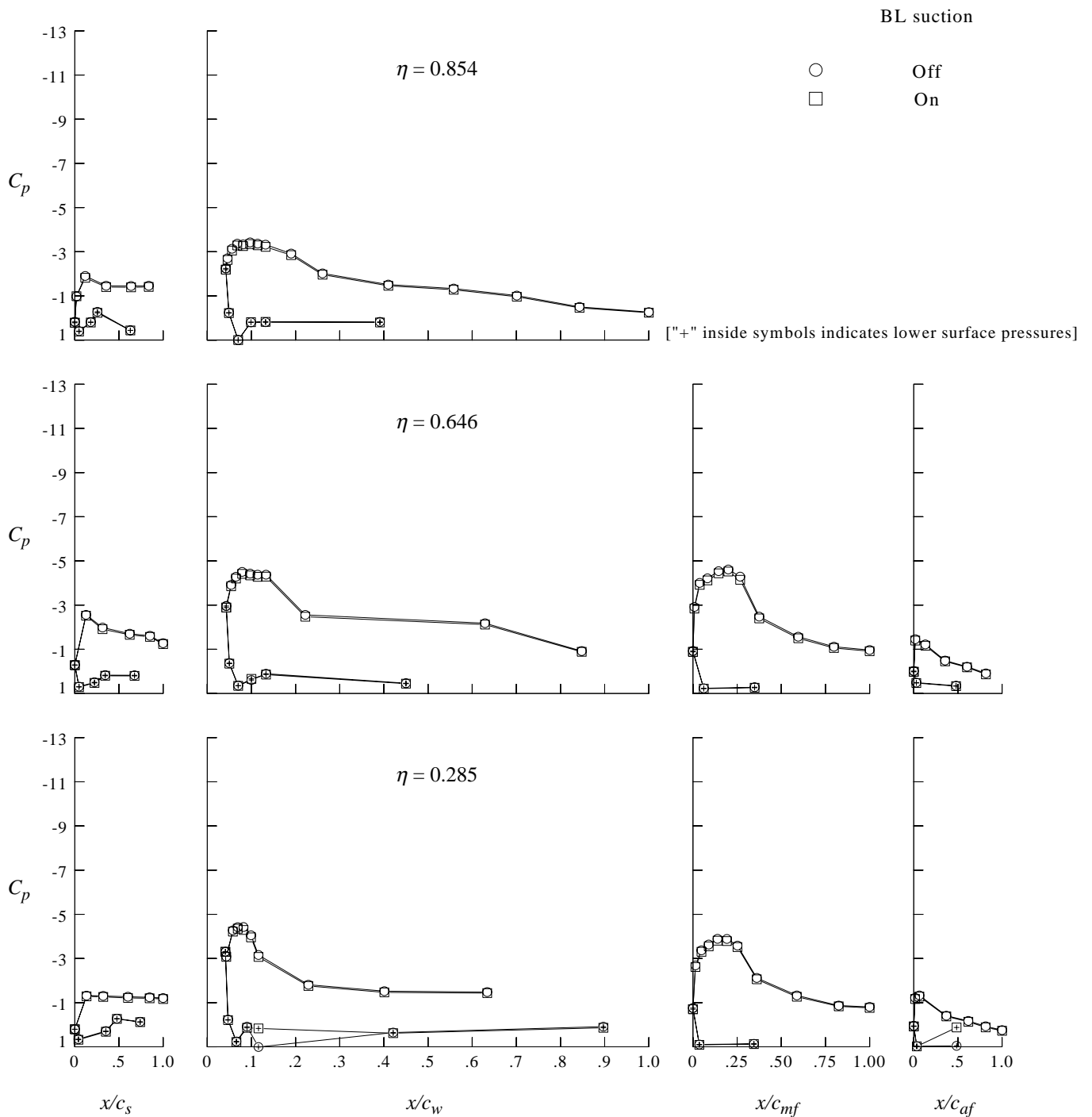
(e) $\alpha = 26^\circ$.

Figure 17. Concluded.



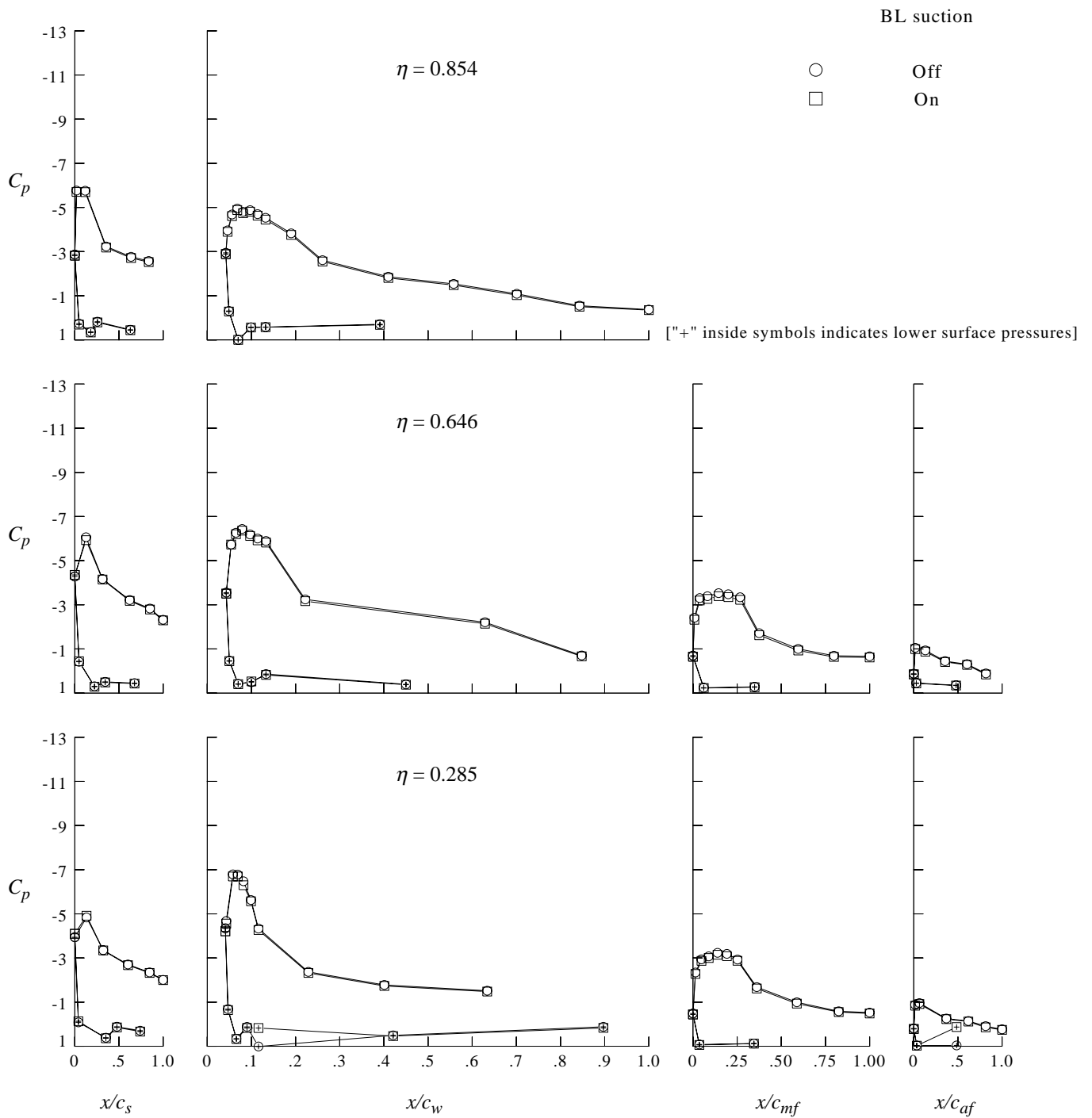
(a) $\alpha = 0^\circ$.

Figure 18. Tunnel floor boundary layer thickness reduction effect on high-lift wing pressure distributions. $q_\infty = 70$ psf.



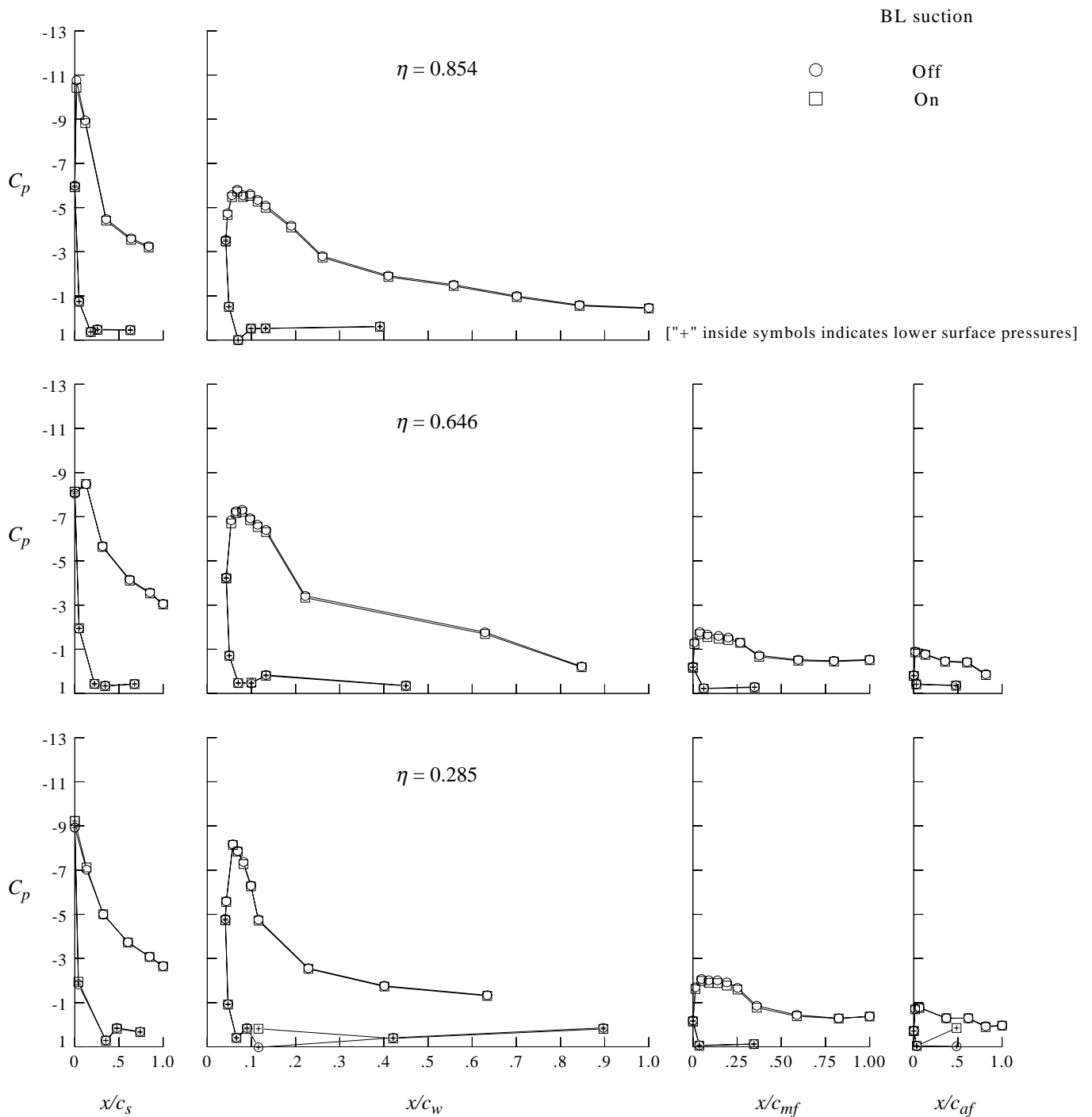
(b) $\alpha = 8^\circ$.

Figure 18. Continued.



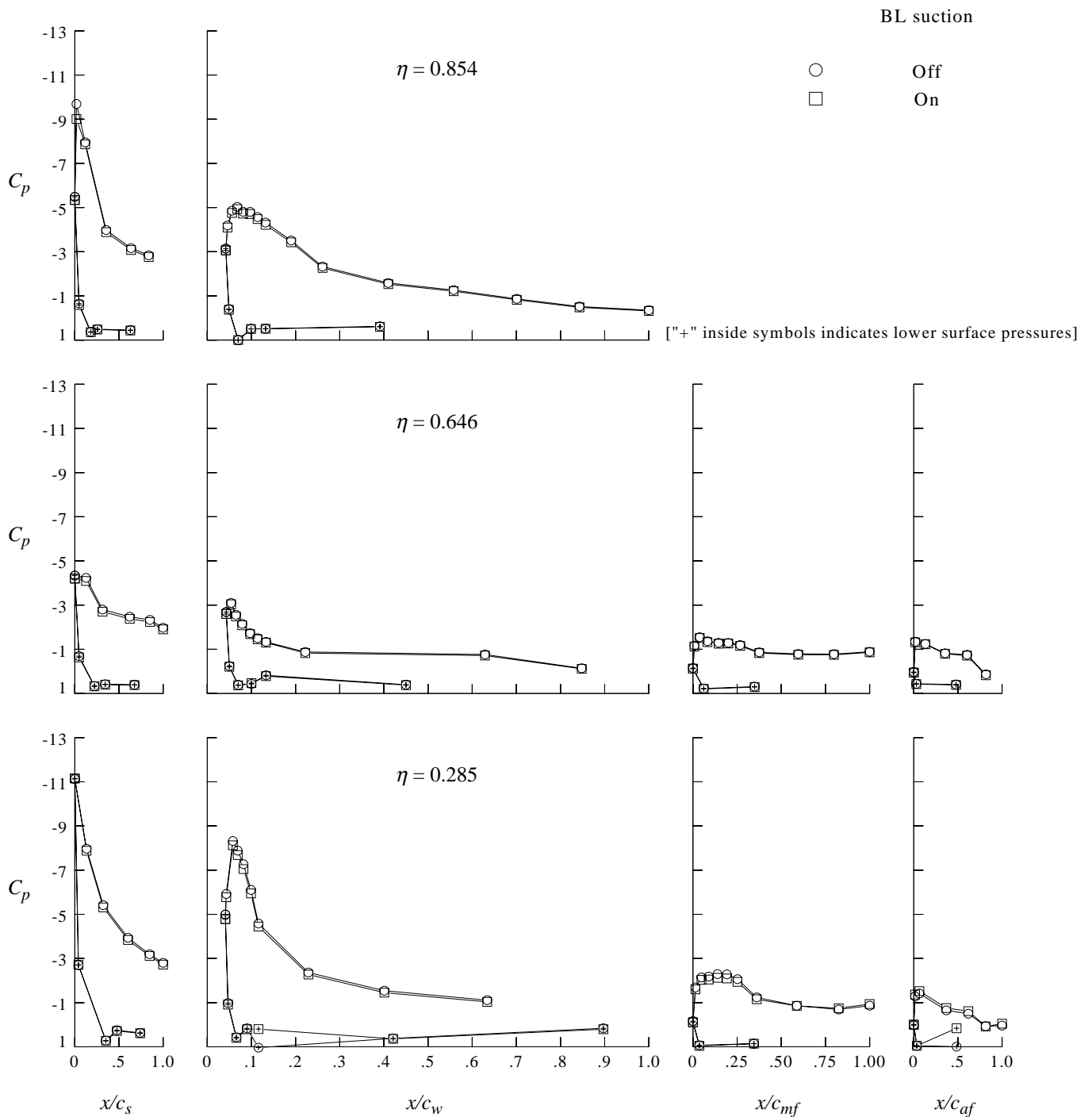
(c) $\alpha = 16^\circ$.

Figure 18. Continued.



(d) $\alpha = 22^\circ$.

Figure 18. Continued.



(e) $\alpha = 26^\circ$.

Figure 18. Concluded.

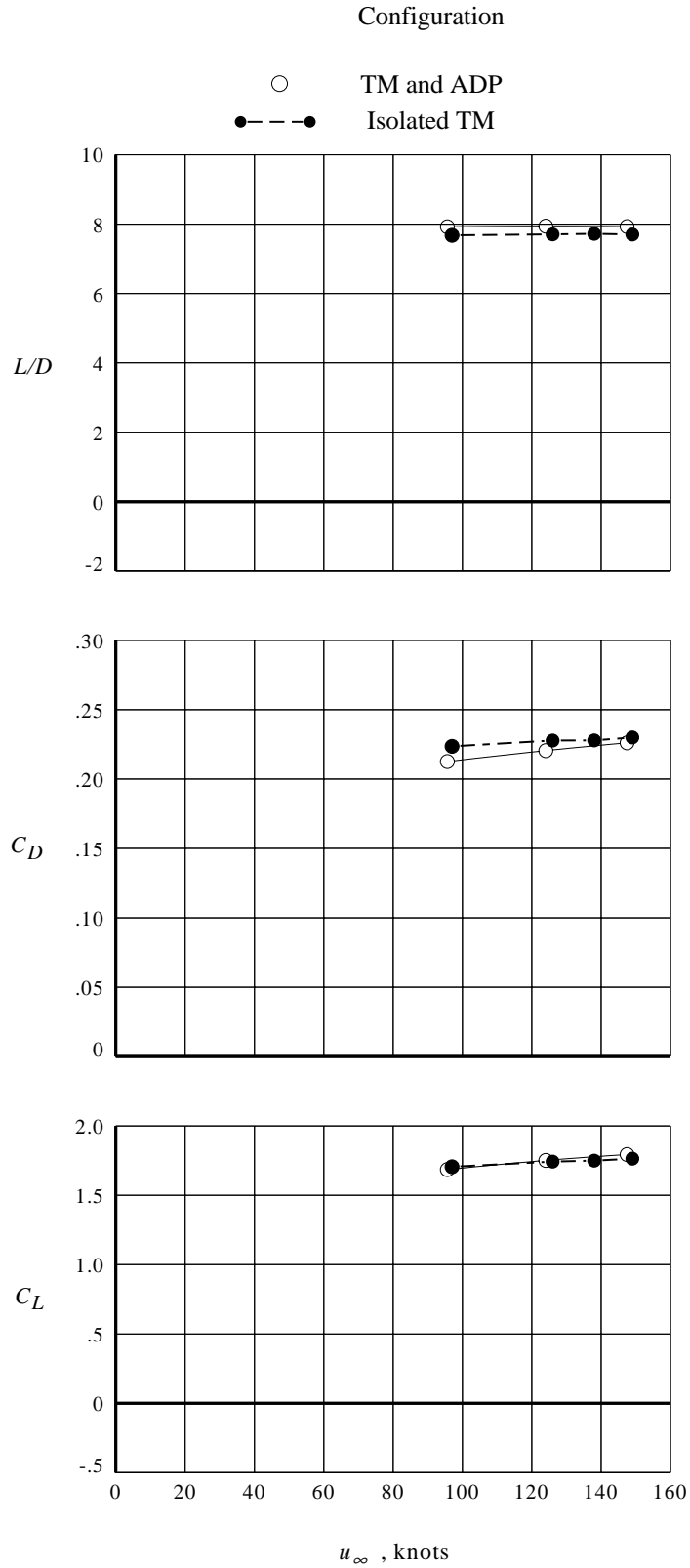
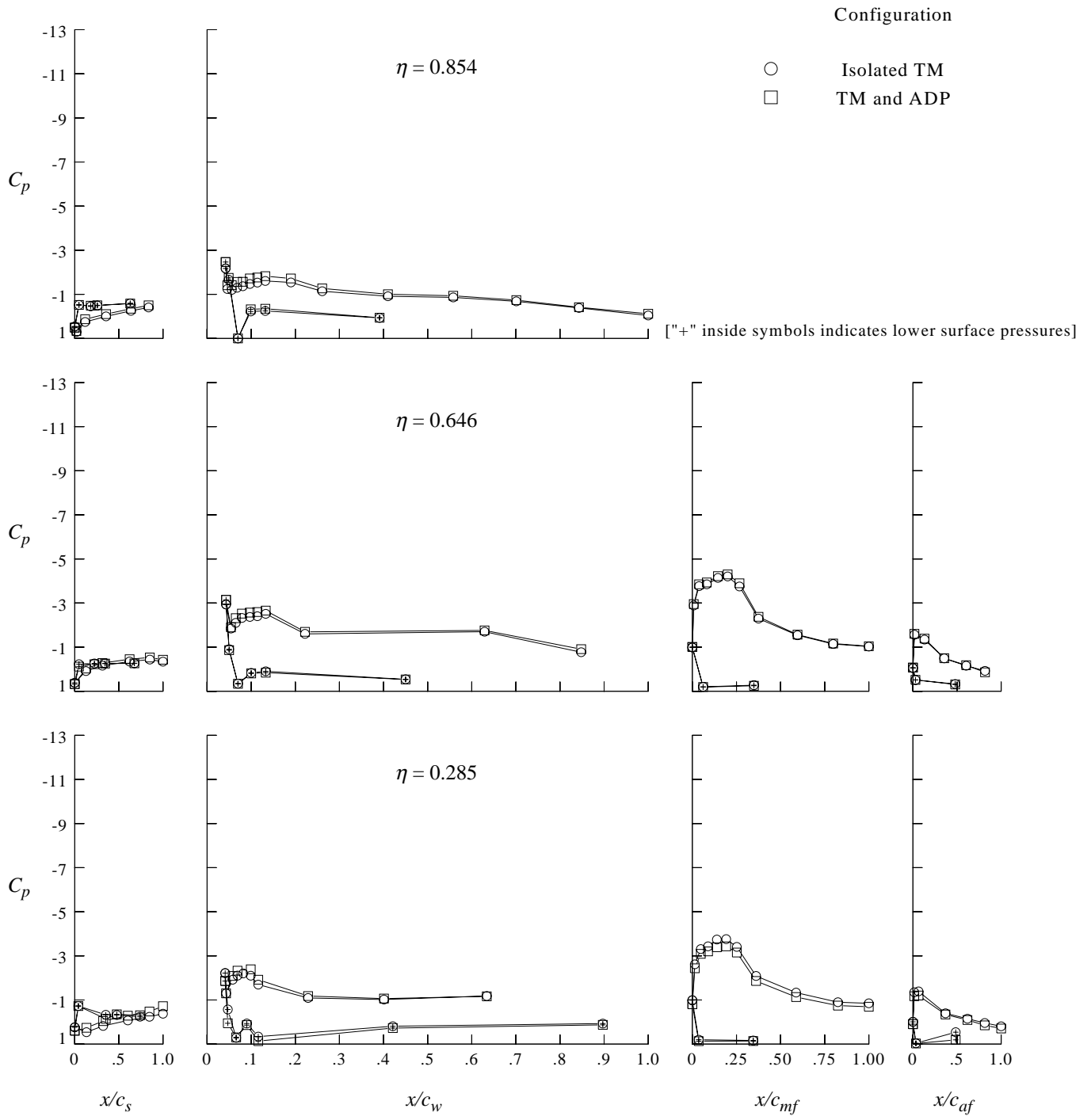
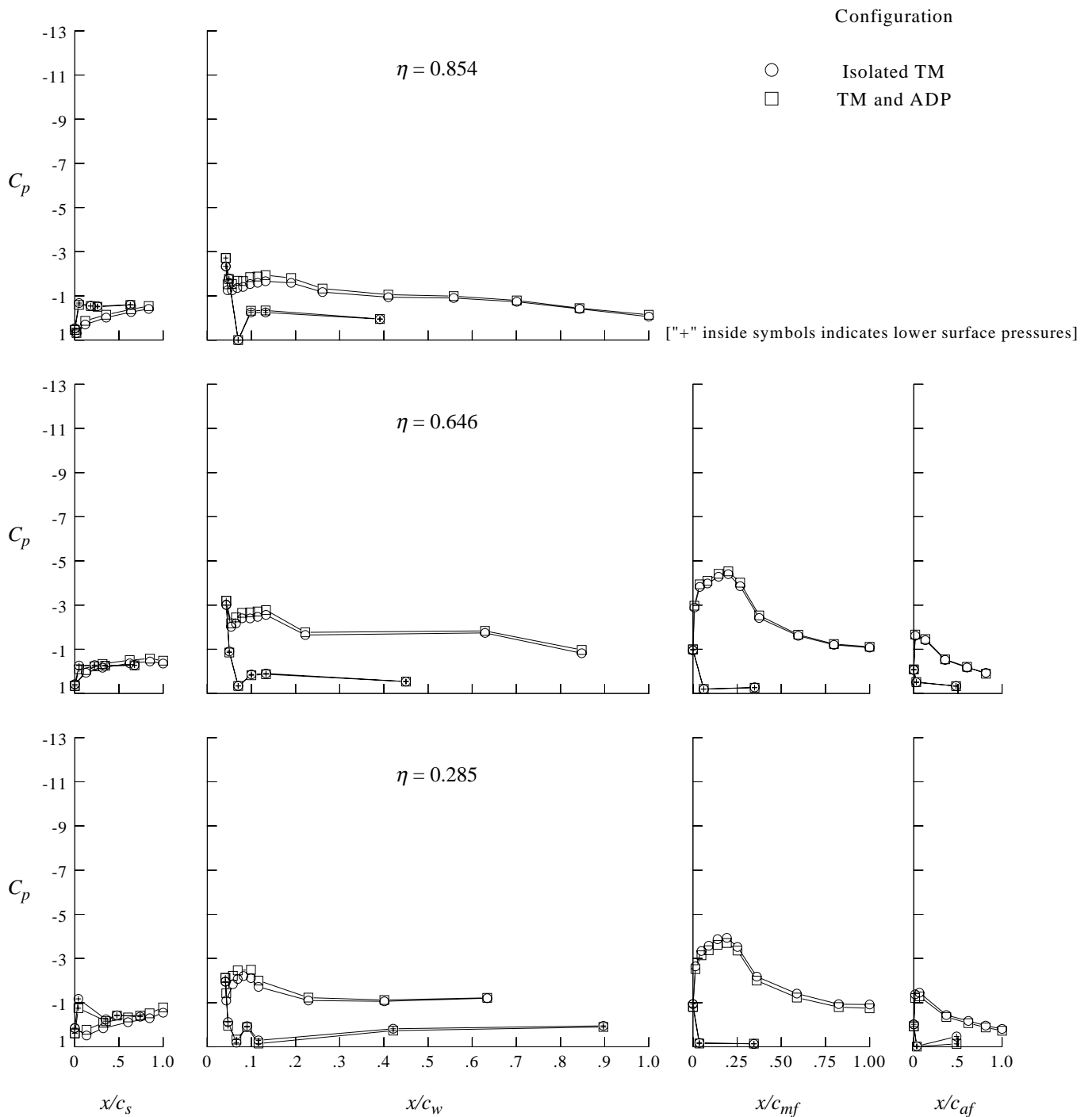


Figure 19. Windmilling ADP effect on transport model aerodynamic coefficients.
Slat-to-nacelle gap = 2.75 in.; $\beta_{ADP} = 98.25^\circ$ $\alpha \approx 0^\circ$.



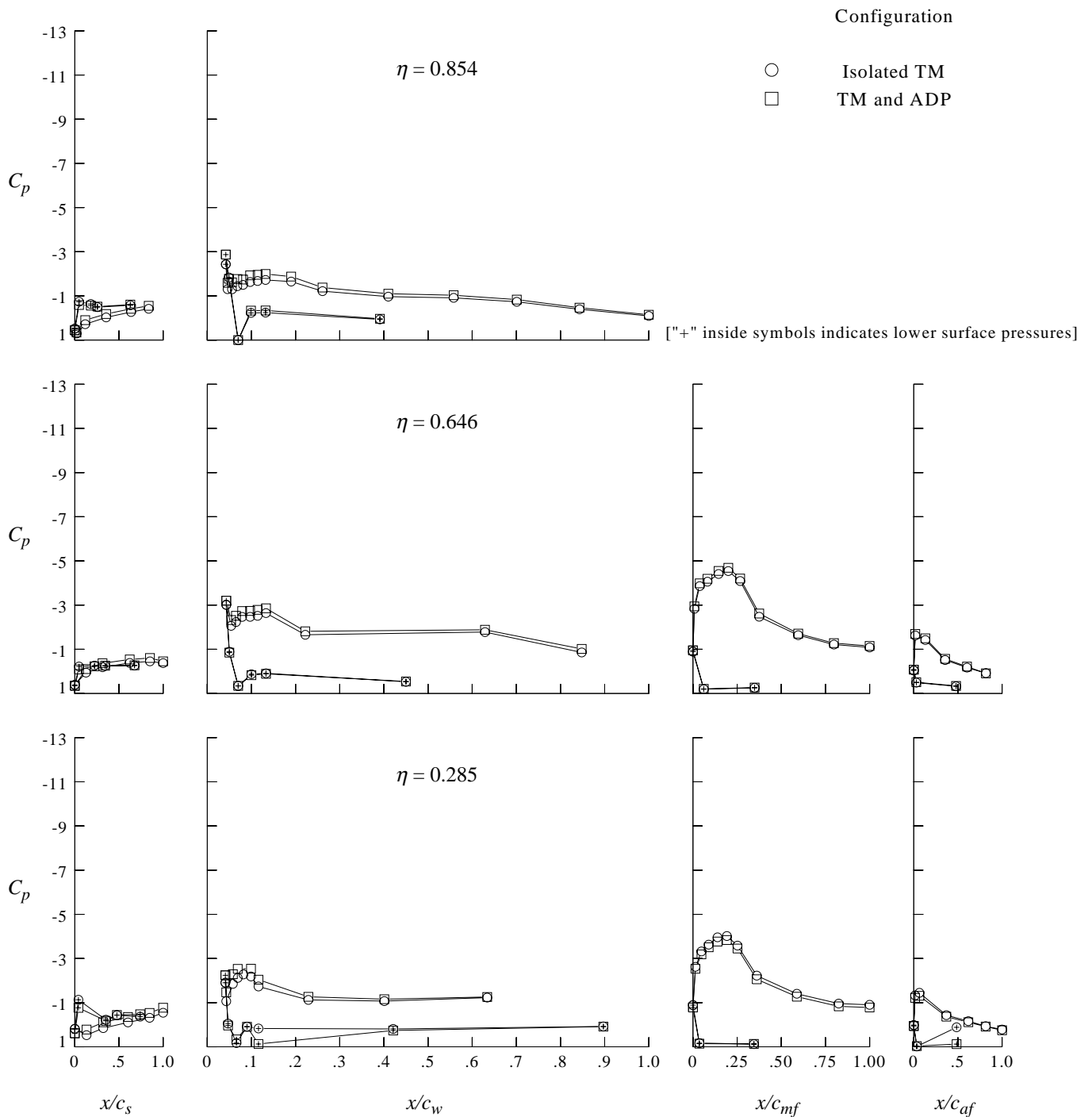
(a) $u_\infty \approx 96$ knots.

Figure 20. Windmilling ADP effect on high-lift wing pressure distributions. Slat-to-nacelle gap = 2.75 in.; $\beta_{ADP} = 98.25^\circ$ $\alpha \approx 0^\circ$



(b) $u_\infty \approx 125$ knots.

Figure 20. Continued.



(c) $u_\infty \approx 148$ knots.

Figure 20. Concluded.

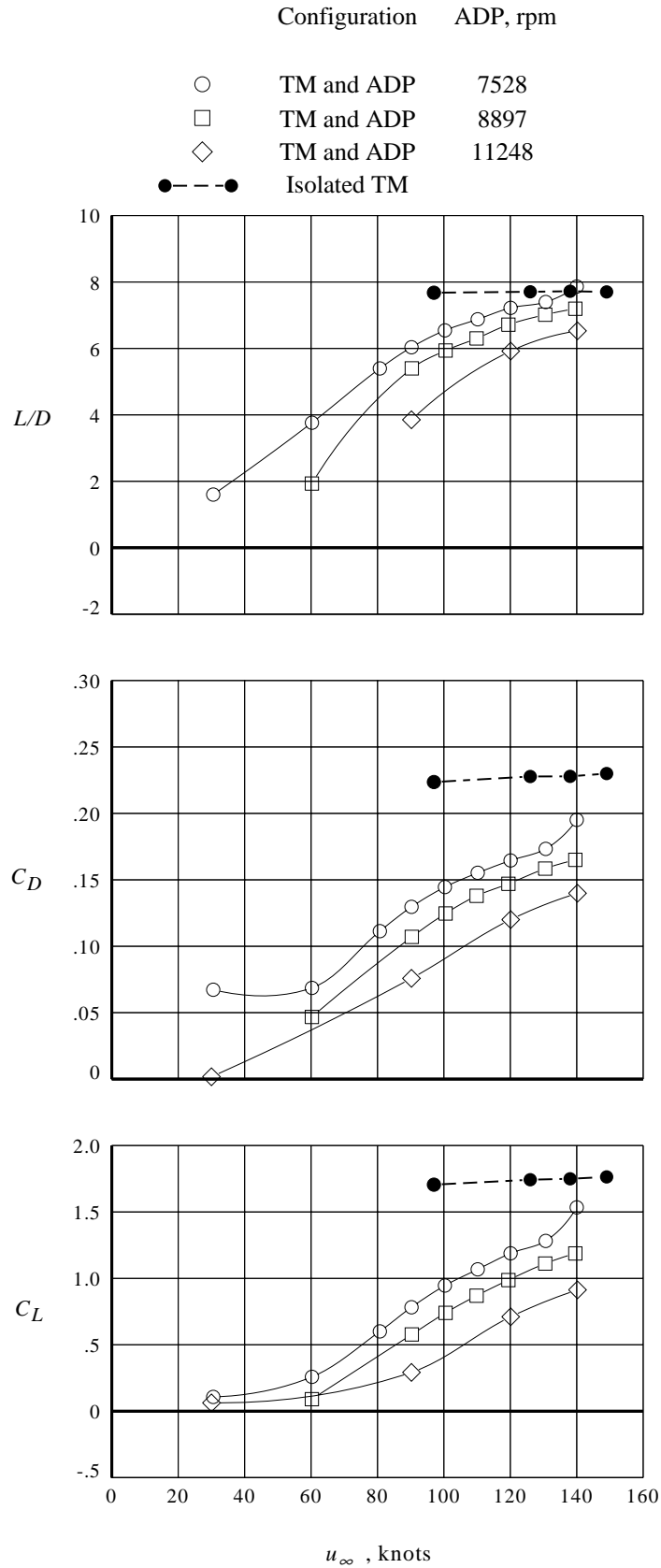


Figure 21. Powered ADP reverse-thrust effect on transport model aerodynamic coefficients. Slat-to-nacelle gap = 0.38 in.; $\beta_{ADP} = 98.25^\circ$ $\alpha \approx 0^\circ$.

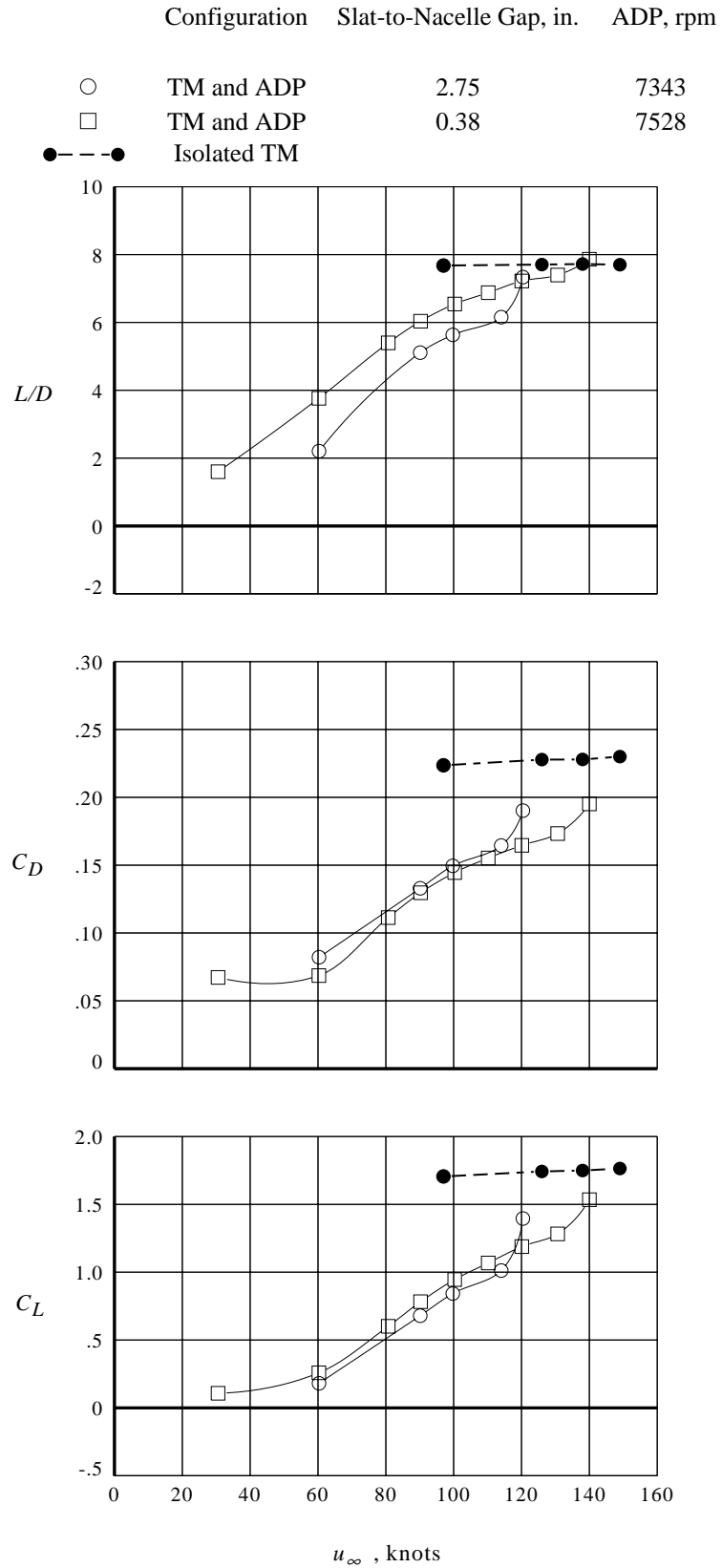
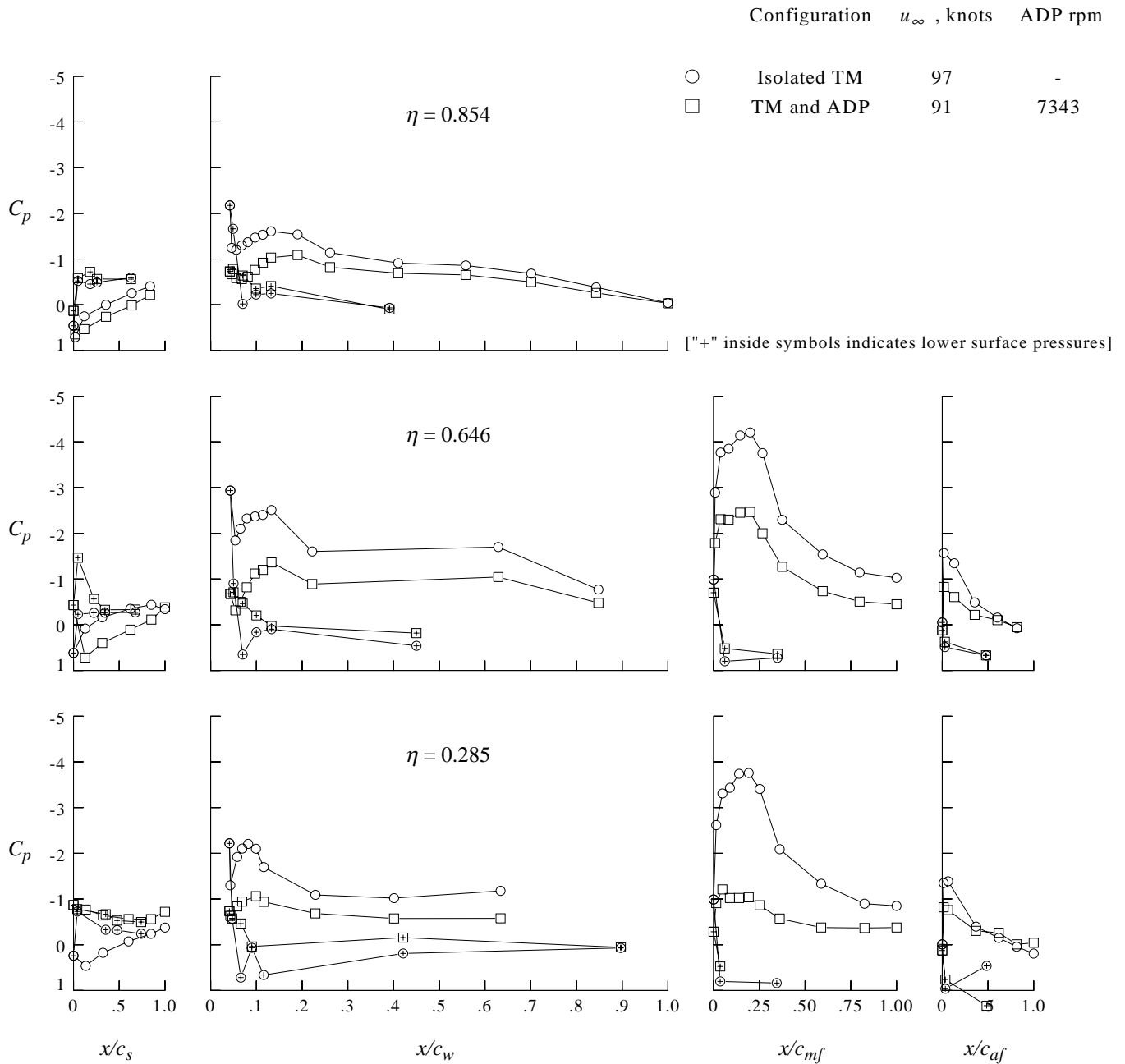


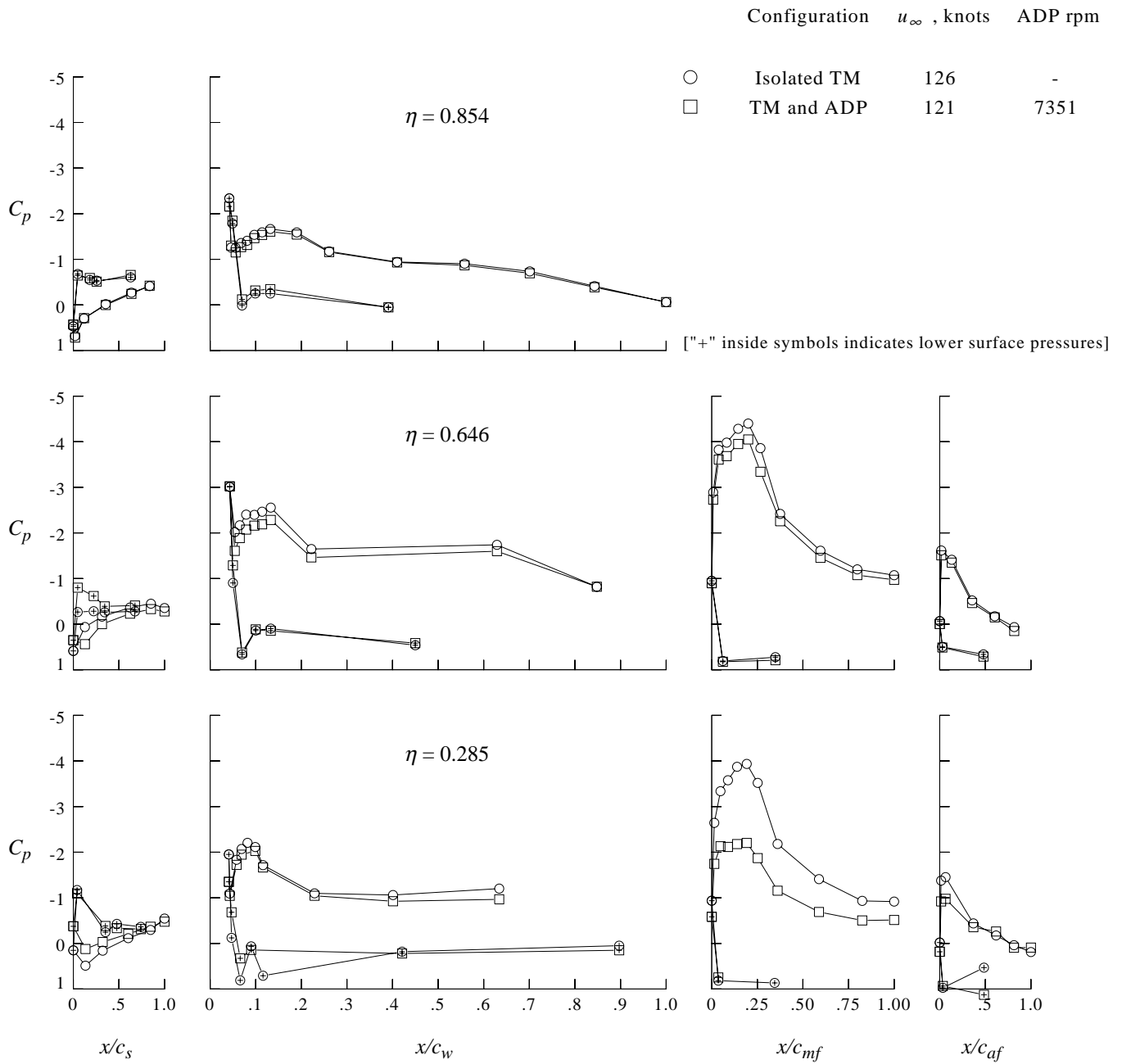
Figure 22. Aerodynamic coefficient comparison for two ADP waterline locations. $\beta_{ADP} = 98.25^\circ$ $\alpha \approx 0^\circ$.



(a) $u_\infty \approx 91$ knots.

Figure 23. Powered ADP reverse-thrust effect on high-lift wing pressure distributions.

Slat-to-nacelle gap = 2.75 in.; $\beta_{ADP} = 98.25^\circ$ $\alpha \approx 0^\circ$.



(b) $u_\infty \approx 121$ knots.

Figure 23. Concluded.

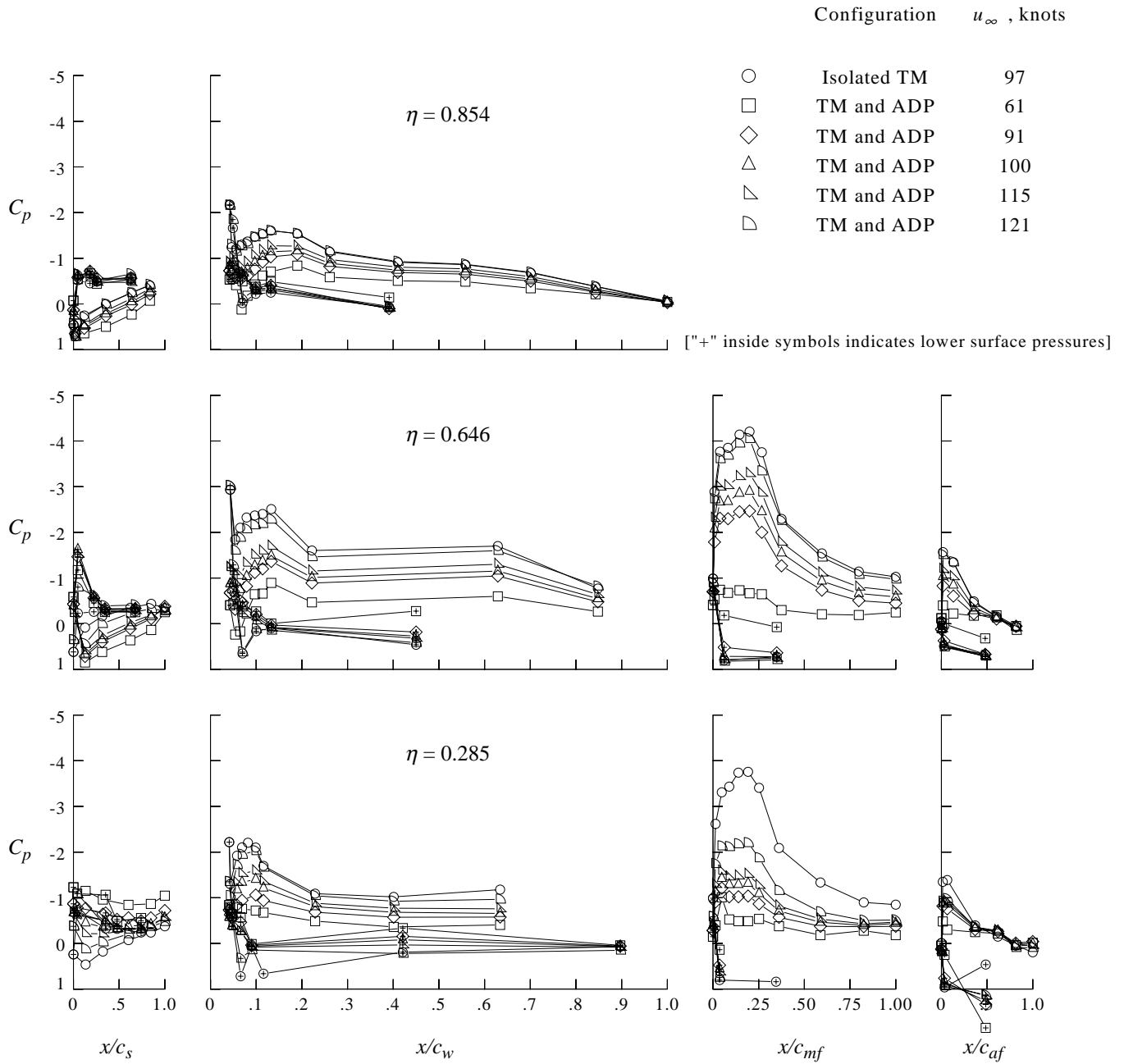


Figure 24. Powered ADP reverse-thrust effect on high-lift wing pressure distributions. ADP speed ≈ 7300 rpm; slat-to-nacelle gap = 2.75 in.; $\beta_{ADP} = 98.25^\circ$ $\alpha \approx 0^\circ$.

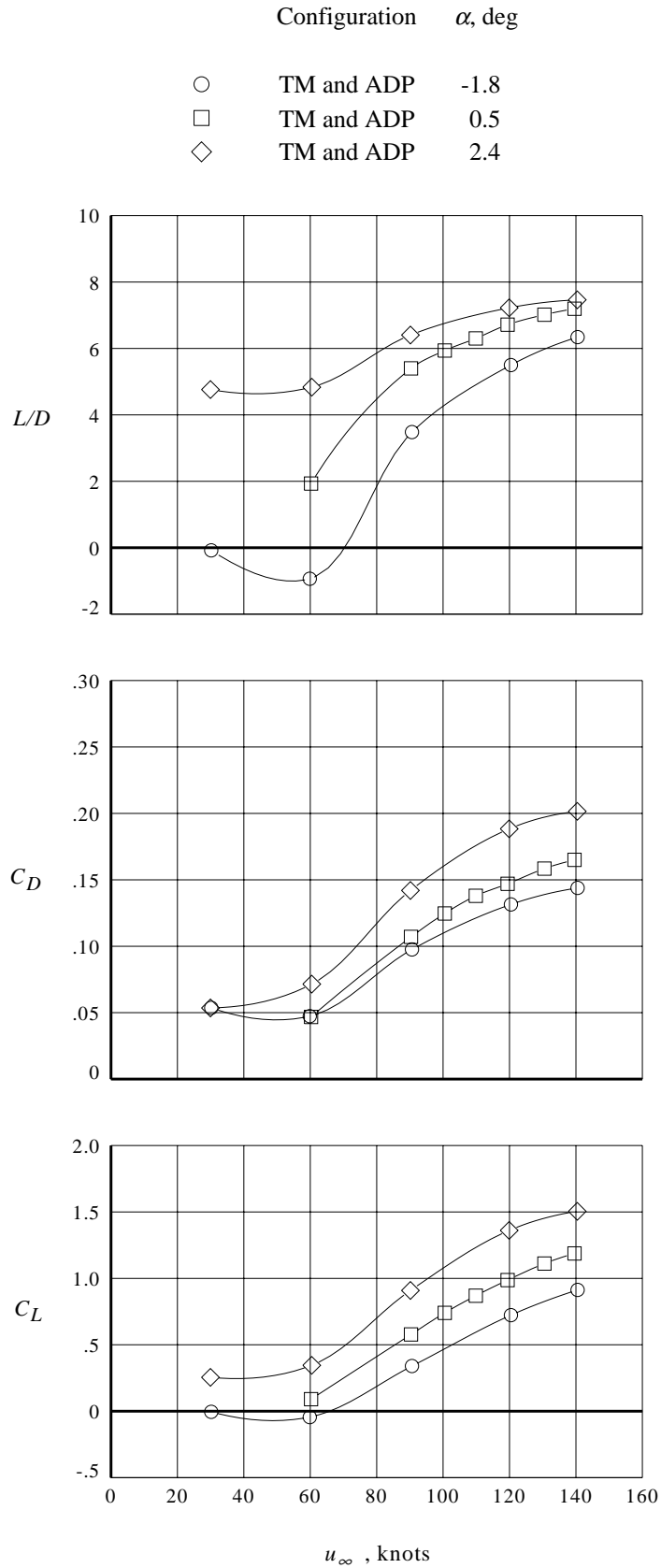


Figure 25. Angle of attack effect on transport model aerodynamic coefficients. Powered ADP; ADP speed ≈ 8900 rpm; slat-to-nacelle gap = 0.38 in.; $\beta_{ADP} = 98.25^\circ$.

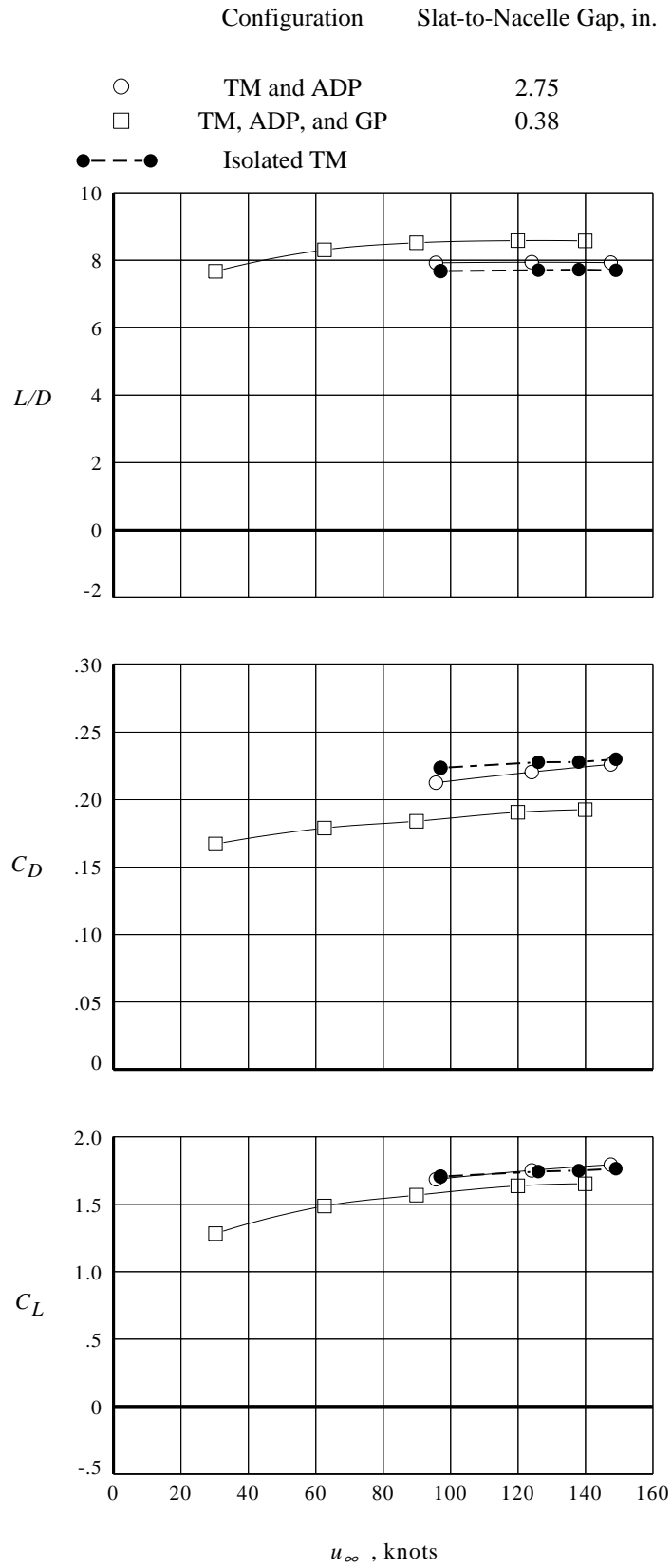


Figure 26. Ground plane effect on transport model aerodynamic coefficients. Windmilling ADP;
 $\beta_{ADP} = 98.25^\circ$ $\alpha \approx 0^\circ$

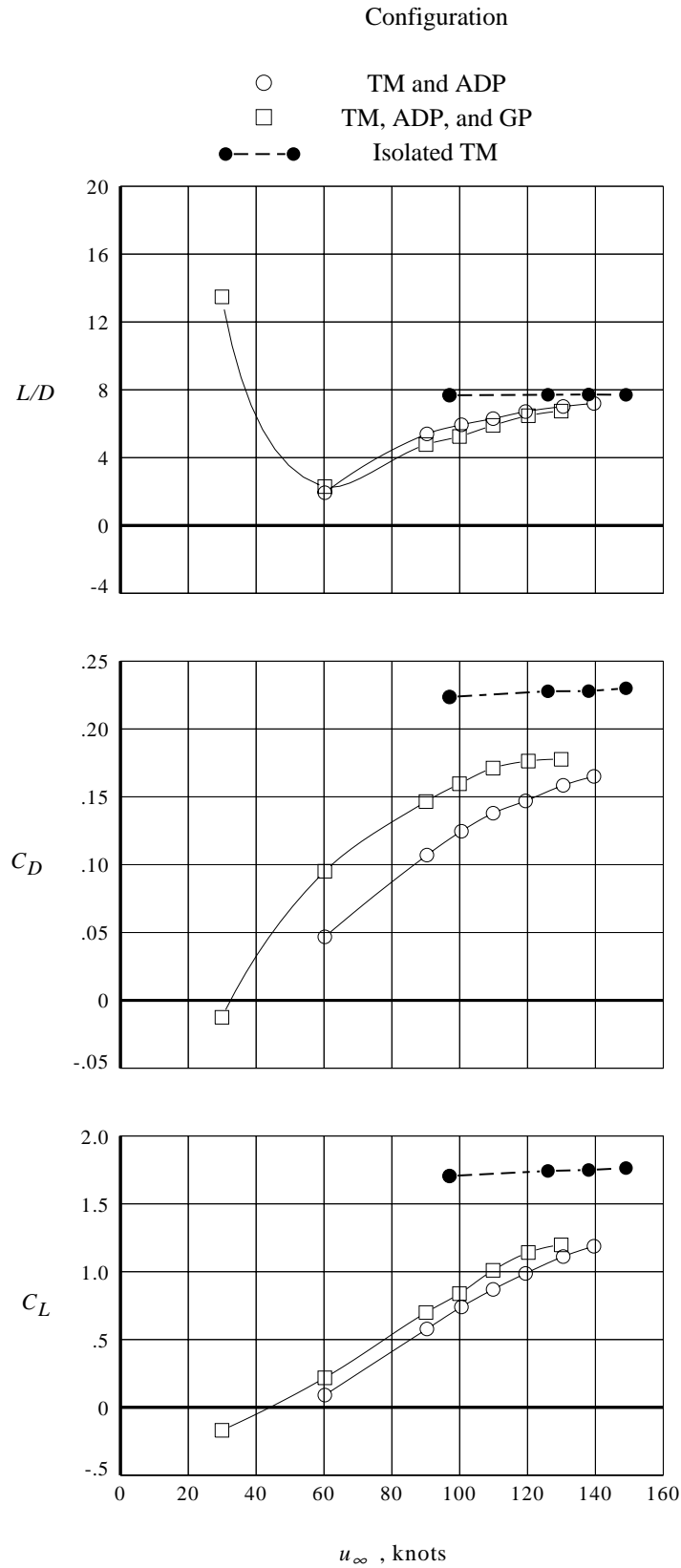


Figure 27. Groundplane effect on transport model aerodynamic coefficients. Powered ADP; ADP speed ≈ 8900 rpm; slat-to-nacelle gap = 0.38 in.; $\beta_{ADP} = 98.25^\circ$ $\alpha \approx 0^\circ$.

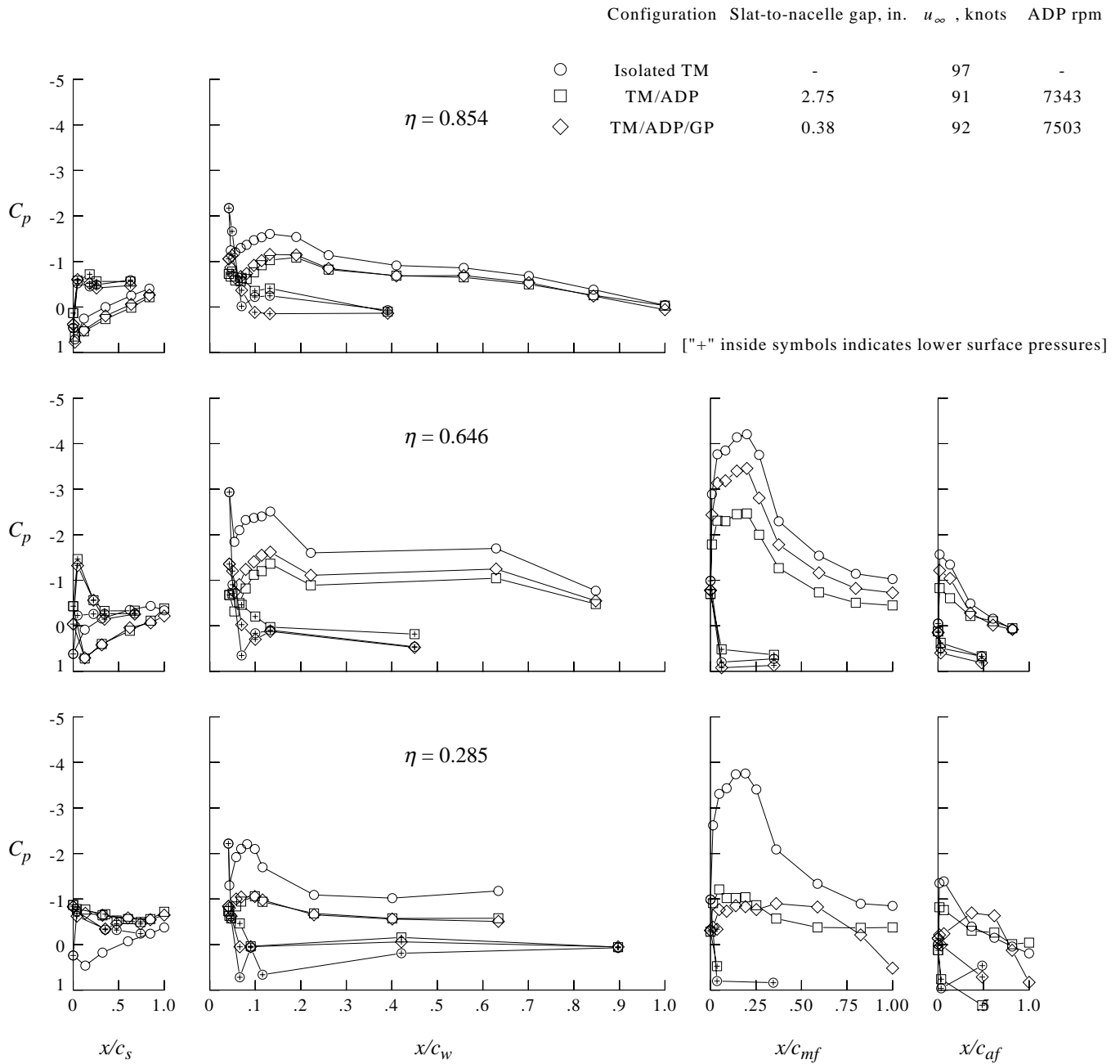
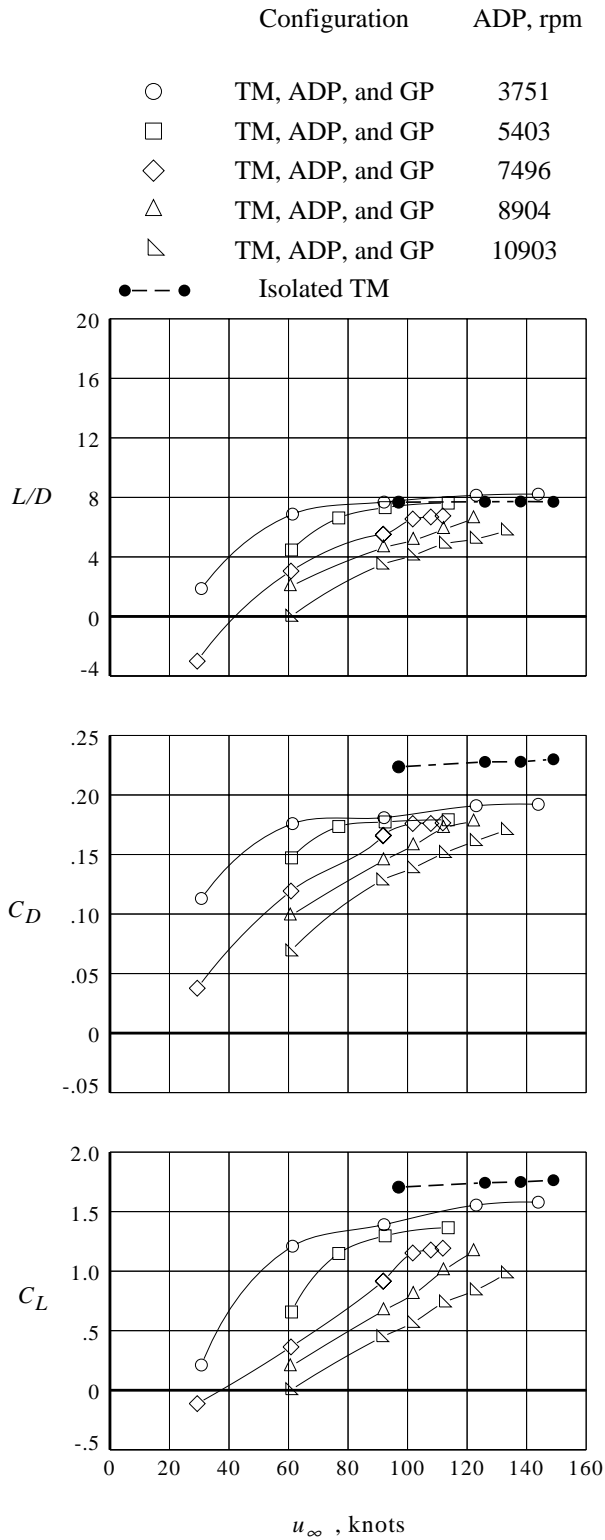
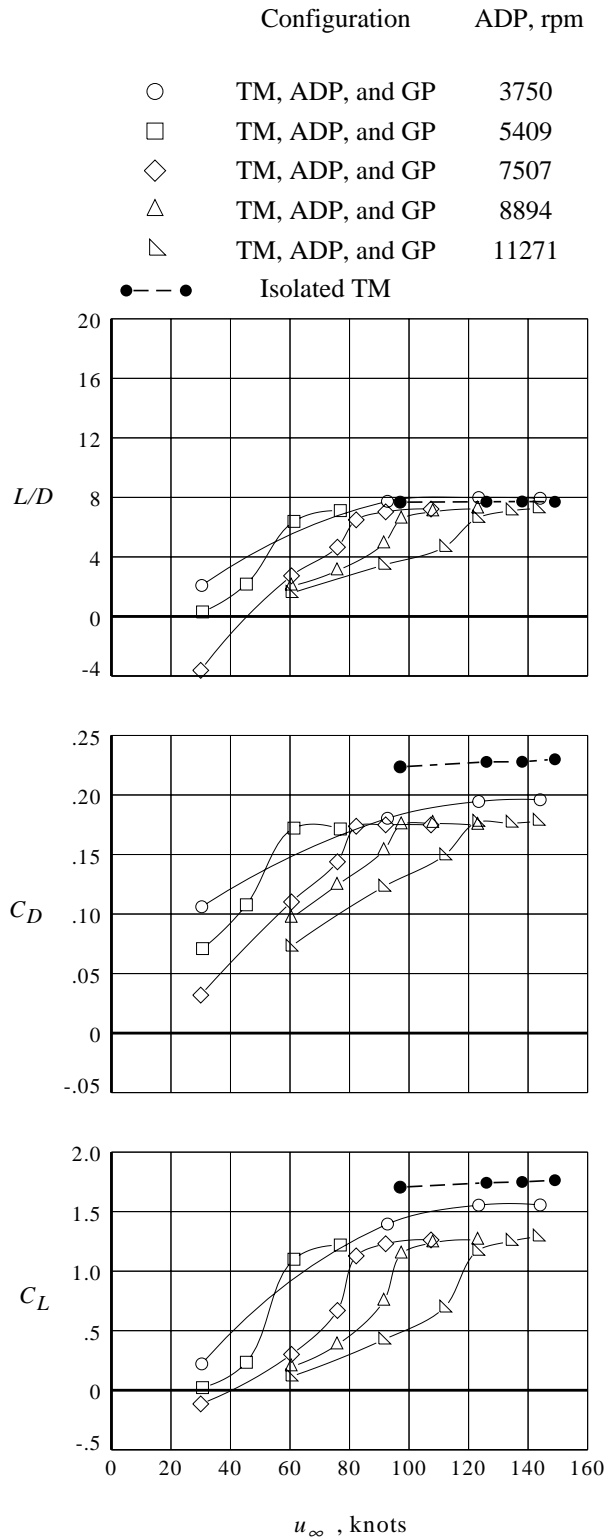


Figure 28. Ground plane effect on high-lift wing pressure distributions. Powered ADP; $\beta_{ADP} = 98.25^\circ$ $\alpha \approx 0^\circ$.



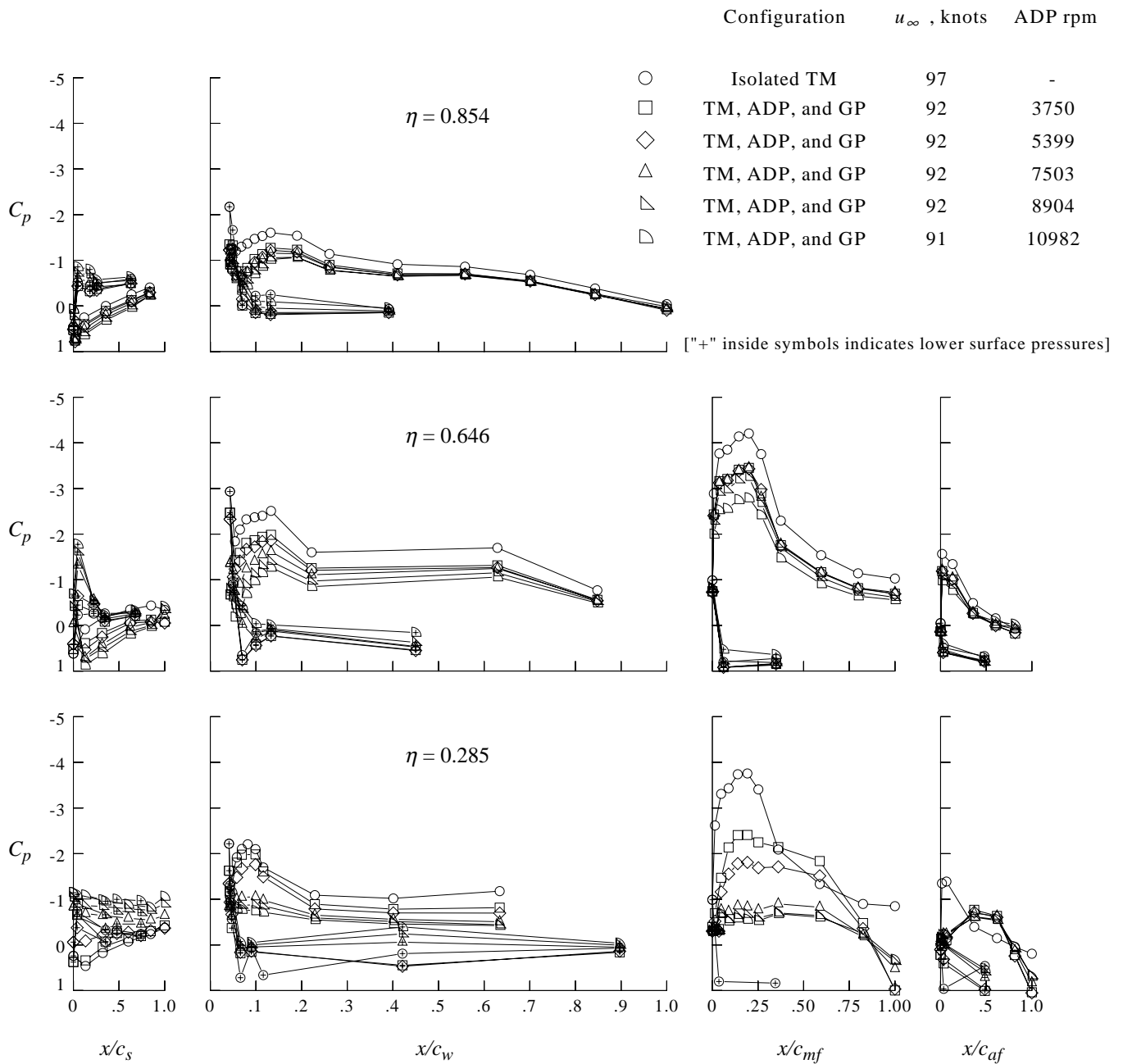
(a) $\beta_{ADP} = 98.25^\circ$.

Figure 29. ADP rotational speed effect on transport model aerodynamic coefficients with groundplane installed. Slat-to-nacelle gap = 0.38 in.; $\alpha \approx 0^\circ$.



(b) $\beta_{ADP} = 95^\circ$.

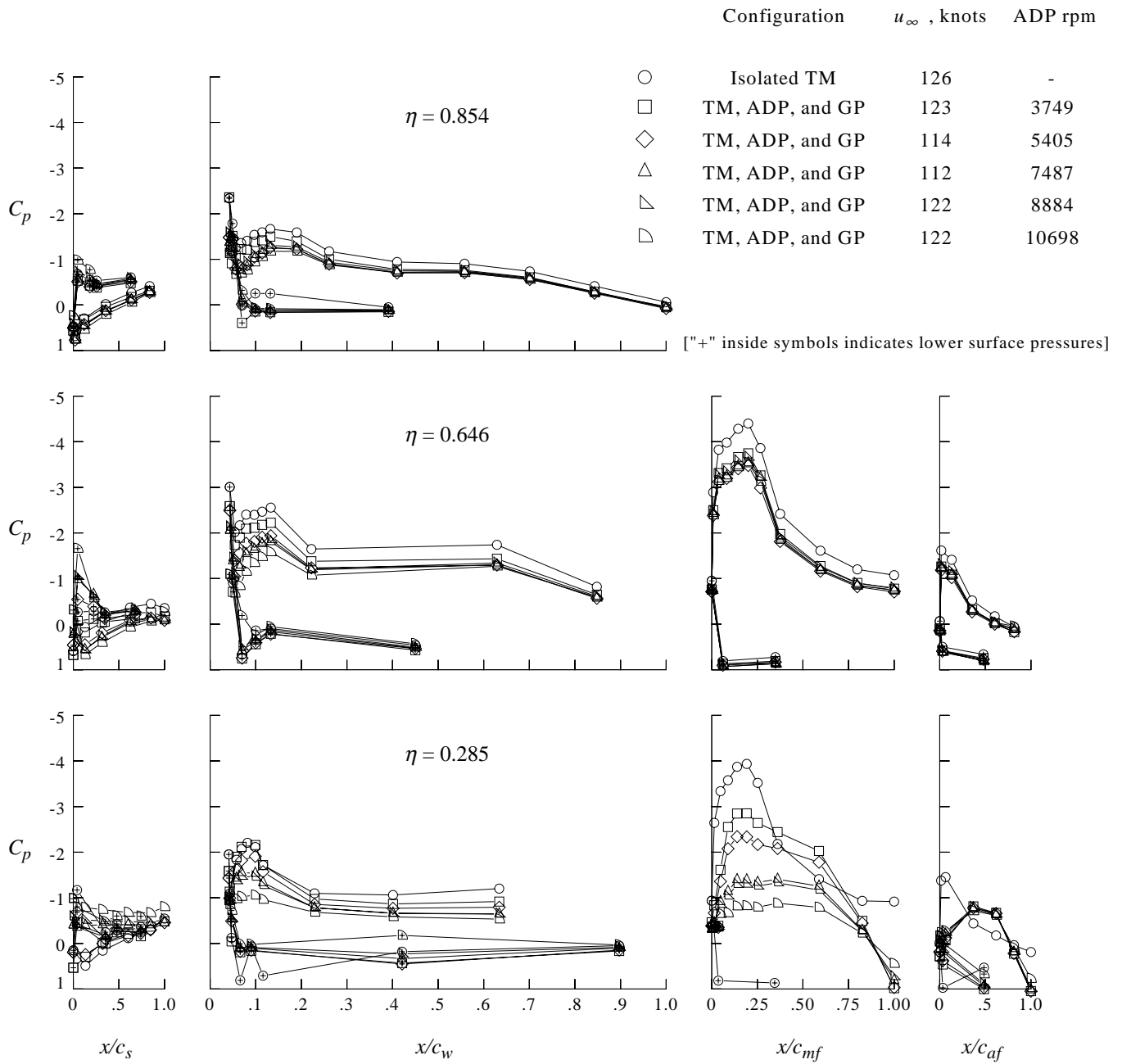
Figure 29. Concluded.



(a) $u_\infty \approx 92$ knots.

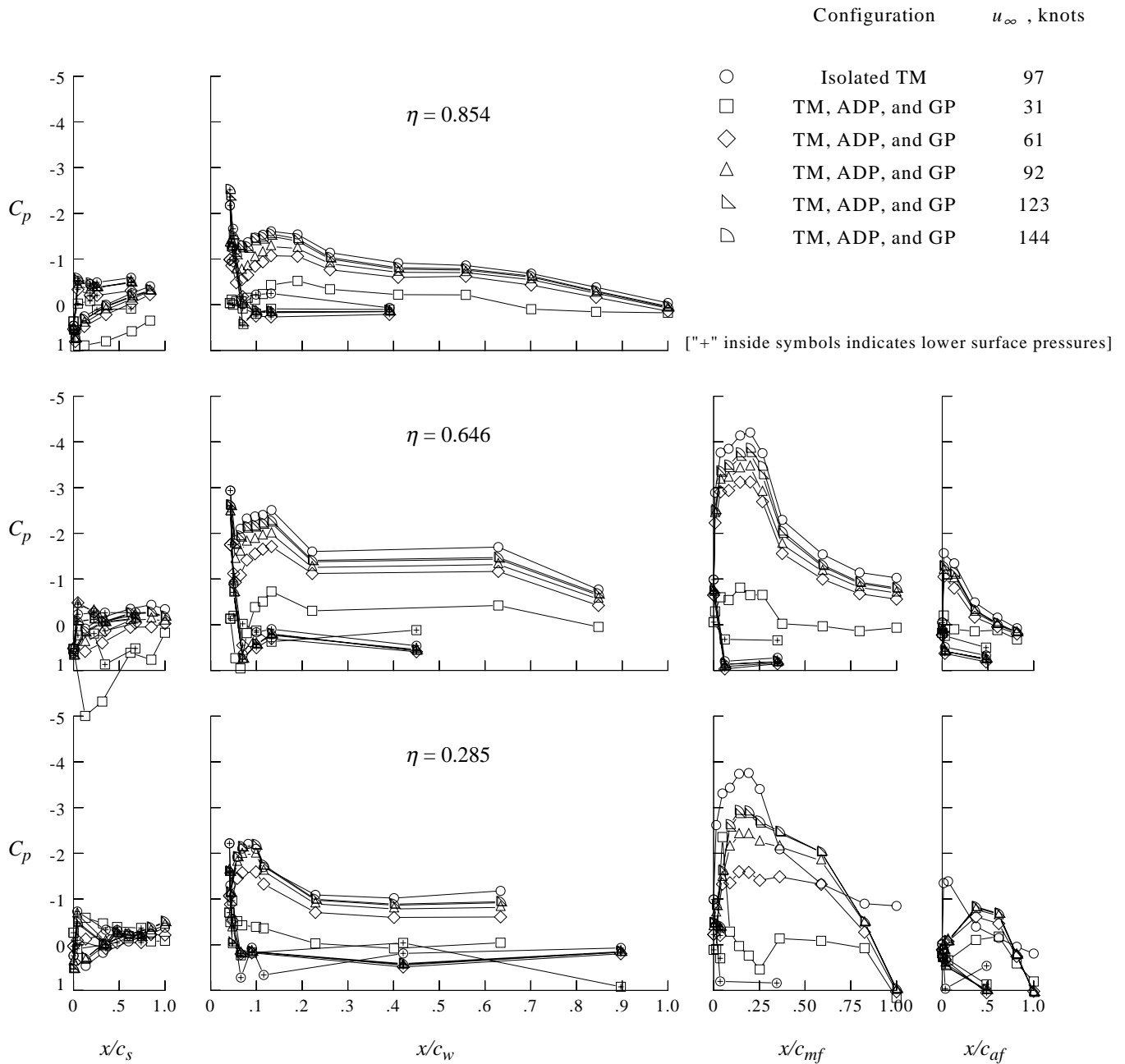
Figure 30. Powered ADP effect on high-lift wing pressure distributions with ground plane installed.

Slat-to-nacelle gap = 0.38 in.; $\beta_{ADP} = 98.25^\circ$ $\alpha \approx 0^\circ$.



(b) $u_\infty \approx 120$ knots.

Figure 30. Concluded.



(a) ADP speed \approx 3750 rpm.

Figure 31. Free-stream speed and powered ADP effects on high-lift wing pressure distributions with ground plane installed. Slat-to-nacelle gap = 0.38 in.; $\beta_{ADP} = 98.25^\circ$ $\alpha \approx 0^\circ$.

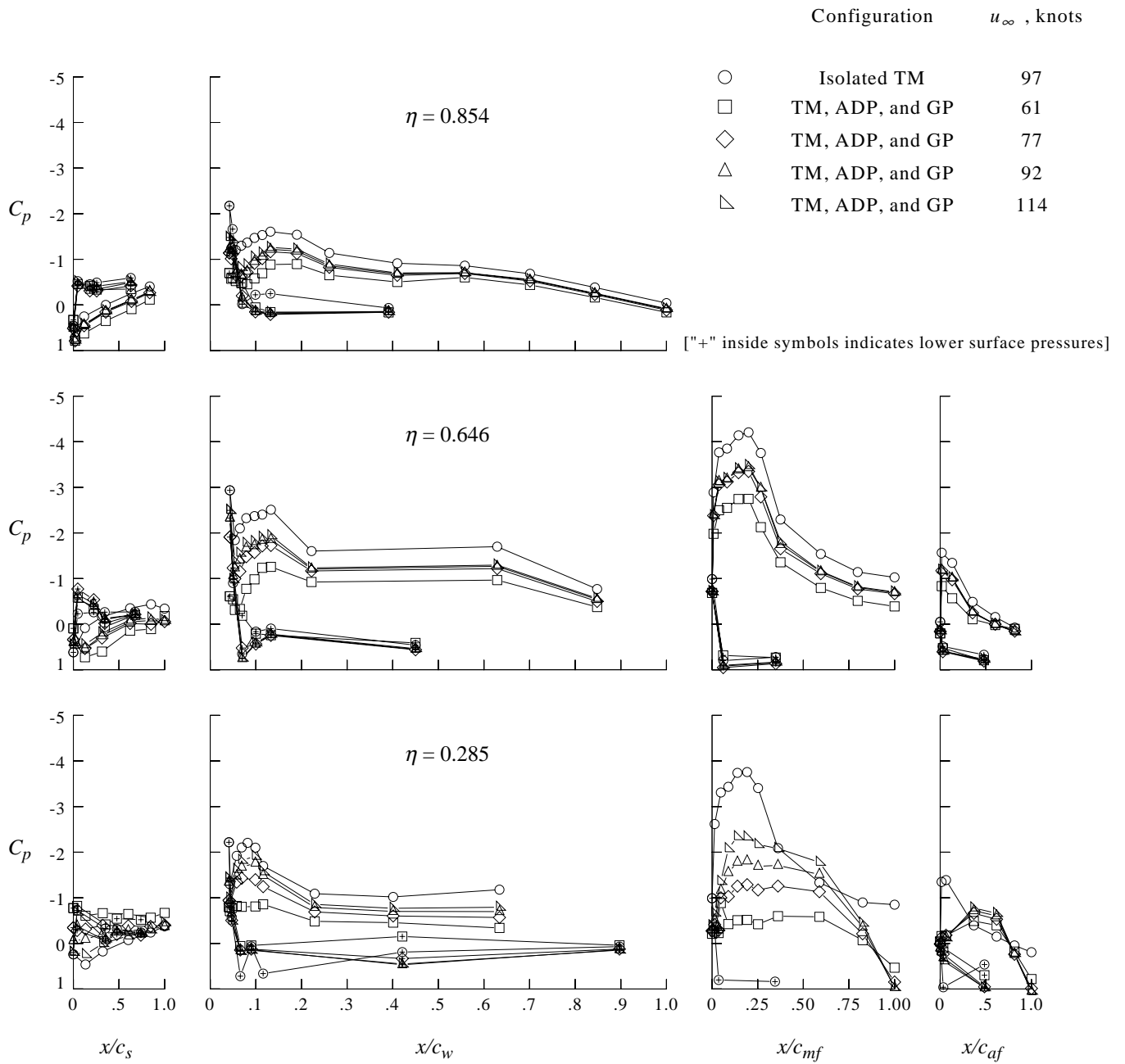
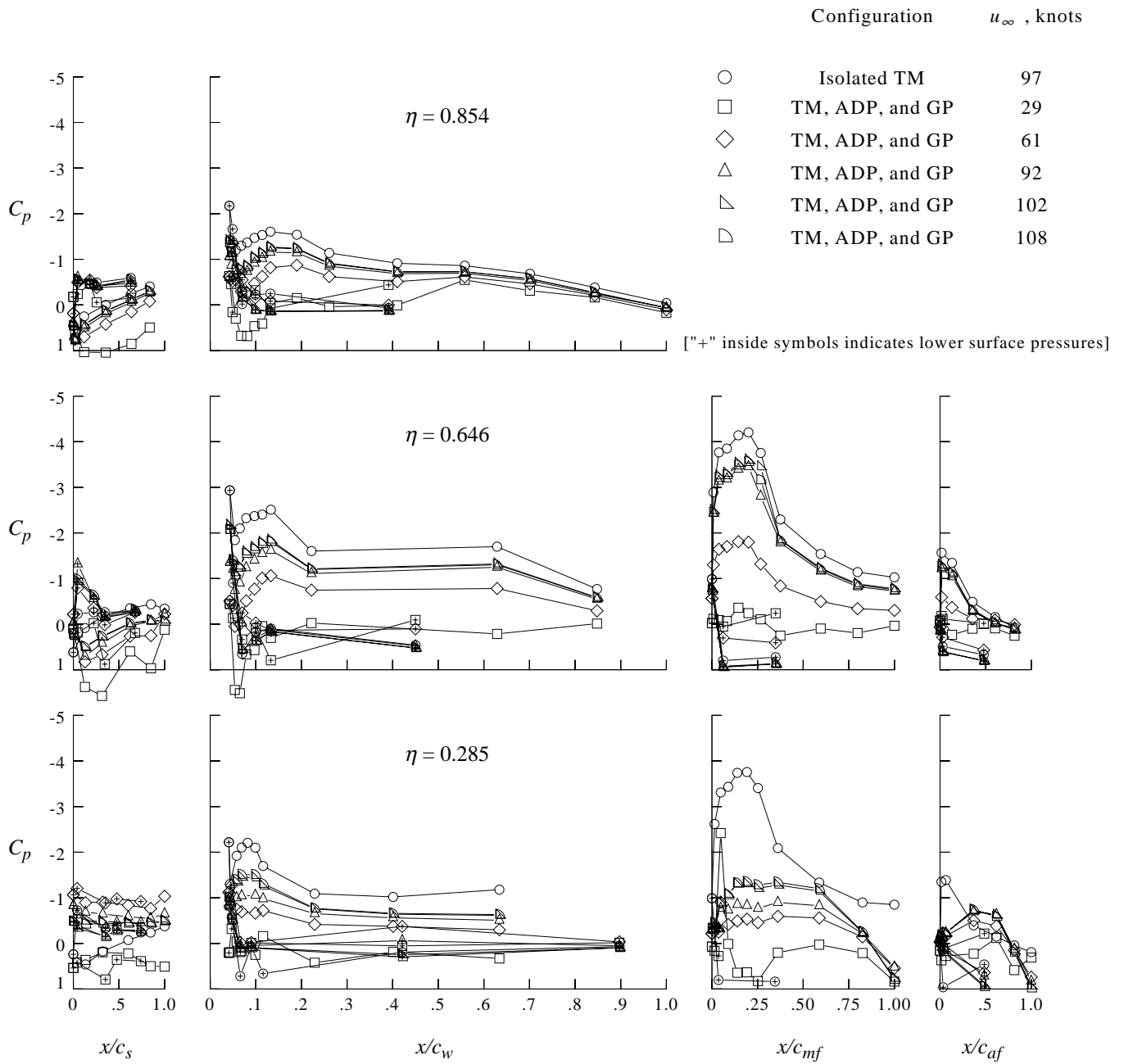
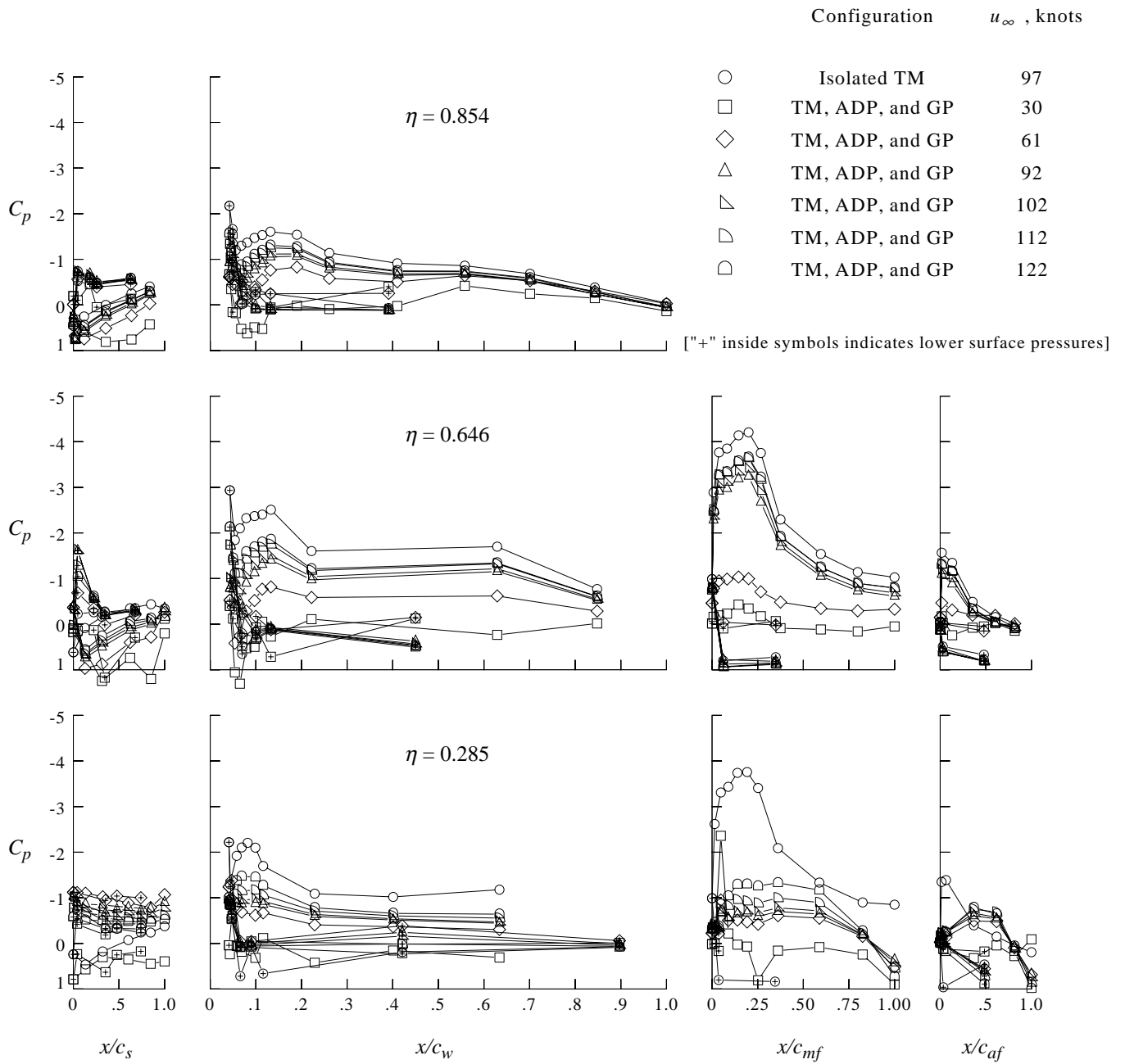


Figure 31. Continued.



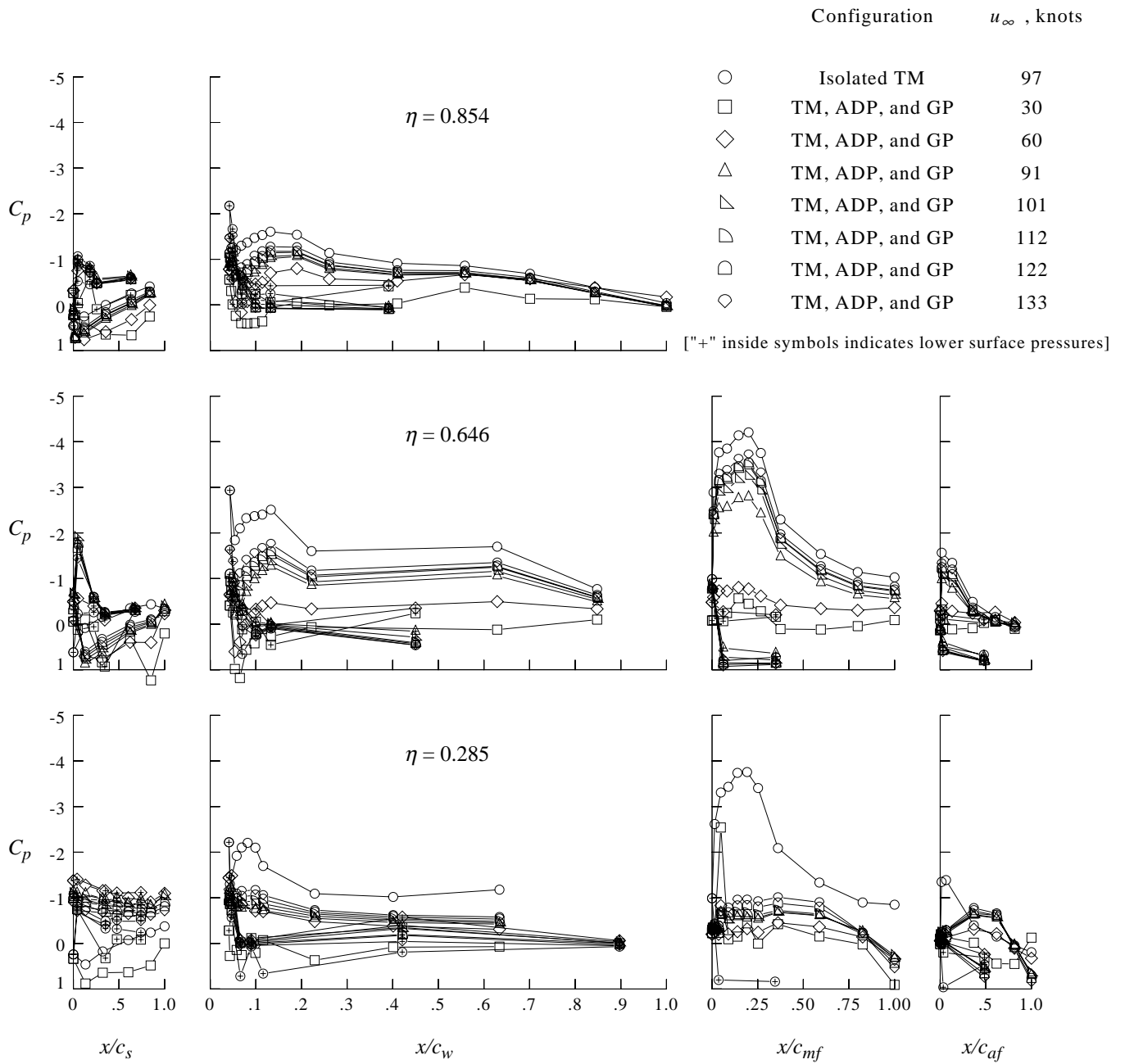
(c) ADP speed \approx 7500 rpm.

Figure 31. Continued.



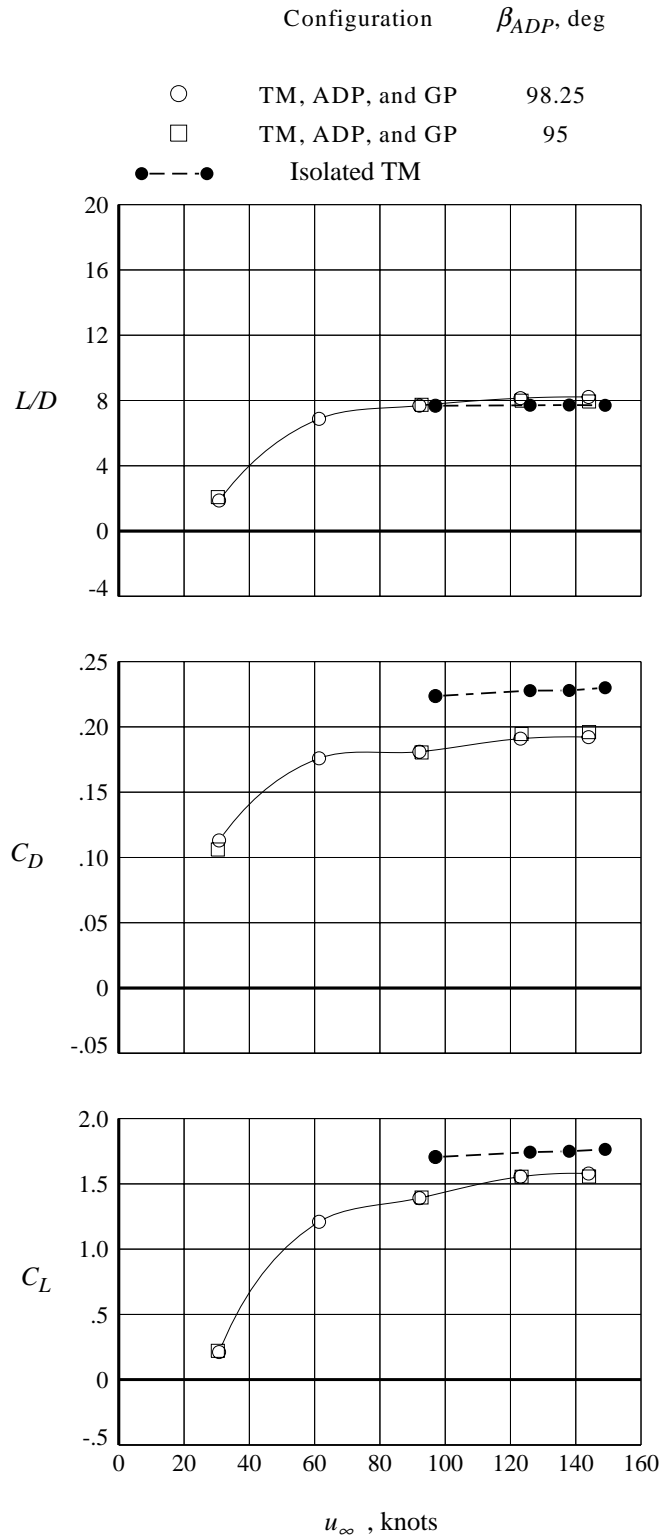
(d) ADP speed \approx 8900 rpm.

Figure 31. Continued.



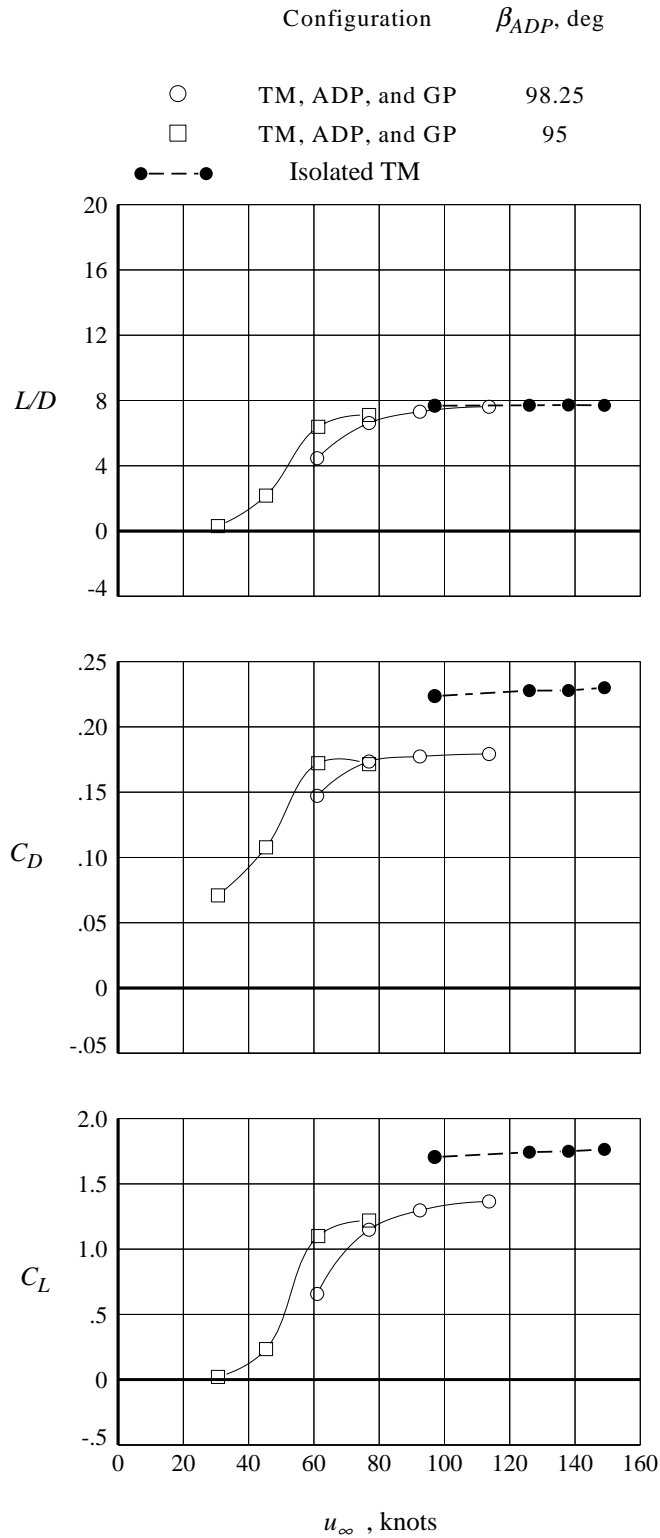
(e) ADP speed \approx 11 200 rpm.

Figure 31. Concluded.



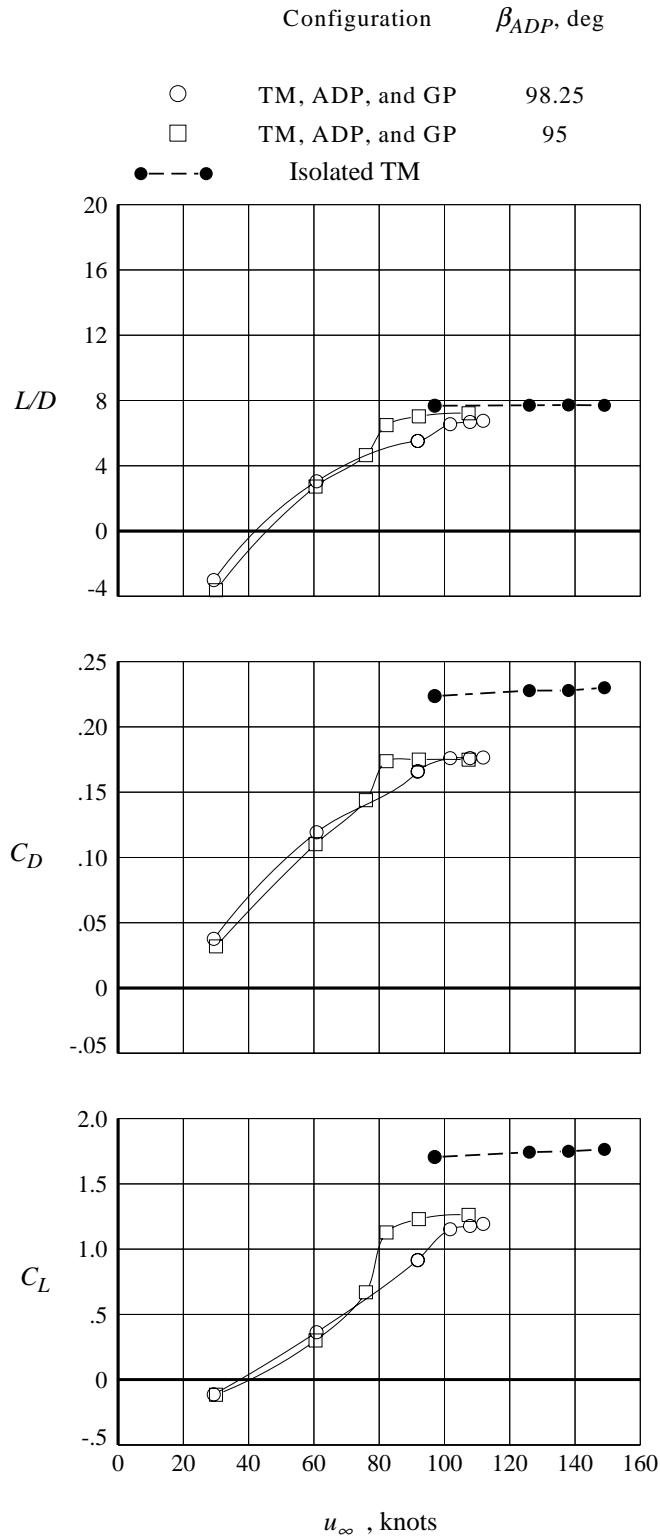
(a) ADP speed \approx 3750 rpm.

Figure 32. ADP blade angle effect on transport model aerodynamic coefficients with ground plane installed. Slat-to-nacelle gap = 0.38 in.; $\alpha \approx 0^\circ$.



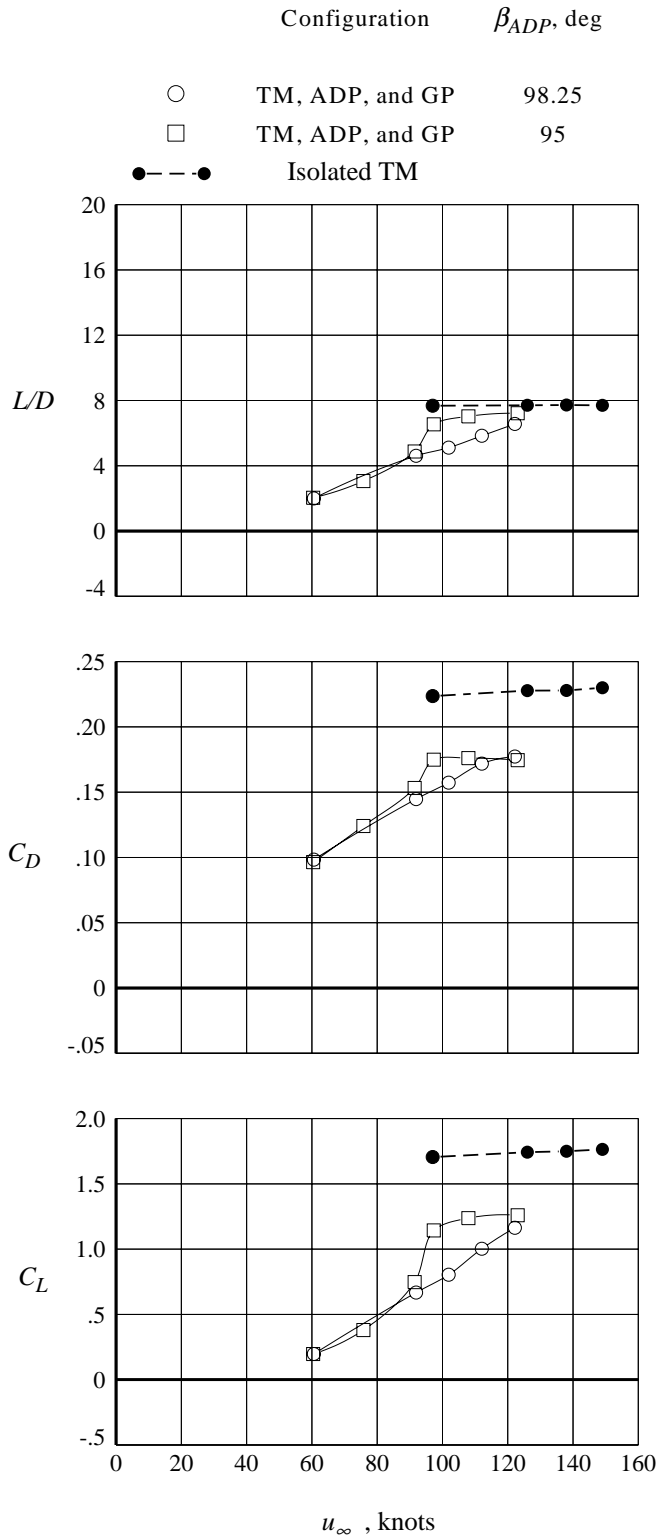
(b) ADP speed \approx 5400 rpm.

Figure 32. Continued.



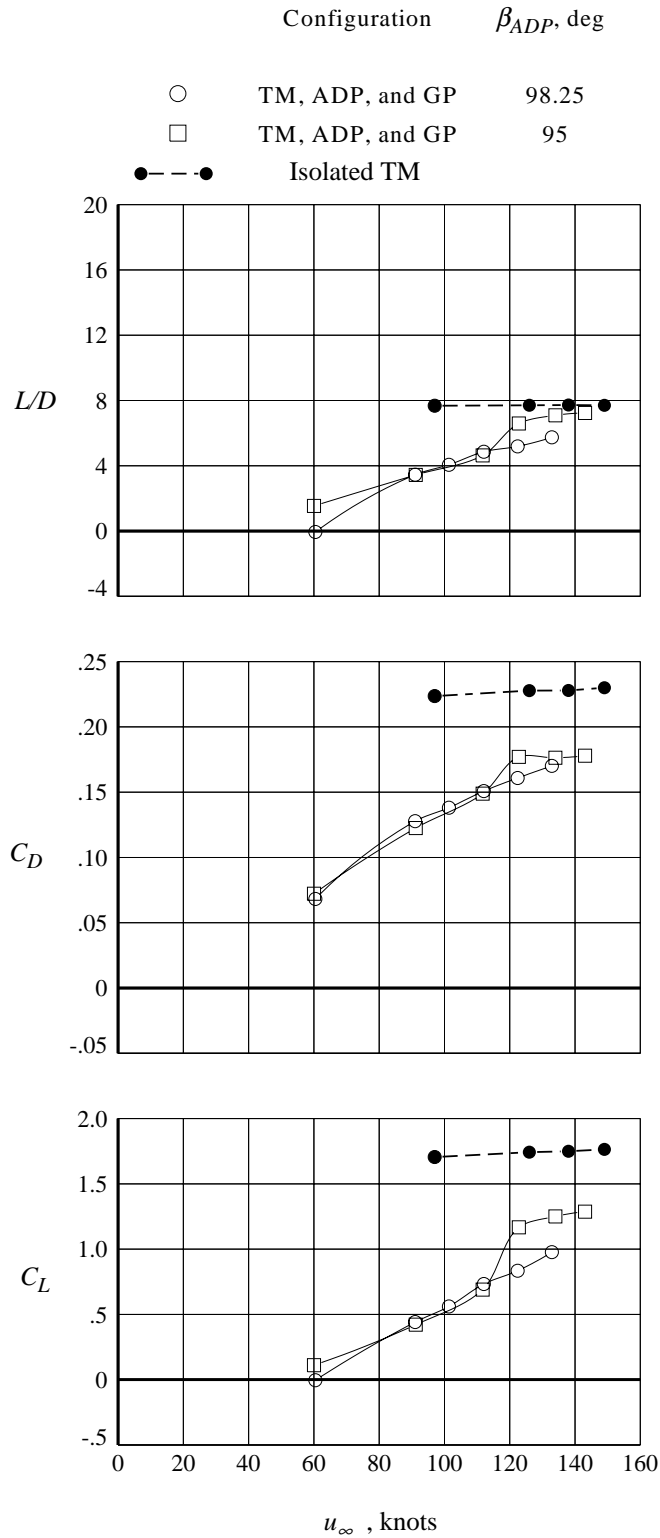
(c) ADP speed \approx 7500 rpm.

Figure 32. Continued.



(d) ADP speed \approx 8900 rpm.

Figure 32. Continued.



(e) ADP speed \approx 11 200 rpm.

Figure 32. Concluded.

- (b) Cruise wing planform.
- (c) High-lift wing planform.

Figure 1. Concluded.

REPORT DOCUMENTATION PAGE			Form Approved OMB No. 0704-0188	
Public reporting burden for this collection of information is estimated to average 1 hour per response, including the time for reviewing instructions, searching existing data sources, gathering and maintaining the data needed, and completing and reviewing the collection of information. Send comments regarding this burden estimate or any other aspect of this collection of information, including suggestions for reducing this burden, to Washington Headquarters Services, Directorate for Information Operations and Reports, 1215 Jefferson Davis Highway, Suite 1204, Arlington, VA 22202-4302, and to the Office of Management and Budget, Paperwork Reduction Project (0704-0188), Washington, DC 20503.				
1. AGENCY USE ONLY (Leave blank)	2. REPORT DATE July 1994	3. REPORT TYPE AND DATES COVERED Technical Paper		
4. TITLE AND SUBTITLE Subsonic Aerodynamic Characteristics of Semispan Commercial Transport Model With Wing-Mounted Advanced Ducted Propeller Operating in Reverse Thrust			5. FUNDING NUMBERS WU 535-03-10-02	
6. AUTHOR(S) Zachary T. Applin, Kenneth M. Jones, Brenda E. Gile, and P. Frank Quinto				
7. PERFORMING ORGANIZATION NAME(S) AND ADDRESS(ES) NASA Langley Research Center Hampton, VA 23681-0001			8. PERFORMING ORGANIZATION REPORT NUMBER L-17282	
9. SPONSORING/MONITORING AGENCY NAME(S) AND ADDRESS(ES) National Aeronautics and Space Administration Washington, DC 20546-0001			10. SPONSORING/MONITORING AGENCY REPORT NUMBER NASA TP-3427	
11. SUPPLEMENTARY NOTES				
12a. DISTRIBUTION/AVAILABILITY STATEMENT Unclassified-Unlimited Subject Category 02			12b. DISTRIBUTION CODE	
13. ABSTRACT (Maximum 200 words) A test was conducted in the Langley 14- by 22-Foot Subsonic Tunnel to determine the effect of the reverse-thrust flow field of a wing-mounted advanced ducted propeller on the aerodynamic characteristics of a semispan subsonic high-lift transport model. The advanced ducted propeller (ADP) model was mounted separately in position alongside the wing so that only the aerodynamic interference of the propeller and nacelle affected the aerodynamic performance of the transport model. Mach numbers ranged from 0.14 to 0.26; corresponding Reynolds numbers ranged from 2.2 to 3.9×10^6 . The reverse-thrust flow field of the ADP shielded a portion of the wing from the free-stream airflow and reduced both lift and drag. The reduction in lift and drag was a function of ADP rotational speed and free-stream velocity. Test results included ground effects data for the transport model and ADP configuration. The ground plane caused a beneficial increase in drag and an undesirable slight increase in lift. The ADP and transport model performance in ground effect was similar to performance trends observed for out of ground effect. The test results form a comprehensive data set that supports the application of the ADP engine and airplane concept on the next generation of advanced subsonic transports. Before this investigation, the engine application was predicted to have detrimental ground effect characteristics. Ground effect test measurements indicated no critical problems and were the first step in proving the viability of this engine and airplane configuration.				
14. SUBJECT TERMS Subsonic transport; High lift; Propulsion integration; Advanced ducted propeller; ADP; Semispan			15. NUMBER OF PAGES 113	
			16. PRICE CODE A06	
17. SECURITY CLASSIFICATION OF REPORT Unclassified	18. SECURITY CLASSIFICATION OF THIS PAGE Unclassified	19. SECURITY CLASSIFICATION OF ABSTRACT Unclassified	20. LIMITATION OF ABSTRACT	